TURBINE BLADE-TIP CLEARANCE EXCITATION FORCES

Final Report on Contract Number NAS8-35018

Submitted by

M. Martinez-Sanchez
Associate Professor, Aeronautics and Astronautics
Massachusetts Institute of Technology

and

Edward M. Greitzer, Co-investigator
Professor, Aeronautics and Astronautics

To

NASA, George C. Marshall Space Flight Center
Alabama 35812

Technical Monitor: Glenn E. Wilmer, Jr. EP23

Cambridge, Massachusetts

June 7, 1985

TABLE OF CONTENTS

Page

ABSTRACT

This report summarizes the results of an effort to assess the existing knowledge and plan the required experimentation in the area of turbine blade-tip excitation forces. The work was carried out in three phases, which are documented in Sections 1, 2 and 3 of this report, respectively. The first was a literature search and evaluation, which served to highlight the state of the art and to expose the need for an articculated theoretical-experimental effort to provide not only design data, but also a rational framework for their extrapolation to new configurations and regimes. The second phase was a start in this direction, in which several of the explicit or implikcikt assumptions contained in the usual formulations of the Alford force effect were removed and a rigorous linearized flow analysis of the behavior of a non-symmetric actuator disc was carried out. In the third phase of the work we conducted a preliminary design of a turbine test facility that would be used to measure both the excitation forces themselves and the flow patterns responsible for them, and do so over a realistic range of dimensionless parameters.

LIST OF SYMBOLS

A = Contact area in heat exchanger. Also turbine annulus area

A_f = Flow area in heat exchanger

c_x, c_y = Absolute flow velocity components

c'_x, c'_y = Perturbations of the above

c_p (c_v) = Specific heats at constant pressure (volume)

c = Blade chord

$C_{xx}, C_{xy}, C_{yx}, C_{yy}$ = Damping coefficients of shaft due to fluid effects

C_{ij} = Generic damping coefficient

D = Diameter

e = Turbine disc eccentricity

f = Pipe pressure loss factor

f = Turbine disc force per unit perimeter

f_{id} = Same, ideal

F_x, F_y = Total x and y forces on disc

F_{TOT} = Azimuthal net turbine force (= Torque/ω)

G = Mass flux, ρu

h = Heat transfer film coefficient

H = Blade height

i_{ex} = Brake excitation current

I = Brake load current

K_o = Structural shaft stiffness

$K_{xx}, K_{xy}, K_{yx}, K_{yy}$ = Stiffnesses of turbine shaft due to fluid effects

K_{ij} = Generic stiffness (i,j = x,y)

k_{ij} = K_{ij}/K_o

K_G, K_V, K_C, K_{TOT} = Constants defined in Sec. 3.6

$K_{cell}, K_{bar}, K_{TOT}$ = Stiffnesses (Sec. 3.7.4)

$\dot{m}$ = Mass flow rate

M = Rotor mass

$\mathcal{M}$ = Molecular mass

P = Pressure, Power

Pr = Prandtl number

Q, Q_g = Torque to brake

r_m = Turbine mean radius

R = Turbine mean radius. Also degree of reaction

R_e, R_{ey} = Reynolds Number

R_i, R_L = Internal and load resistances of brake

s = Clearance

t = Time. Also tip clearance (Sec. 2)

T = Temperature

u_x, u_y = Absolute flow velocity components

U = Peripheral wheel speed

u_B = "Bypass velocity" = $\dot{m}_B\, u_x/\dot{m}_t$

u_s = Ideal total turbine wheel force in azimuthal direction (Sec. 2)

V = Volume. Also, brake voltage

W = Turbine specific power

α = Sensitivity of local efficiency to blade-tip clearance (Sec. 1.1)

α = Specific area of heat exchanger (Sec. 3.5.2)

α_2 (α_3) = Stator (rotor) absolute flow leaving angle

β = Alford coefficient = $(RH/Q)K_{yx}$

β_1 = Stator incidence angle

β_2 (β_3) = Stator (rotor) relative flow leaving angle

γ = c_p/c_v, specific heat ratio

δ_{ax} = Axial (stator-rotor) gap

δ_o = Nominal radial gap

ΔP = Pressure drop

λ_g = Brake load control parameter

μ = Viscosity

η = Efficiency (local)

ηo = Efficiency at zero clearance

ω, Ω = Rotational speed

Ω = Whirl or vibration frequency

Π_t (Π_c) = Turbine (compressor) pressure ratio

ρ = Density

θ = Azimuthal coordinate

ζ_{ij} = Dimensionless damping factor = $C_{ij}/2\sqrt{K_o M}$

ψ = Loading parameter = specific enthalpy extraction/U^2

ψ = Stream function (Sec. 2)

1. A Literature Review on Alford Forces and Related Effects

1.1 Basic Concepts

The term "Alford force" is used in the U.S. to denote the cross-forces arising in turbomachinery as a consequence of uneven clearance gaps due to shaft displacements during vibration. An equivalent European designation is "Thomas force." The names are taken from the pioneering publications of J.S. Alford (Ref. 1, 1965) and H.J. Thomas (Ref. 2, 1958), who independently proposed essentially the same mechanism to explain observed "aerodynamic" instabilities in high power steam turbines (Thomas) and jet engines (Alford).

This mechanism is clearly illustrated for a turbine in Fig. 1.1, adapted from a recent paper by F. Ehrich and D. Childs (Ref. 3) in which an excellent overview is given of the known sources of self-excited turbomachine vibration. In essence, the higher efficiency in the area of closer tip clearance implies a larger forward aerodynamic force, and the net result is a force on the wheel which tends to feed into a forward whirling motion.

The essence of the argument used by both Thomas and Alford is as follows: the local efficiency η (for the case of a turbine) can be thought of as the ratio of the actual azimuthal force f per unit perimeter to the ideal force f_{id}. From data on concentric turbines at various values of the clearance s, it is known that η varies more or less linearly with the fractional clearance:

$$\frac{f}{f_{id}} = \eta_0 \left(1 - \alpha \frac{s}{H}\right) \qquad (1.1.1)$$

where η_0 is the efficiency at zero clearance, H is the blade height, and α is of order unity (See Fig.1.2). When the shaft is off-center in the x-direction by e_x, the local gap is approximately $s = s_0 - e_x \cos\theta$, where θ is measured from the point of smallest gap. Therefore, assuming the local efficiency behaves in the same way as that of a centered rotor,

$$f = f_{id}\, \eta_0 \left[1 - \alpha \frac{s_0}{H} + \alpha \frac{e_x}{H} \cos\theta\right] \qquad (1.1.2)$$

Projecting in the transverse direction, the total y-force will then be

$$F_y = \int_0^{2\pi} f \cos\theta \, R d\theta = f_{id}\, \eta_0\, \alpha \frac{e_x}{H}\, \pi R \qquad (1.1.3)$$

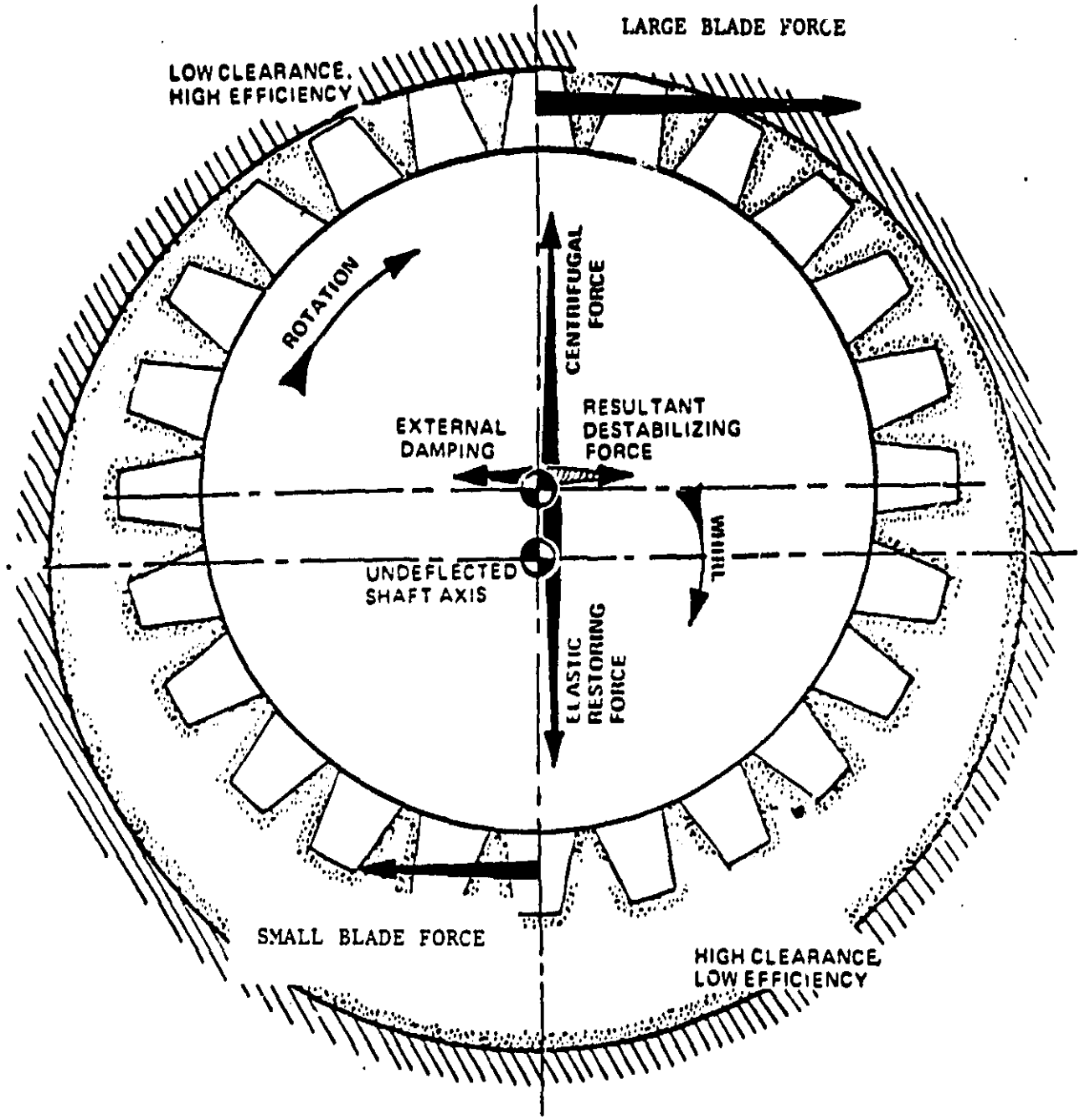

Fig. 1.1 Turbine Tip Clearance Effect's Contribution to Whirl

or, in terms of the "total tangential force" = $2\pi R f_{id} = F^{tot}_{id} = (Torque/R)_{id}$,

$$F_y = F^{tot}_{id} \frac{\alpha n_0}{2} \frac{e_x}{H} \qquad (1.1.4)$$

The group $\alpha n_0/2$ is called k_2 ("excitation coefficient") in the German literature, or $\beta/2$ (β = Alford coefficient) in the U.S. literature. Its value ranges, as we will see, from zero to about 3, depending on turbine design and operating point.

In turbines with no tip shroud band, this is the dominant mechanism for cross-force excitation. For shrouded turbines, on the one hand the sensitivity of n to gap is reduced (smaller α) but, on the other hand, nonuniform pressure distributions arise in the seal gap. This leads to additional, and often dominant, cross-forces, since the maximum and minimum of pressure do not line up with the direction of shaft displacement. The existence of this unsymmetric pressure pattern is closely related to the inlet flow swirl into the seal. The following simplified argument will help to understand the effect.

In a labyrinth seal gland, the fluid is sheared between an outer, stationary casing, and the rotor surface, and if no other effects were present, would acquire an azimuthal mean velocity which would be a certain fraction of the rotor linear speed. If the fluid arriving at the seal happens to have just this limiting azimuthal velocity, no change in it is required across the sealing strips (despite the jump in pressure). If the arriving azimuthal velocity is higher than the limit, and the seal is centered, the tangential flow speed in the gland is simply raised somewhat; but if the seal is off-centered, more azimuthal momentum is imparted to the fluid in the wider region, where the flow into the gland is higher, than to that in the narrow region. The result is a positive pressure gradient in the swirl direction over the wider zone, and a negative one in the narrow zone. The pressure peak happens ahead of the narrowest point, and the resultant pressure force is in the forward whirl direction. The opposite happens for inlet swirl <u>below</u> the limiting value.

In a 50% reaction turbine with axial exit the flow leaving the stator blading has an azimuthal velocity equal to the wheel speed, and so it will already be above the limiting value as it enters the turbine shroud seal (as a rough estimate, the equilibrium azimuthal speed in the gland can be taken to be 50% of the wheel speed). Thus, some excitation of forward whirl will occur.

In an impulse turbine, the fluid enters the rotor seal at <u>twice</u> the wheel speed (i.e., with $\sim$ 150% of wheel speed in excess of the limit), and so we can expect excitation forces about three times larger than for a 50% reaction case. On the other hand, if guide vanes are introduced to cancel the inlet swirl in the near-wall region, we can expect a <u>reversal</u> of the excitation forces; this was actually observed by Wohlrab in one test. (Ref. 12).

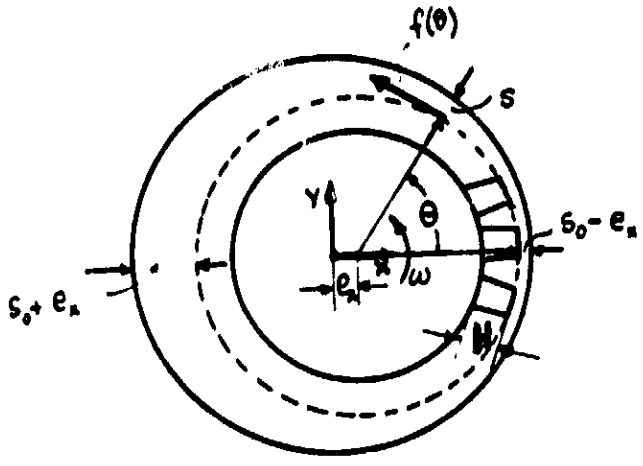

Fig. 1.2 Geometry for Alford's Model

The importance of these cross-forces on the rotor dynamic stability can be readily illustrated by a linear spring-mass-damper analysis (Ref.15). For a shaft of mass M and elastic stiffness Ko, assume the fluid effects produce forces

$$F_x = -K_{xx}\, x + K_{xy}\, y - C_{xx}\, \dot{x} + C_{xy}\, \dot{y} \qquad (1.1.5)$$

$$F_y = -K_{xy}\, x - K_{xx}\, y - C_{xy}\, \dot{x} - C_{xx}\, \dot{y} \qquad (1.1.6)$$

where x and y are the small cross-displacements of the shaft center during vibratory motion. It is then found that the complex displacement vector, $z = x + i\, y$, will vary (with no external excitation) as $\exp(i\Omega t)$, where

$$\frac{\Omega}{\sqrt{K_o/M}} = \pm 1 \pm \frac{i}{2}\, k_{xx} - \zeta_{xy} - i\, (\pm \frac{i}{2}\, k_{xy} - \zeta_{xx}) \qquad (1.1.7)$$

and

$$\kappa_{ij} = \frac{K_{ij}}{K_o} \quad , \quad \zeta_{ij} = \frac{C_{ij}}{2\sqrt{K_o M}} \qquad (1.1.8)$$

which are asssumed to be small in magnitude.

We notice that:

(a) One of the two modes of vibration (forward or backward whirl) will become unstable if $1/2|\kappa_{xy}| > \zeta_{xx}$, or $|K_{xy}| > \Omega_o\, C_{xx}$, where $\Omega_o = \sqrt{Ko/M}$ is tne undisturbed natural frequency.

(b) The effect of a direct stiffness K_{xx} on the cross-damping (xy) is a small modification of the whirl frequency away from the natural frequency.

Thus, unless the machine has sufficient intrinsic direct damping C_{xx}, or unless the fluid effects themselves provide it, an instability will result due to the cross-force stiffness K_{xy}. Thus, although the fluid effects are known to also produce direct stiffness K_{xx} of the same order as K_{xy} (Refs. 7, 12), most attention has been focused on the cross-effect. An exception to this has been the utilization of the stiffening effect of cylindrical seals to raise the natural frequency of the SSME turbopumps (Ref. 33).

1.2 Early Work on Clearance-Induced Excitation Forces

The seminal papers of Thomas and Alford have already been mentioned. Although their concepts were soon accepted and used by practicing engineers for design and diagnostic purposes, experimental confirmation was slow in coming, and then, mostly in Germany, and theoretical refinement is still lacking. Early tests of a limited nature, were made by Pollmann (Ref. 4) and Winter (Ref. 5), and later, more quantitative work was initiated by Thomas' co-workers at Munich (Ref. 6). This opened the way for the much more comprehensive series of tests carried out later by this same group, which we analyze in more detail in the two following subsections.

1.3 Review of K. Urlichs' work (1975) (Ref. 7)

This is the first of two major pieces of work performed at the Munich Technical University under the supervision of Dr. H.J. Thomas, both completed in 1975 (the other one is by R. Wohlrab and will be subsequently discussed).

Urlichs set out to refine, analytically as well as experimentally, the understanding of turbine tip excitation effects, with special emphasis on tip seal behaviour. Some passing attention was also paid to effects occuring in unshrouded blades. The author gives a review of previous work, by and large done in Germany. As is common in the European literature, the credit for identifying the transverse forces due to anisotropic tip clearance losses is given to H. J. Thomas for his 1958 work (Ref. 2), rather than to Alford (Ref. 1), as is more often done in the U.S. literature. The work of Winter at Darmstadt (Ref. 5) is mentioned as having reviewed and compared expressions for tip clearance losses. Traupel's book (Ref. 8) is often used as a basic source for such expressions, and the one used for reference throughout Urlich's (and Wohlrab's) work gives the side force excitation coefficient (one half of the Alford ß factor, in U.S. parlance) as

$$K_{i_S} = \frac{1}{2}\left[\frac{k'}{\sqrt{Z'}\sin\alpha_i}\,\frac{d_n}{d_m}\,\frac{\ell''}{\ell'} + \frac{k''}{\sqrt{Z''}\sin\beta_i}\,\frac{d_\ell}{d_m}\right]$$

where d_n is the stator seal diameter, d_ℓ the rotor seal diameter, d_m the mean blade diameter, ℓ' and ℓ'' the stator and rotor blade length, respectively, α_i and β_i the stator and rotor leaving angles (measured from the azimuthal direction) and Z' and Z" the respective stator and rotor number of sealing strips; k' and k" are dimensionless coefficients given in graphical form and having values of about 0.7 for unshrouded blading and from 0.2 to 0.8 for shrouded blades, depending on loading.

To this K_{i_S} must be added a similar K_{i_d} attributable to direct

pressure forces acting unevenly over the shroud surface. The overall K2 then determines the cross-force Q_{2s} as

$$Q_{2s} = K_2 \, U_s \, \frac{e}{\ell}$$

where U_s is the isentropic azimuthal force $\dot{m}\Delta h_s/U$ ($\dot{m}$ = mass flow rate, Δh_s = specific enthalpy drop for isentropic expansion, U = peripheral velocity). Also, e is the rotor eccentricity and ℓ the blade height.

Regarding the K_{2d} (pressure) component, Urlichs, after giving a physical explanation of the effects involved, discusses existing (to that time) calculational methods for seal excitation forces. Alford's paper (Ref. 1) is mentioned in this respect, not in connection with tip clearance forces, but in connection with his more controversial postulated effect of the axial variation of sealing gap width in labyrinths. As a general treatise on non-contact seals, Trutnowsky's book (Ref. 9) is quoted; however, on the specific area of excitation forces, Kostyuk's 1972 paper (Ref. 10) and Hochreuther's 1975 thesis (Ref.11) at Stuttgart are recommended. This is an area where significant advances have occurred after Urlichs' work and which we will review separately (Secs. 1.6, 1.7).

The body of the theoretical work of Urlichs is devoted to an elaborate model of the flow in non-contact gas seals, including both plane and labyrinth types. The flow is subdivided into a finite number of "streamtubes," each of which is itself subdivided along its length. This finite element approach has the peculiarity that the element corners are not predetermined, but are found in the process of the iterative calculation, somewhat akin to computational methods which use the stream function as an independent variable. The equations of continuity, momentum and energy are satisfied, making use along the way of a number of empirical coefficients to account for friction, flow turning, contraction, etc. The solution is found by a nested set of iterations. The presence of so many adjustable constants and the laboriousness of the process detract somewhat from the value of this work, but on the other hand, it does appear to have the flexibility required to effect computations for a variety of seal geometries and, as we will see, it can give good predictions on the presure patterns existing in off-centered seals.

More directly applicable is the part of the work devoted to the experiments. These were done in an air, open loop test rig, operating at near atmospheric pressure, with flow rates of up to 0.4 Kg/sec (which restricted the achievable Reynolds' numbers to below 10^5). Static rotor offsets only were considered, and these were obtained by displacing the casing on a fixed rotor. The rotor was supported on bearings mounted on a bar frame which allowed all translations, and which was restrained laterally by stiff load cells, and axially by thrust-relief cables. A counterweight was used to support most of the vertical load, and a brake to absorb the turbine

power (up to about 4 KW).

The rotor was about 32 cm in diameter, with blades 2 cm high and about 1.5 cm in chord. Stage pressure drops ranged up to 0.2 atm., yielding azimuthal forces U_s of up to some 100 N.

A great deal of effort went into making detailed measurements of the small pressure variations about the periphery of the rotor and stator seals. This was done using U-tubes, with precision down to $\sim$ 1 mm Hg (0.02 psi; or, about 1.4 mb) which proved sufficient, since most pressure patterns were roughly sinusoidal, with amplitudes of some 6 mb per 0.1 mm shaft offset. These measurements allowed the author to separate the contribution of pressure (K_{2_d}) and tip clearance variations (K_{2_s}) to the excitation cross-force.

The turbine tested had impulse blading, without and with shroud seals (and these with either 2 or 3 strips). With no shroud, K_2 was found to range from about 1 to 3, increasing markedly with the axial gap between stator and rotor, and decreasing as the mean radial gap increased. These trends are not predicted by the simple Alford (or Traupel) formulations, but the general trends with eccentricity (linearity was found) and load were as predicted and so was, in a general way, the value of K_2.

With shrouds, the efficiency increased substantially, particularly with the stepped 3-strip labyrinth. Simultaneously, the sensitivity of this efficiency to tip clearance was reduced, leading to the expectation of a reduced excitation coefficient. In fact, the measured K_2 was generally higher than without a shroud; the excess was shown to be consistent with the effect of the measured asymmetric pressure pattern on the shroud's outer surface, as well as with that predicted by the author's theoretical calculations (with proper selection of empirical constants). This pressure effect tended to account for 50% of the measured force.

With the apparatus used, no separation was possible between stator and rotor effects. However, some measurements were also reported on the effect of rotor inclination; these were found to be generally small and to have little effect on stability. Similarly, the forces in the direction of offset were also reported, but their effect is minimal, due to the competing effect of the large shaft stiffness.

1.4 Review of R. Wohlrab's work (1975) (Ref. 12)

In comparison to Urlich's work, the companion work by Wohlrab featured more realistic Reynolds' numbers (up to 2×10^5 based on inlet velocity, roughly 5×10^5 based on leaving velocity), while at the same time providing less detailed information on pressure distributions. Wohlrab also separated the stator and rotor effects by providing for independent offsets, and he verified his force measurements by means of direct kinematic (vibration) tests.

Wohlrab's theoretical discussion is similar to that of Urlich's, i.e., based on Thomas' and Traupel's simple theories. His report does not attempt any new analytical development.

The test apparatus was part of a closed air loop capable of pressurization up to 6 atm. and of flow rates up to 6-8 Kg/sec. With rotation rates up to 5000 RPM, the brake power was as high as 400 KW. The rotor was supported by two pairs of perpendicularly arranged load cells, with a cable to absorb thrust. As was mentioned, the rotor and stator casings could be separately displaced in the transverse direction, and axial displacement was also allowed. The turbines tested had a mean diameter of 46 cm and blade height of 4 cm. Wohlrab tested two 50% reaction stages (stage A, with many small buckets, B with larger, thicker blades), one impulse stage (stage C), and a 3-stage turbine similar to stage B. All the turbine rotors had sealed shrouds, but only that in stage C was a continuous band.

No attempt was made to map the pressure distribution over the seals. Instead only side and direct forces were measured and reported for a large variety of operating conditions.

With stage A, one surprising result was the finding that many of the curves of side force vs. offset were markedly nonlinear, some quite irregularly shaped. No explanation was offered for this, but a potential cause may have been the intrusion of measurement errors, since the forces were smallest for this particular stage ($K_2 \sim 0.5$). This smallness resulted from two causes: (a) The small chord of the blades, and (b) The small inlet swirl to the shroud seal, since 50% reaction blading was used. The measured K_2 was only about 1/2 of that predicted by Traupel's gap loss formula, a result which is also at variance with those for the other stages.

With stage B, featuring larger blades, k_2 was more linear with offset, and its magnitude was generally comparable with Traupel's prediction (although with scatter). Very similar results for K_2 were obtained from the 3-stage turbine, which had similar blading.

The results for stage C (impulse) are similar to those obtained by Urlichs, i.e., K_2 was found to be 2-3 times larger than the gap-loss prediction, with the excess being roughly explainable by the large pressure non-uniformity on the shroud surface. This was here a continuous band, and was subject to a strong inlet preswirl (the stator leaving angle was 13° only). The range of K_2 was from 2 to 3. The force was quite linear with displacement, also as in Urlich's case.

Wohlrab tested stage C for a range of air densities which must have varied the Reynolds no. between 2.5 and about 5×10^5 (based on chord and leaving velocity). Interestingly, this did not produce any significant variation in K_2; this is consistent with the existence of a critical

Reynolds no. range at lower values ($1\text{-}2\times10^{5}$), as will be discussed in Sec. 3.1.

The dominant effect of inlet preswirl was clearly demonstrated by adding meridional guide vanes in the labyrinth in stage C. With the vanes extending throughout the three glands, and hence probably cancelling the flow swirl, the value of K_2 went to essentially zero. Curiously, K_2 became negative when the vanes were placed only ahead of the first sealing strip. This can be understood in terms of our discussion of seal pressure effects in Sec. 1.1. With vanes throughout, both the inlet and the limiting velocities are zero, and no differential energization of gland swirling motion occurs. With only the inlet swirl cancelled, the limiting azimuthal speed is still of the order of half the wheel velocity, and so the flow enters below this limit, and reverse excitation can be expected.

Finally, Wohlrab modified the support system, suspending each bearing from bar springs and dampers, and performed vibration, or kinetic tests on the same turbines. The frequency of vibration (whirl frequency/rotation frequency of the order of 0.1) was, however, much lower than would be expected in an actual turbine of the same power, with the result that the tests can mostly be regarded as quasi-static in nature. This is compounded by the relatively poorer accuracy of the data collected in this manner. Wohlrab was able to obtain K_2 kinetic data which agreed fairly well with those obtained from force measurements, but his conclusion that velocity-dependent effects are unimportant does not appear justified from the data. This is a difficult area where more work is still necessary.

1.5 More Recent Work on Alford Forces

Vance and Laudadio (Ref. 13) have recently performed the only experimental measurements (to this author's knowledge) on Alford forces in the U.S. For their tests they used a small fan (torque under 0.1 Nm, speed to 7000 rpm) with a movable casing. The fan bearings were mounted on very flexible springs to allow measurement of the small cross forces (less than 10 grams). No attempts were made to measure airspeeds or pressures.

Vance and Laudadio confirmed the linearity of the cross-force with offset and with torque, but noticed a non-zero torque threshold below which these forces did not appear. The β factor was found to depend both on torque and on speed at constant torque, and was in the range of 0.5 to 2.5 (K_2 betwen 0.25 and 1.25). A three-parameter non-dimensional expression was proposed for the cross-force F_y, of the form

$$\frac{F_y D}{T} = f\left(\frac{x}{H}, \frac{D}{H}, \frac{V}{ND}\right) \qquad (1.5.1)$$

where D is diameter, T is torque, x is the offset, H the blade height, V the axial flow velocity and N the angular velocity. This would replace the simpler form $F_y D/T = \beta\, Tx/D\, H$ used by Alford, but the authors did not provide enough data to determine the functional form of (1.5.1).

1.6 Theoretical Understanding of Labyrinth Seal Forces

Early attempts to explain the occurence of strong cross-forces on eccentric labyrinth seals were based on extrapolations of known phenomena in journal bearings, such as Lomakin's effect, or oil whip. Alford, in his 1965 paper, postulated a mechanism for side force generation which was based on a non-symmetric rate of gas storage in a gland following an offset of the shaft. However, rapid equilibration can be expected due to azimuthal flows in the gland, and the effect may not be too significant.

We have also mentioned Urlichs' analysis of seal flows. His method applies probably more to a planar seal than to a labyrinth, although both are covered in the formulation. Starting with Kostyuk (Ref. 10), specialized fluid-mechanical formulations have been introduced and refined, generally based on linearization of the equations of conservation of mass, momentum and energy, written in integral form for each gland and supplemented by a few semi-empirical factors to account for friction, venacontracta and kinetic energy carryover. Representative of this line of analysis are Iwatsubo (Ref. 14) and Lee, et al. (Ref. 15), among others. Ref. 15 presented a comparison of the predictions of this linearized theory to the measurements of Ref. 21, and found agreement to within ± 20% over a wide range of parameters. The achievable accuracy appears to be limited mainly by uncertainty in the specification of discharge coefficients for flow over the sealing strips. The classical formulations of Egli (Ref.16), or Komotori (Ref.

17) have been used, but are insufficient for many geometries of interest. Turbulence modeling in two- or three-dimensional computational fluid mechanical calculations has also been tried, with only limited success in terms of accuracy (Ref. 18), which is not surprising considering the complexity of the recirculating, separated flows involved. Attempts at direct Navier-Stokes computational simulation of cavity flows of the same type are presently underway, and are capable of handling Reynolds numbers (based on clearance width and speed) of the order of 2000. An order of magnitude improvement is required for realism, and this may be achieved in a few years (Ref. 19).

1.7 Experimental Information on Labyrinth Seal Forces

Among the groups who have published data on the excitation effects of labyrinth seals, we will mention especially the work of Benckert and Wachter (Refs. 20,21), Leong and Brown (Refs. 22,23) and Wright (Refs. 24,25).

Benckert and Wachter used in their experiments a static-offset test rig with air flows of the order of 0.2 - 0.4 Kg/sec, and featuring a 30 cm diameter rotor mounting multicavity seal (up to 23 glands). Multiple pressure taps were used to obtain the circumferential pressure distributions in the various chambers, and the net forces were then obtained by integration of these measured pressures. The inlet swirl was controlled by means of inclined injection nozzles, and various types of sealing strip arrangements (straight-through, comb-type), with various chamber sizes and depths, were used. The results were presented in the form of non-dimensional force coefficients, covering a very wide range of parameters. These data have been the object of various correlations to theory, and constitute probably the most complete set existing. The one area not covered was that of dynamic seal effects, since only static rotor displacements were used.

The tests of Leong and Brown were similar in nature to those of Benckert-Wachter, namely, static deflection, multichamber seals. In Ref. 22 very small entry swirl was used, and negative whirl was seen to be excited. In Ref. 23 the entry swirl was higher, but still less than the rotor speed. As entry swirl increased, the excitation force became less negative and eventually crossed over to a positive value (excitation of forward whirl). Conversely, as the rotor speed increased, the tendency to negative whirl also increased. The authors mention similar earlier results of Greathead (Ref. 26), who put forward the hypothesis that forward whirl excitation would result if the entry swirl velocity exceeded the rotor speed, and vice versa. A more likely threshold is the equilibrium limiting azimuthal velocity in the seal, as discussed in Sec. 1.1.

Wright's tests differed from the others in that they were performed using a kinematic rig, i.e., by mounting the sealed rotor on flexible supports and inducing a vibrating or whirling motion (similar to some of Wohlrab's tests). The vibration was controlled by shakers with a feedback system designed to maintain neutral rotor stability at the natural rotor frequency (which was itself somewhat modified by the in-line seal forces). The feedback signals were used to infer the excitation forces. The mass flow rate was only 0.026 Kg/sec, giving a

Reynolds number below 4000, well below the transition to fully turbulent behavior; this makes extrapolation difficult to the levels of Reynolds number encountered in larger seals. One significant disadvantage of these tests was the lack of inlet swirl control. Since this is the crucial parameter affecting seal cross-forces, the results are difficult to interpret. Forward or backward whirling effects were encountered depending on seal configuration and whirling direction; this could possibly be due to varying amounts of friction-induced pre-swirl in the different cases. The different magnitudes of the cross-force for forward and backwards whirl could be used to infer seal damping forces, which have not been accurately measured elsewhere; the author chose not to present the data in this form, perhaps because the whirling frequencies were significantly different for the two directions.

Finally, pressure profiles taken with two diametrically opposite stationary transducers, were used to infer excitation fluid forces, and these were 30 to 45% higher than those obtained from the vibration tests. The author attributes this to the presence of non-pressure forces. The smallness of the effects measured (due to the lack of well defined inlet swirl) must be borne in mind, however.

2. The Prediction of Destabilizing Blade Tip Forces for Shrouded and Unshrouded Turbines

2.1 Introduction

As we have discussed in Sec. 1. while there is a fairly large body of analytical literature on the fluid forces due to labyrinth seals (Refs. 14 and 15, for example),the corresponding coverage on Alford forces is much more sparse.

In his pioneer paper, Alford (1) made an attempt to calculate the variation of the blade tip force. By assuming uniform upstream and downstreamflow fields, he was able to obtain an expression for the variation of blade tipforce from the knowledge of efficiency variation. But clearly, as a result of the clearance variation, the flow field can no longer beconsidered uniform, and these flow field perturbations may influence the resulting blade tip force. In this report an attempt has been made to calculate the effect of the non-uniform fields by using actuator disc theory. The ideas used here are based on those developed by Greitzer and Horlock (31). It will be shown that the non-uniformity cannot, in general,be ignored in the calculation of the destabilizing force. Within the limitations of the model, we have also included the effect of a time-varying eccentricity, or a finite whirl speed. Some values predicted by the model developed will be compared with those obtained experimentally by Urlichs (7) and Wohlrab (12), though an extensive testing against data is not possible because of a dearth of experimental data on the effects of variations of the blade tip gap. The possibility of using existing empirical turbine tip loss correlations to predict Alford forces is also explored.

2.2 The Model

The method of approach is to first find the flow field due to the tip clearance variation, and then, using the velocity triangles, to calculate the resultant Alford force. It is to be stressed that a complete three-dimensional investigation of the flow field with the non-uniform tip clearance is not attempted here.

Consider a single-stage turbine with its rotor whirling at a constant eccentricity e_o (Fig. 2.2.1). If the hub/tip ratio is high, the flow field can be approximated to be two-dimensional. Fig. 2.2.2 shows an actuator disc representing a two dimensional unwrapped blade row of circumference $2\pi R$, where w is the relative flow velocity and c is the absolute flow velocity. If the Mach numbers upstream and downstream are small, the flow can be considered incompressible, as well as inviscid, outside of the blade row.

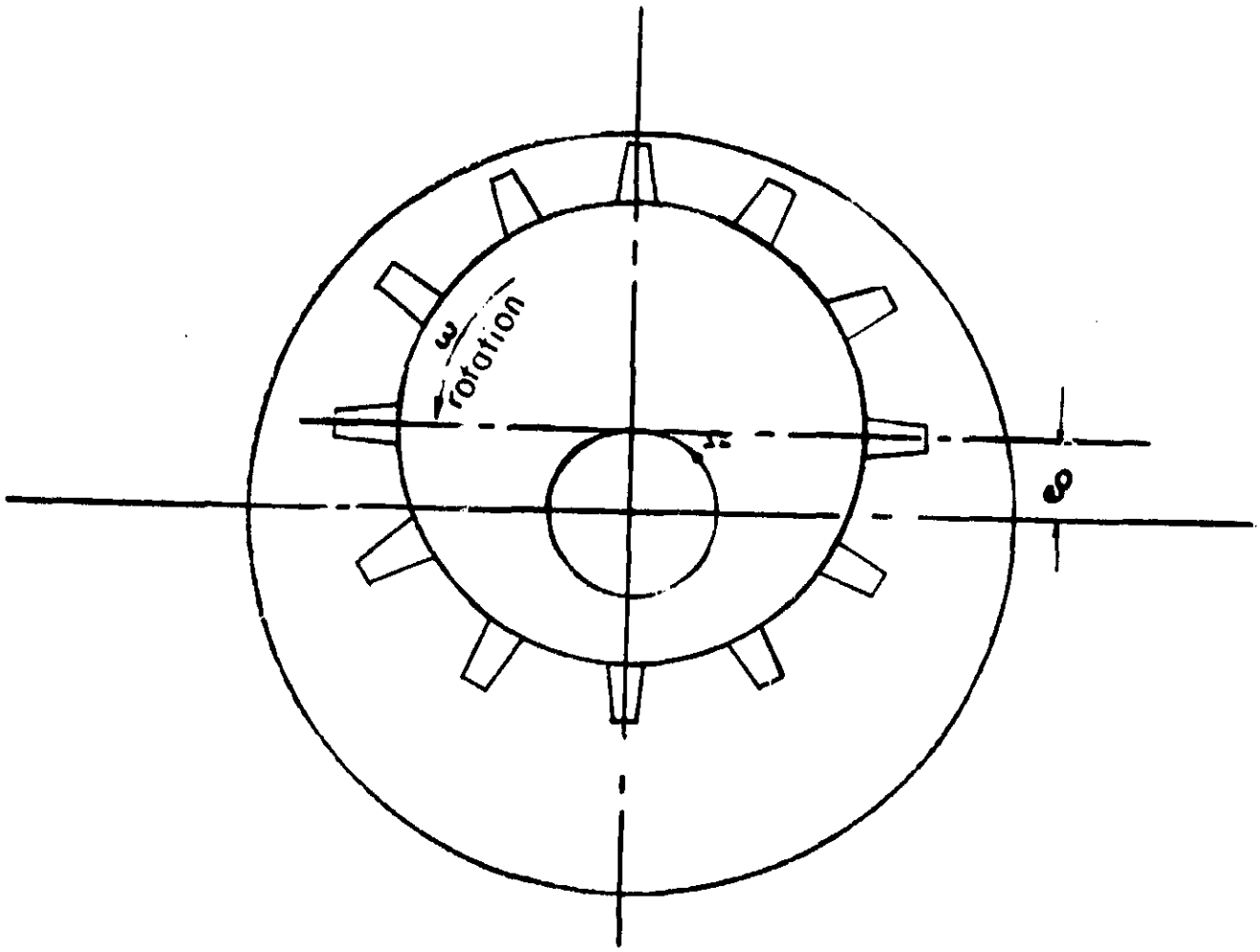

Fig. 2.2.1 Rotor under whirl

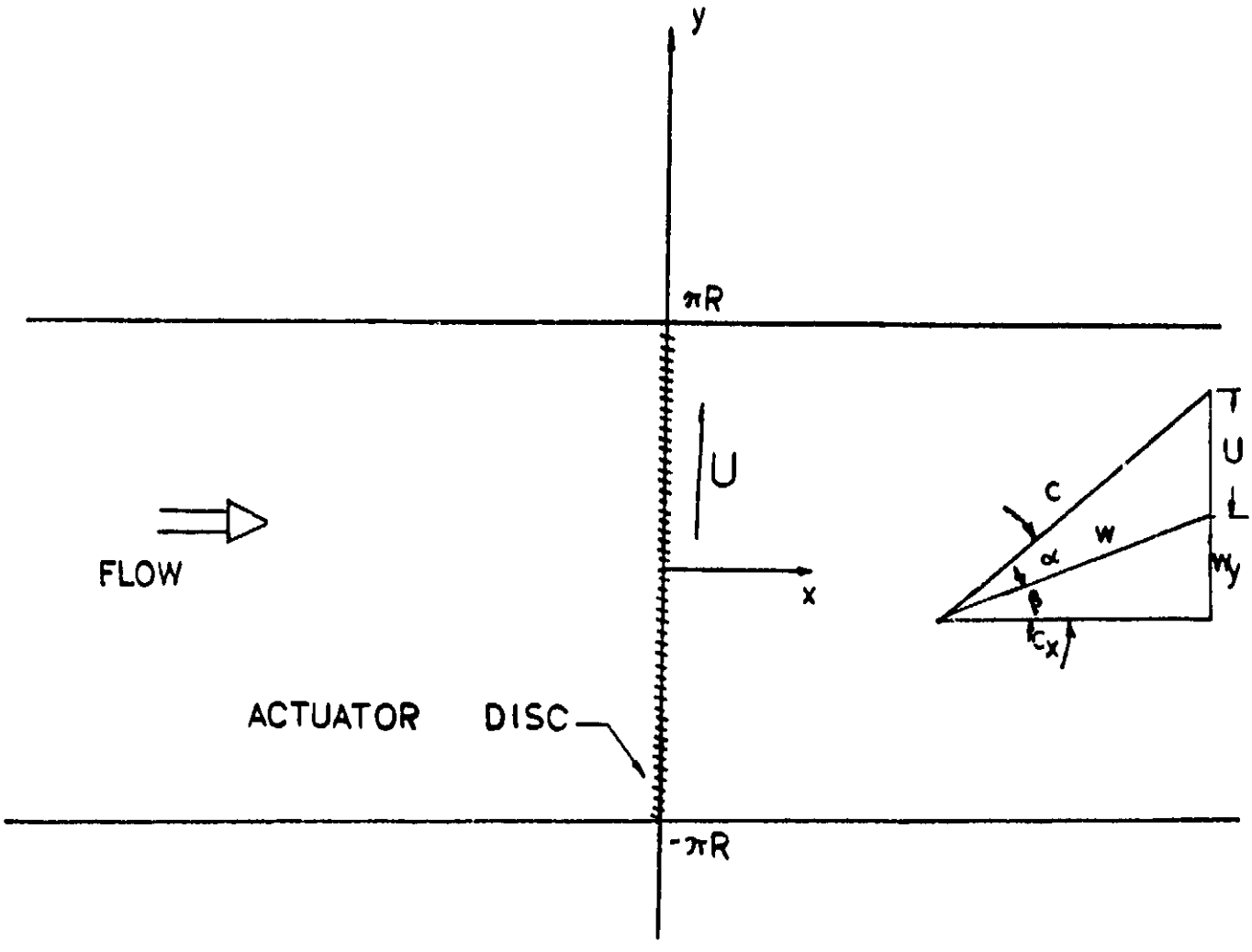

Fig. 2.2.2 Two-dimensional flow model

The variation of the tip clearance around the annulus can be represented by

$$\delta \frac{\tau}{H} = \Sigma E_n \left[i \frac{Y}{R} n - \Omega t i \right] \qquad (2.2.1)$$

where Ω is the whirling speed, Y is the distance in the tangential direction, R is the mean blade radius, H the blade height, and the E_n are constants.

Since only the first harmonic is of interest, as will be explained later, higher harmonics are not included in the analysis and $E_1 = e_o/H$.

The perturbation velocities c'_x and c'_y are related to the stream function ψ by

$$c'_x = \frac{\partial \psi}{\partial y} \qquad (2.2.2a)$$

$$c'_y = - \frac{\partial \psi}{\partial x} \qquad (2.2.2b)$$

Upstream of the stage, the flow is irrotational, $\nabla^2 \psi_1 = 0$ and downstream the flow is rotational $\nabla^2 \psi_3 = n$. The flow is steady in a reference frame rotating at the whirl speed Ω, therefore the stream functions can be written as

$$\psi_1 = A \exp \left[\frac{1}{R} (x + i y) - \Omega t i \right] \quad \text{upstream of the stage} \qquad (2.2.3)$$

$$\psi_3 = B \exp \left[\frac{i}{R} (- x + i y) - \Omega t i \right]$$

$$+ C \exp \left[\frac{i}{R} (- x \tan \bar{\alpha}_3 i + y i - \Omega t i) \right] \quad \text{downstream of the stage} \qquad (2.2.4)$$

where $\bar{\alpha}_3$ is the mean flow angle downstream of the rotor. Notice the irrotational term dies out far upstream and downstream. The vorticity downstream is convected by the mean flow at an angle $\bar{\alpha}_3$. Again only first harmonics are considered.

There are three matching conditions across the actuator disc surface:

1) The axial mass flux is constant

or
$$c'_{x1} = c'_{x3} \qquad (2.2.5)$$
$$\frac{\partial \psi_1}{\partial y}(o, y) = \frac{\partial \psi_3}{\partial y}(o, y)$$

2) The relative flow leaving angle is constant

$$\tan \beta_3 \, c'_{3x} = w'_{3x} = c'_{3y} + u' \qquad (2.2.6)$$
$$\text{at } x = 0$$

3) The third boundary condition involves matching perturbation quantities by using the known experimental information.

The total-to-static turbine efficiency can be written as

$$\eta = \frac{(c_{y3} - c_{y2})\, u}{c_p \, T_{01}\left(1 - \left(\frac{p_3}{p_{01}}\right)^{\gamma-1/\gamma}\right)} \qquad (2.2.7)$$

where c_{y2} and c_{y3} are the y-components of the absolute flow velocity before and after the rotor (defined positive in the y direction), u is the blade speed, p_3 is the static pressure downstream of the disc, and p_{01} is the total pressure upstream.

Due to the local blade tip clearance variation, the efficiency can be written as the sum of the mean efficiency and its perturbation:

$$\eta = \bar{\eta} + \eta' \qquad (2.2.8)$$

where to a first approximation

$$\eta' = \frac{\partial \bar{\eta}}{\partial (t/H)} \delta(t/H) + \frac{\partial \bar{\eta}}{\partial \beta_1} \delta \beta_1 \qquad (2.2.9)$$

It is known that the second term in the above expression is small compared with the first term, if β is not too far from the design value. Hence the second term in Eq.(2.2.9) will be ignored in the analysis.

Perturbing equation (2.2.7)

$$\eta' \, c_p \, T_{01}\left(1 - \left(\frac{p_3}{p_{01}}\right)^{\gamma-1/\gamma}\right) - \eta \, c_p \, T_{01}(\gamma-1/\gamma)\left(\frac{p_3}{p_{01}}\right)^{-1/\gamma+1} \frac{p'_3}{p_3}$$

$$= (c'_{y3} - c'_{y2})\, u + u'(\bar{c}_{y3} - \bar{c}_{y2}) \qquad (2.2.10)$$

All quantities are evaluated at x = 0.

Differentiating equation (10) with respect to y

$$\frac{\partial n'}{\partial y} Q_1 + Q_2 \frac{\partial p'_3}{\partial y} = \left(\frac{\partial c'_{3y}}{\partial y} - \frac{\partial c'_{y2}}{\partial y}\right) u + (\bar{c}_{y3} - \bar{c}_{y2}) \frac{\partial u'}{\partial y} \qquad (2.2.11)$$

where

$$Q_1 = c_p T_{01} \left(1 - \left(\frac{p_3}{p_{01}}\right)^{\gamma-1/\gamma}\right)$$

$$Q_2 = -\eta\, c_p\, T_{01} \frac{\gamma-1}{\gamma} \left(\frac{p_3}{p_{01}}\right)^{\gamma-1/\gamma} \frac{1}{p_3}$$

If we assume the leaving angle of the stator is also constant, then

$$\frac{\partial c'_{y2}}{\partial y} = \tan \alpha_2 \frac{\partial c'_{x2}}{\partial y} = \tan \alpha_2 \frac{\partial c'_{x1}}{\partial y} \qquad (2.2.12)$$

The momentum equation downstream of the rotor gives

$$-\frac{1}{\rho} \frac{\partial p_3}{\partial y} = \frac{\partial c'_{y3}}{\partial x} \bar{c}_{x3} + \bar{c}_{y3} \frac{\partial \bar{c}_{y3}}{\partial y} + \frac{\partial c'_{y3}}{\partial t} \qquad (2.2.13)$$

From (11), (12) and (13)

$$\frac{\partial n'}{\partial y} Q_1 + Q_2 \rho_3 \left[-\bar{c}_{x3} \frac{\partial c_{y3}}{\partial x} - \bar{c}_{y3} \frac{\partial c_{y3}}{\partial y} - \frac{\partial c'_{y3}}{\partial t}\right]$$

$$= \left(\frac{\partial c_{y3}}{\partial y} - \tan \alpha_2 \frac{\partial c'_{x1}}{\partial y}\right) u + \frac{\partial u'}{\partial y} (\bar{c}_{y3} - \bar{c}_{y2}) \qquad (2.2.14)$$

In terms of the stream functions, the three matching conditions can be written as

$$\frac{\partial \psi_1}{\partial y} = \frac{\partial \psi_3}{\partial y}$$

$$\frac{\partial \psi_3}{\partial y} \tan \beta_3 = - \frac{\partial \psi_3}{\partial x} + u'$$

$$\frac{\partial \eta'}{\partial y} Q_1 + Q_2 \rho_3 \left[\bar{c}_{x3} \frac{\partial^2 \psi_3}{\partial x^2} + \bar{c}_{y3} \frac{\partial^2 \psi_3}{\partial y \partial x} + \frac{\partial^2 \psi_3}{\partial t \partial x} \right]$$

$$= - u \left[\frac{\partial^2 \psi_3}{\partial x \partial y} + \tan \alpha_2 \frac{\partial^2 \psi_1}{\partial y^2} \right] + (\bar{c}_{y3} - \bar{c}_{y2}) \frac{\partial u'}{\partial y} \qquad (2.2.15)$$

Substitute Eqs. (2.2.3) and (2.2.4) into (2.2.15), (2.2.5), and (2.2.6):

$$A = B + C \qquad (2.2.16a)$$

$$(\tan \bar{\beta}_3 i - 1)B - (i \tan \bar{\alpha}_3 - i \tan \bar{\beta}_3)C = - \Omega e_o R \qquad (2.2.16b)$$

$$\tan \alpha_2 A + B \left[i - Q_2 \rho_3 \frac{\bar{c}_x}{u} (1 - i \tan \bar{\alpha}_3) - Q_2 \rho_3 \frac{\Omega}{\omega} i \right]$$

$$- C \left[+ \frac{\Omega}{\omega} Q_2 \rho_3 \tan \bar{\alpha}_3 - \tan \bar{\alpha}_3 \right] = \frac{R \lambda Q_1}{u} \frac{e_o i}{H} + \frac{\Omega R}{u} e_o i (\tan \bar{\alpha}_3 - \tan \alpha_2) \bar{c}_x \qquad (2.2.16c)$$

where

$$\lambda = \frac{\partial \eta}{\partial (t/H)}$$

To obtain the blade force variation, the momentum equation is applied across the rotor blades. The tangential component of the force is given by

$$f_y = \rho c_{x3} (c_{y3} - c_{y2}) H \qquad (2.2.17)$$

Since only the perturbation of force contributes to the resultant destabilizing force

$$f'_y = o\, c'_{x1}\, (\bar{c}_{y3} - \bar{c}_{y2})\, H + o_1\, \bar{c}_x\, (c'_{y3} - c'_{y2})\, H \qquad (2.2.18)$$

If we consider a reference frame rotating at the whirl speed Ω, and add together the forces perpendicular to the instantaneous eccentricity, we find the net cross-force

$$F_y = \int_0^{2\pi R} \mathrm{Real}(f'_y\, e^{\Omega t})\, \cos\,(y/R)\, d\, y \qquad (2.2.19)$$

This expression justifies the inclusion of only the first harmonic in the stream function expansion, since the higher harmonics contribute nothing to the Alford force.

A non-dimensional excitation coefficient k_{xy} is defined as

$$k_{xy} = \frac{Fy}{U_s} \,/\, \frac{eo}{H} \qquad (2.2.20)$$

where U_s is the ideal total force in the circumferential direction on the blade, and e_o/H is the dimensionless eccentricity.

2.3 Calculations and Comparisons to Data

Cases with stationary eccentricity are considered first. A typical plot of the axial velocity perturbation and the blade force variation vs. angular position are shown in Fig. 2.3.1. As was to be expected, these quantities are almost in counterphase with the tip clearance variation, which indicates that the non-uniform flow field will tend to increase the Alford forces.

Although Alford published his paper in 1965, very few experiments have been done to verify the proposed formula. Hence it is difficult to make any good comparison between the Alford model, the present analysis, and experimental results. Two tests were done by Urlich (7) and Wohlrab (12), and more recently Laudadio and Vance (13) did verify the linearity between the Alford forces and eccentricity for a fan. Accurate experimental data seems very difficult to obtain due to the small magnitude of the forces to be measured.

For the present analysis the data of Urlich seems to be the more suitable, since he also determined the efficiency vs. average clearance for an unshrouded turbine stage. From this information the values of

$$\lambda = \frac{\partial \eta}{\partial (t/H)}$$

are found by a second order polynomial curve fit to the efficiency vs. clearance data (Table 2.3.1). Values of k_{xy} are found by using λ, together with appropriate flow angles (Ref. 7) in the analytical model. The predicted values and experi-

mentally obtained values of k_{xy} are plotted in Figs. 2.3.2 and 2.3.3, together with the values of k_{xy} obtained from the Alford formula. It can be seen that the analysis gives a value of k_{xy} higher than the Alford formula, indicating that

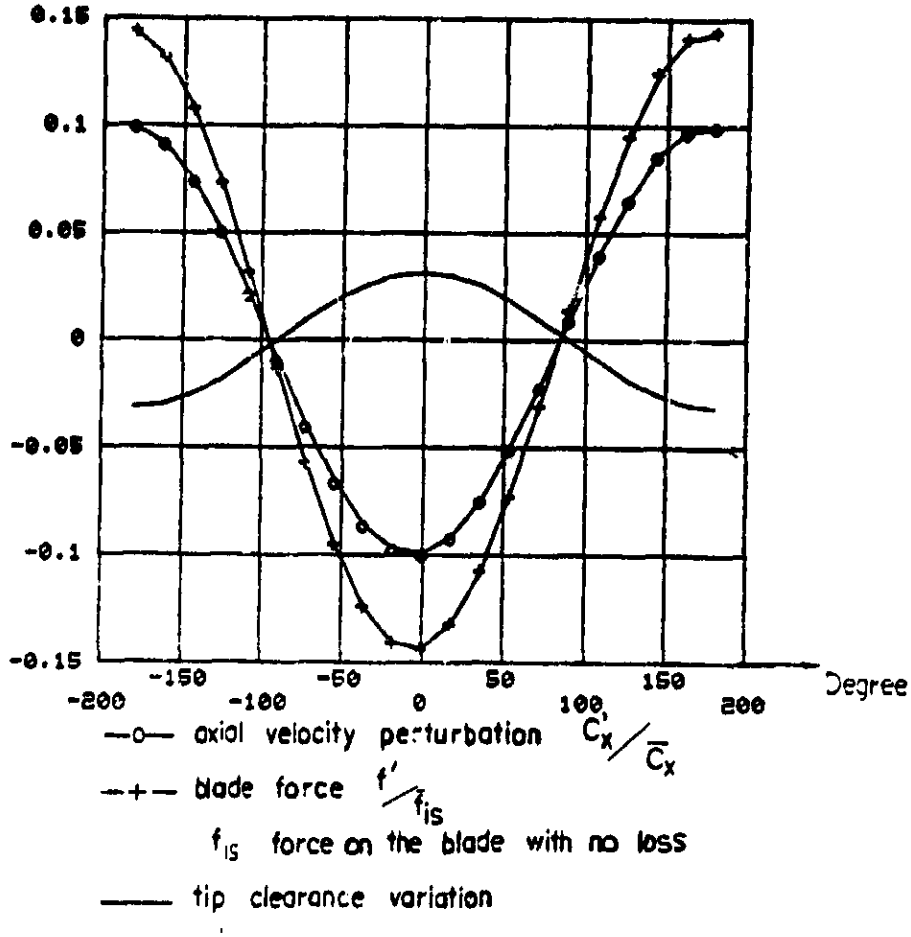

Fig. 2.3.1 Axial velocity and local blade force distribution

	radial clearance/blade height		
	2.6 %	5.3 %	7.8 %
axial gap 7.1 %	.705	.594	.521
21 %	.716	.570	.440

Table 2.3.1 Efficiency for tip clearances

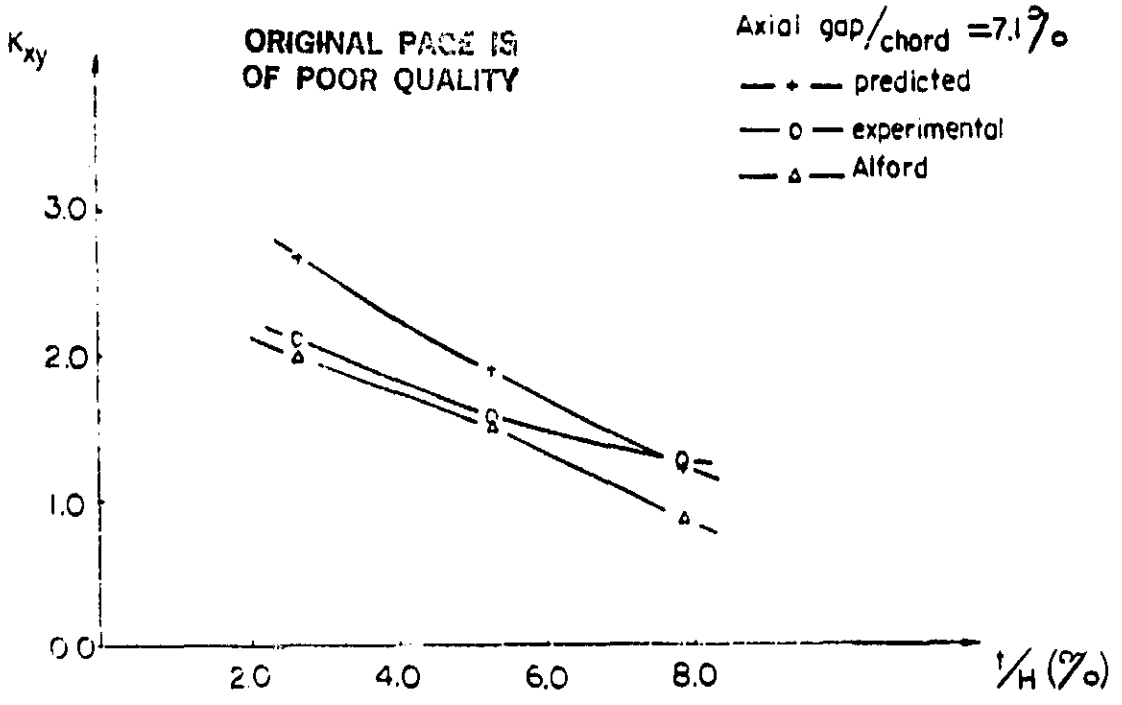

Fig. 2.3.2 Variation of excitation coefficient with tip clearance

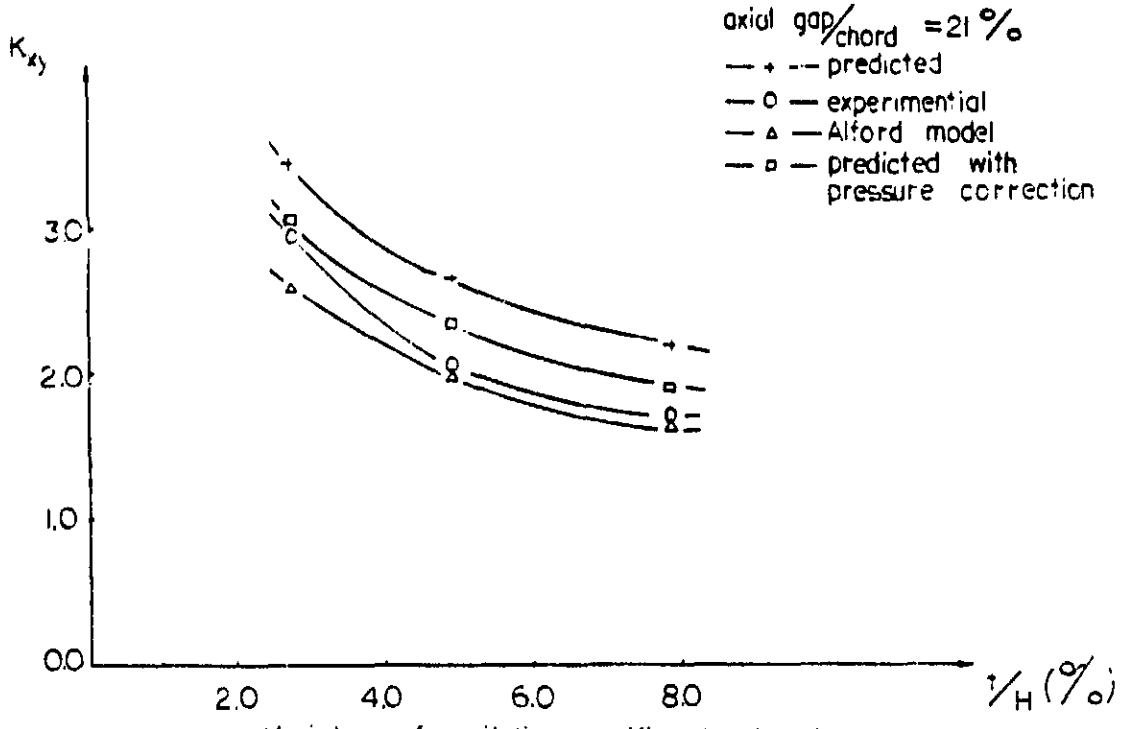

Fig. 2.3.3 Variation of excitation coefficient with tip clearance

the non-uniformity does increase the destabilizing forces.

In addition, it is also clear from Figs. 2.3.2 and 2.3.3 that the new theory overpredicts the side forces, when compared to the experimental data. However, we should at this point also consider the effect of the nonuniform pattern of pressure acting on the turbine wheel rim. Fig. 2.3.4 shows that, although the pressure field just upstream of the rotor is in phase with the clearance variation, it is shifted by 90° just downstream, and that those nonuniform pressures act in such a way as to reduce the forward cross-force.

A precise accounting of the effect of these pressure forces is not possible in the context of our actuator-disc theory. However, we can see that the 90° rotation of the pressure pattern must occur in the rotor passages, and so it is logical to calculate the induced side force by letting the rotated pressure wave act on an axial rim width equal to half a bladde chord. New excitation coefficients, including this pressure force, are also shown in Fig. 2.3.4. Although the precise axial length over which the pressure forces act is difficult to determine, it can be seen that they do contribute significantly to the net force, and that their effect is to substantially reduce the overprediction.

2.4 The Use of Tip Clearance Correlations

In many situations, curves of efficiency vs. clearance may not be available. The possibility of using some of the existing tip clearance loss correlations is investigated here. The formula used is given by Dunham and Came (34), which is a modified form of the methods of Ref. (32).

The correlation of loss coefficient vs. clearance is given by

$$Y_R = B \frac{c}{H} \left(\frac{t}{c}\right)^{0.78} Z \qquad (2.4.1)$$

where

$$Z = \left(\frac{c_L}{s/c}\right)^2 \frac{\cos^2 \alpha_2}{\cos^2 \alpha_m}$$

where t is tip clearance, c is true chord, c_L is the lift coefficient, α_m is the mean gas angle, constant B = .47 for unshrouded blades. B = .37 for shrouded blades. Assuming M << 1, then (Ref. 35)

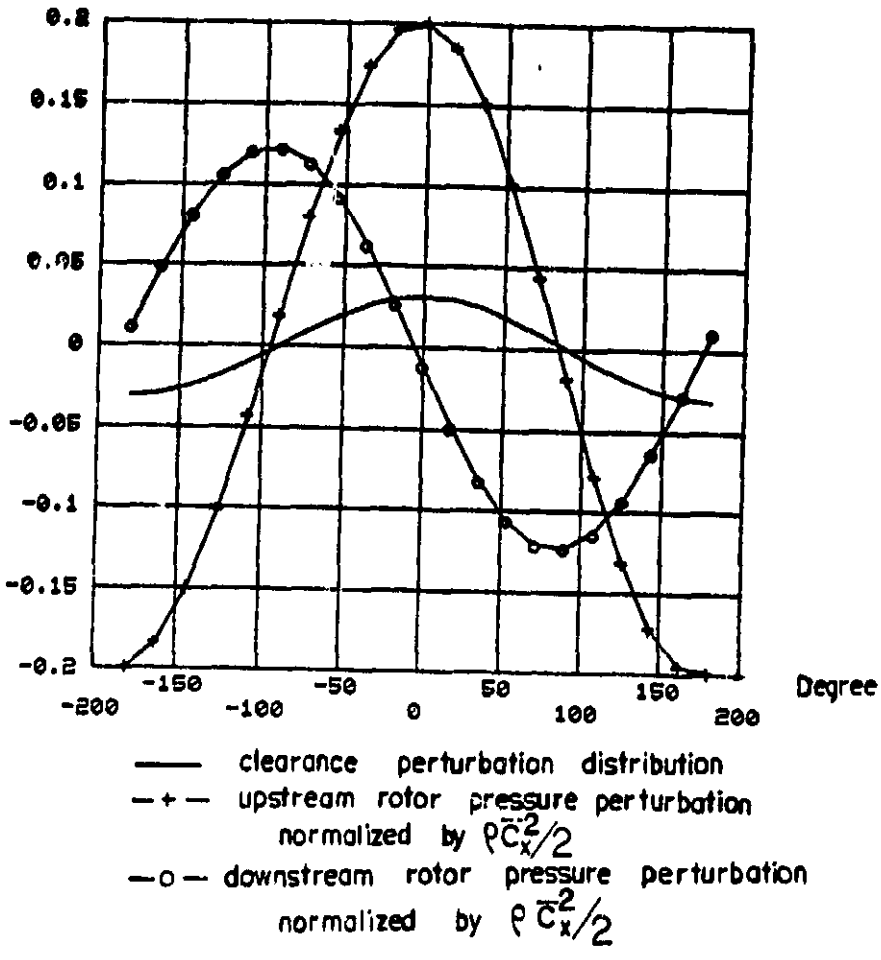

Fig. 2.3.4 Pressure perturbation distribution

$$\eta_{Ts} = \frac{1}{1 + \left[\frac{V_R W_3}{2} + \frac{T_3}{T_2}\frac{Y_N c_2^2}{2} + \frac{c_3^2}{2}\right]/(h_{01} - h_{02})}$$

$$\frac{\partial \eta_{Ts}}{\partial (t/H)} = -(\eta_{Ts})^2 \frac{w_3^2}{2(h_{01} - h_3)} \cdot 37\,(c/t)^{0.22}\left(\frac{c_L}{s/c}\right)^2 \frac{\cos^2 \alpha_2}{\cos^3 \alpha_m} \qquad (2.4.2)$$

(stator effects have been ignored because the stator is normally better sealed). Fig. 2.4.1 shows the predicted Alford forces based on Eq. (2.4.2), together with the experimental results. It can be seen that the prediction is very reasonable, as it compares well with the data for small axial (stator-rotor) gap, although not as well for large axial gap. The fact that k_{xy} varies with the gap between the rotor and stator is not well understood, and it may be highly dependent on the detailed geometrical arrangement of stator and rotor.

Wohlrab (Ref. 12) tested a shrouded turbine. Since he did not supply data on efficiency vs. tip clearance, λ has to be estimated, in order to compare the present analysis with the experimental values obtained. Encouraged by the results for the unshrouded turbine, an estimated tip loss coefficient is used again, but this time the effective tip clearance is given by (Ref.(34)).

$$t = (\text{geometric tip clearance}) \times (\text{number of seals})^{0.42}$$

Since there is also a shroud, we would expect some seal forces acting on the rotor shroud band. These are found by applying a model developed by Lee, et al. (15). The results (Fig. 2.4.2) again show reasonable agreement, falling between the data obtained by Wohlrab for the two axial gaps tested.

2.5 The Effect of a Time-Varying Eccentricity

All the cases examined so far have been for an assumed static offset. The effect of whirl for a typical case is shown in Fig. 2.5.1. For a whirl speed equal to 50% of the rotating speed, the effect on k is small (± 10%). This is consistent with Wohlrab's experiment, in which he found that within experimental accuracy there is no difference between the values of k_{xy} obtained from kinetic and static tests. It is noted, however, that the predicted effect of whirl (which could be expressed as an Alford damping coefficient), could not have been obtained from the original Alford model, since it depends crucially on the delays between wheel motion and disc passage of the induced flow non-uniformities, and these were ignored in the Alford model.

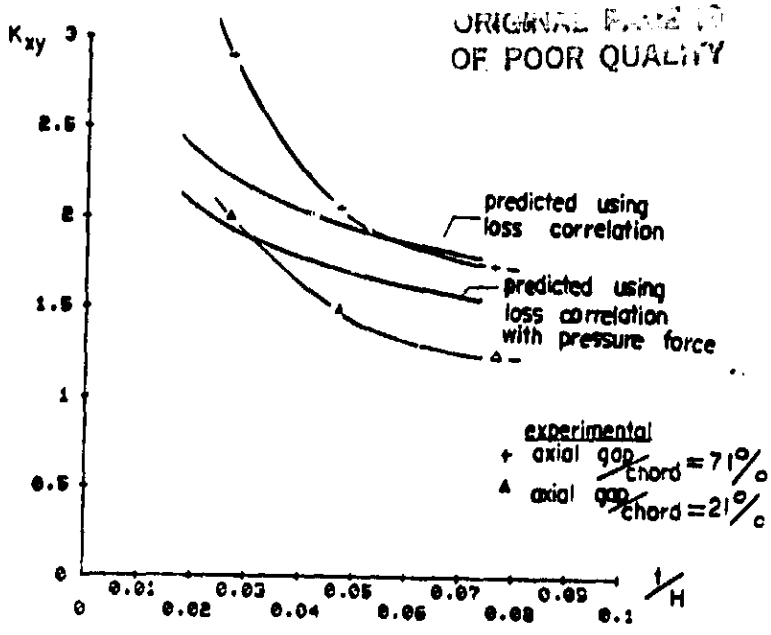

Fig. 2.4.1 Variation of excitation coefficient with tip clearance

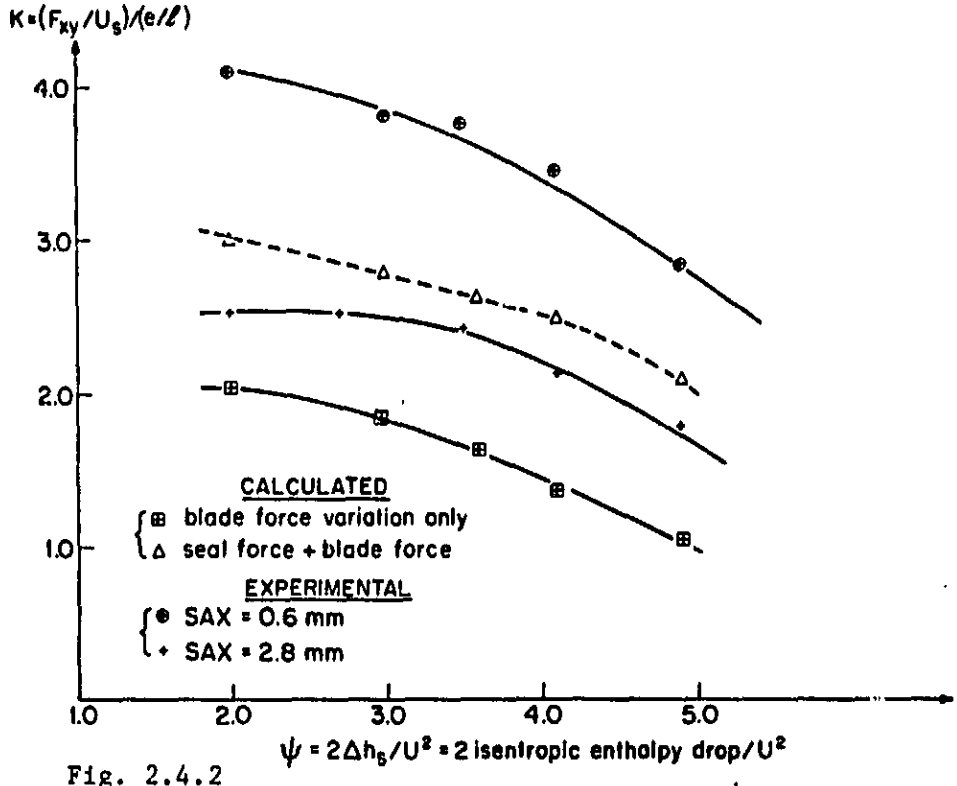

Fig. 2.4.2 CLEARANCE EXCITATION COEFFICIENT VS. ψ

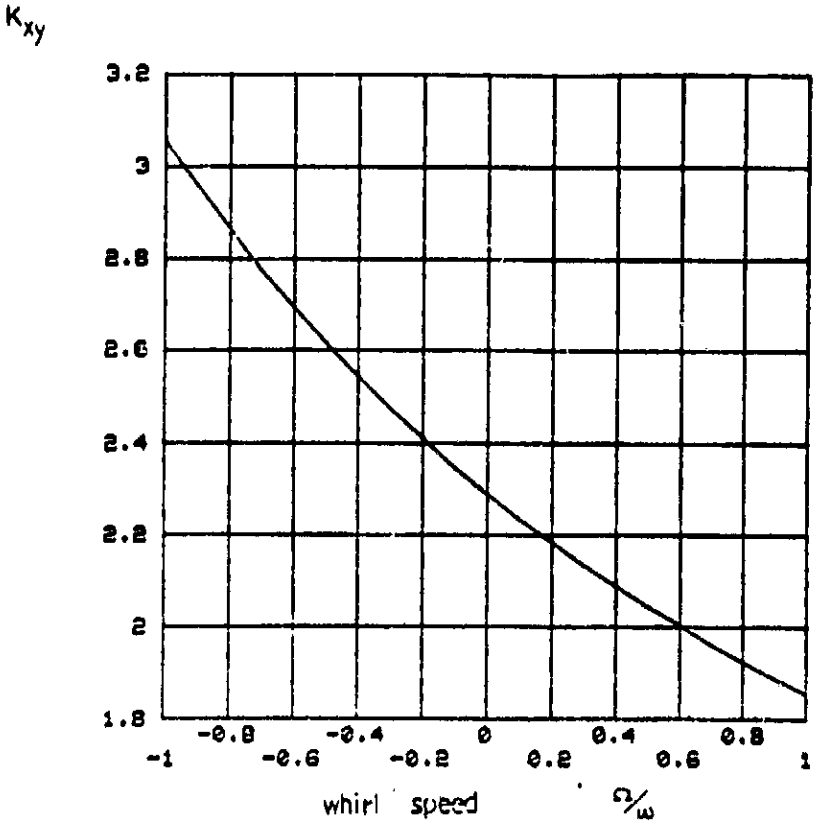

Fig. 2.5.1 Effect of Whirl

2.6 Conclusions

The non-uniform flow field induced by the tip clearance variation tends to increase the resultant destabilizing force over and above what would be predicted on the basis of the local variation of efficiency. On the one hand, the pressure force due to the non-uniform inlet and exit pressure also plays a part even for unshrouded blades, and this counteracts the flow field effects, so that the simple Alford prediction remains a reasonable approximation. Once the efficiency variation with clearance is known, the present model gives a slightly overpredicted, but reasonably accurate destabilizing force. In the absence of efficiency vs. clearance data, an empirical tip loss coefficient can be used to give a reasonable prediction of destabilizing force. To a first approximation, the whirl does have a damping effect, but only of small magnitude, and thus it can be ignored for some purposes. To gain more insight and understanding, more accurate experimental determinations of the tip force must be made. It must be pointed out that the destabilizing force is also highly dependent on the geometry of the rotor and stator, as shown by the experimental dependence of the magnitude of destabilizing force on the axial gap between the stator and rotor. This effect of axial gap on the Alford force points to the need for more detailed study of the flow field around tip regions.

3. Preliminary Design of the Test Facility

3.1 Introduction

As was pointed out in Section 1 of this report, the best existing data on Alford forces are those of Urlichs (Ref. 7) and Wohlrab (Ref. 12), who covered a fairly broad range of parameters, including some preliminary work on dynamic effects. In our experimental work, we propose to follow in the main their approach and capitalize on their experience wherever possible, while at the same time attempting to improve on their results on several specific points: (a) Higher Reynolds number, (b) More complete instrumentation, (c) A more clear separation of effects. As a result of correlating such data with theoretical analysis, we hope to derive a clearer picture of the mechanisms responsible for these forces in turbines of practical interest and to lay the basis for more advanced and accurate predictive methods.

We offer in this subsection a discussion of the test objectives and their impact on facility design. We wish to measure for representative turbines the side forces due to rotor side deflections, as a function of turbine configuration and operating point. In addition, we wish to obtain generic information about the mechanisms responsible for these forces.

First of all, the test turbines must be representative of those of interest for aerospace applications. This means on the one hand a suitable selection of such factors as stage loading and flow angles, which implies mostly geometric replication of some blading of practical interest, but it also means testing at realistic Mach and Reynolds numbers. In our case, since the focus of interest is the SSME turbopumps, the geometry selection is clearly indicated, as we will more fully discuss in Sec. 3.2. The Mach numbers in the SSME turbines are generally low enough as to play only a minor role in their performance, and this is true of many other turbines of interest; hence we simply choose a test design with also a "low" Mach number; namely, no more than, say, 0.3 (axial).

The Reynolds number, on the other hand, poses more difficulties, since their typical SSME values are of the order of 4×10^6 based on chord and leaving velocity. It is well known that Reynolds number (Re) effects become weak at high Re, and, more importantly, are fairly well predictable once fully turbulent operation is established over most of the blading. However, the dependence is stronger at lower Re, in the laminar regime, and, worse yet, it is much more diffficult to predict in the range of laminar-turbulent transition (Re ≈ 100,000 200,000 typically), where factors such as blade aspect ratio, solidity, roughness and free-stream turbulence can play an important role in determining blading performance. Some examples of this behavior are shown in Figs. 3.1.1 and 3.1.2, from Refs. 27, and 28, respectively. These transitional effects occur at

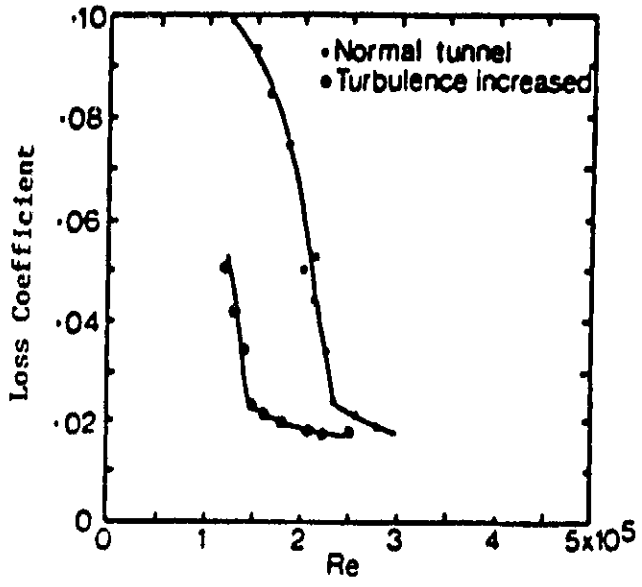

Fig. 3.1.1 Variation of loss coefficient with Reynolds' number.

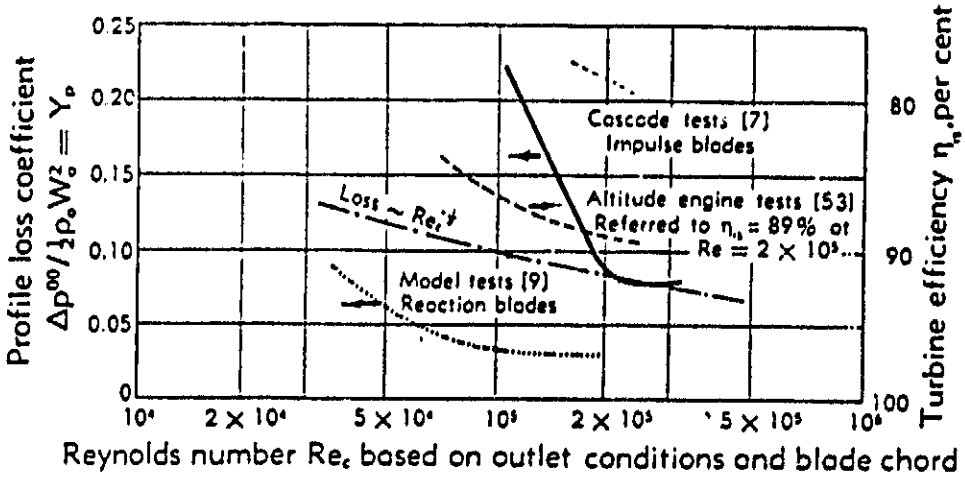

Fig. 3.1.2 Effect of Reynolds number on performance of turbine blading.

somewhat higher Re for low reaction blading.

Unfortunately, it is not very easy to obtain Reynolds numbers above this transition region in standard laboratory tests. Thus Urlichs (Ref.7) with an open-loop test rig supplied with 0.4 Kg/sec of air, and with dimensions close to those used here (i.e., blade chord about 2cm, radius of about 18 cm) was limited to Re values well below 10^6. Wohlrab (Ref.12), by using a much larger air supply in a closed loop circuit (up to 6 Kg/sec), and with blading about twice the size was able to obtain some data at Re $\approx 3\times10^6$, although his nominal operating point was closer to 1.5×10^6. The data of Vance (Ref.13) are for much lower Reynolds numbers.

Our approach, to be discussed more fully in Secs. 3.3, 3.4, consists in switching to Freon-12 as the operating gas in a closed loop facility. For the same pressure, temperature, characteristic dimension and Mach number, the Reynolds no. varies like $\sqrt{\gamma M}/\mu$, where γ is the specific heat ratio, M is the molecular mass and μ the viscosity. This "figure of merit" is compared for air and Freon-12 in Table 3.1.1. Another relevant comparison is that of "fluid power" $\rho v^3 L^2$ (a measure of, for instance, the required compressor or brake power for the facility. Imposing once again the same size, P, T and Mach number, this power scales as the group $\gamma^{1/2}/M^{1/2}$, which, using air as a reference, has a value of 0.35 for Freon-12. These are important advantages, and they allow us to design a reasonably sized test facility (Sec. 3.4) operating at a design Reynolds no. greater than 4×10^6. This is well past the critical "break" value of $\sim 2\times10^6$, even for impulse turbines, and comes to within extrapolation range of the actual Re values.

Gas	M(g/mole)	γ	μ(Kg/(msec))	$\frac{\sqrt{\gamma M}}{\mu}$	Same, relative to air
Air	28.9	1.4	1.8×10^{-5}	3.53×10^5	1
Freon-12	120.9	1.12	1.25×10^{-5}	9.31×10^5	2.64

Table 3.1.1 Factor for Reynolds number at fixed P, T, length, Mach no.:

$$R_e = \frac{\rho u L}{\mu} = \frac{PML}{\sqrt{RT}}\left(\frac{\sqrt{\gamma M}}{\mu}\right)$$

(M = Mach no, R = universal gas constant)

Table 3.1.1 Comparison of Air and Freon-12 Properties.

Regarding instrumentation, the primary measurements are the offsets and lateral forces, plus the turbine state variables. Beyond that, rings of pressure taps in the blade tip regions provide help in interpreting the data and give information on the phenomena. This is the level of instrumentation used by previous workers (Refs.7,12,13). In addition to this, we plan to introduce two scanning measuring rings, upstream and downstream of the stage, equipped with hot wire or three-hole pressure probes. This will further clarify the flow field by giving information on the azimuthal flow redistribution induced by the eccentric gap, and therefore will allow direct correlation to our actuator-disc theory (Ref.33), or perhaps some more refined theories in the future. Automatic digital data recording and processing is also expected to facilitate the experimental process.

Alford forces are known to arise at a variety of locations, including the blade tips, the shroud seals in shrouded turbines and the stator seals. In addition, our calculations (Ref.33) indicate an important hub pressure contribution. Wohlrab introduced separate control of stator and rotor eccentricity in order to separate their contributions. We retain this feature in our design and, in addition, we will verify the validity of this approach by testing with a special seal (see Sec. 3.7.2) designed to minimize stator-induced Alford forces. Our instrumentation ring will provide a means of exploring the near-hub pressures in order to assess their contribution to the side force.

Wohlrab (Ref.12) also performed dynamic vibration tests in his apparatus. Within the error tolerances, he found the effect of velocity-dependent forces to be much less significant than that of the displacement-dependent forces. This may have been in part due to the relatively low frequencies involved, since theoretical calculations on labyrinth seal forces (Ref.15) indicate a potentially significant damping effect. To clearly isolate this effect we plan to perform forced whirl tests in seals identical to those used in the turbine tests. These will be done in a separate seals test facility being built under a different program (see Sec. 3.11.1). In addition, dynamic whirl tests will also be conducted using the basic turbine test rig, in order to assess the importance of velocity-dependent blade tip forces. These tests will be at realistic reduced frequency. (See Sec. 3.7.4).

3.2 Test Turbine Parameters

The Space Shuttle Main Engine (SSME) utilizes in its propellant pressurization system two highly loaded two-stage turbines, one unshrouded (fuel turbopump) and one shrouded (LOX turbopump). These are of direct interest in terms of potentially destabilizing Alford forces, and are also representative of other turbines in high power turbomachinery. Table 3.2.1 summarizes the nominal characteristics of the first-stage blading of each of these turbines (100% power, baseline), and Fig. 3.2.1 shows their geometry.

Table 3.2.1 Characteristics of SSME Fuel and Oxydizer Turbine Blading (1st stages).

	Fuel Turbine	LOX Turbine
Stator leaving angle, α_2	70°	77.5°
Rotor leaving angle, β_3	60°	65°
Mean radius, r_m	12.88 cm	12.8
Number of blades	63	78
Blade height, h	2.17 cm	1.26
Blade chord, c	2.21 cm	1.65
Rotation rate, ω	34560 rpm	27100 rpm
Working gas molecular mass, $\mathcal{M}$	3.75 g/mole	3.30 g/mole
Working gas specific heat ratio, γ	1.352	1.374
Mass flow rate, $\dot{m}$	71.8 Kg/sec	28.0 Kg/sec
Inlet pressure, p_1	3.495×10^7 Pa	3.458×10^7 Pa
Pressure ratio, p_1/p_2	1.192	1.227
Inlet Temperature, T_1	1053 K	782 K
Efficiency	0.821	0.749

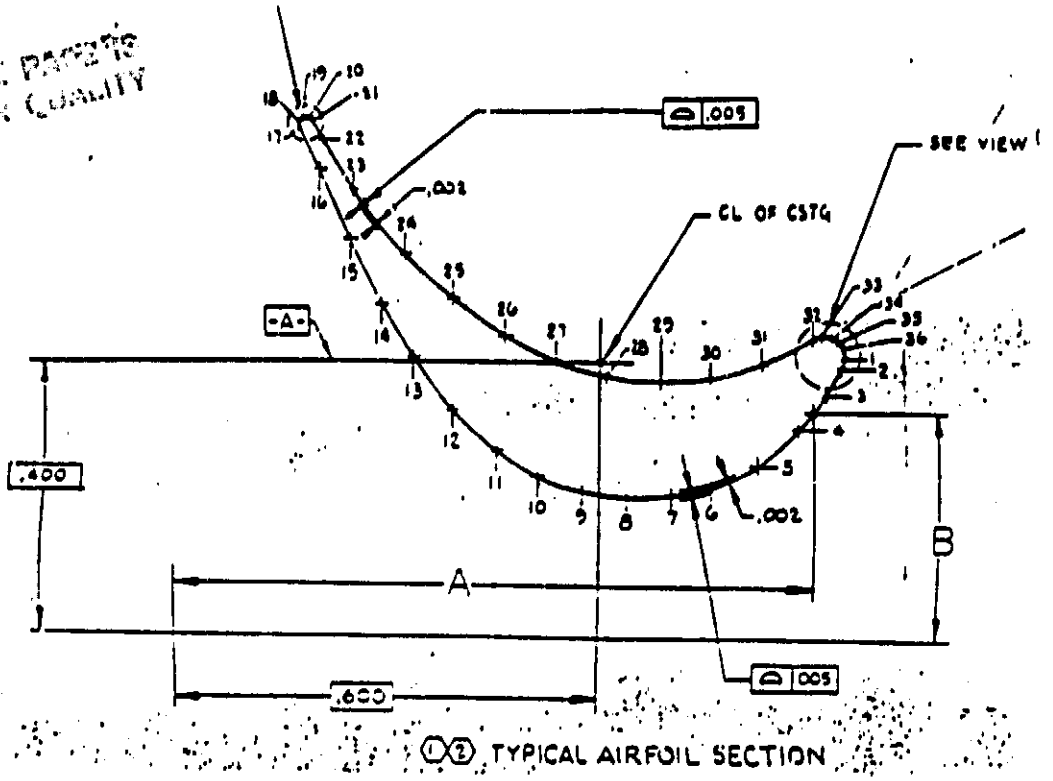

Fig. 3.2.1(a) Typical HPFT 1st Stage Blade Profile

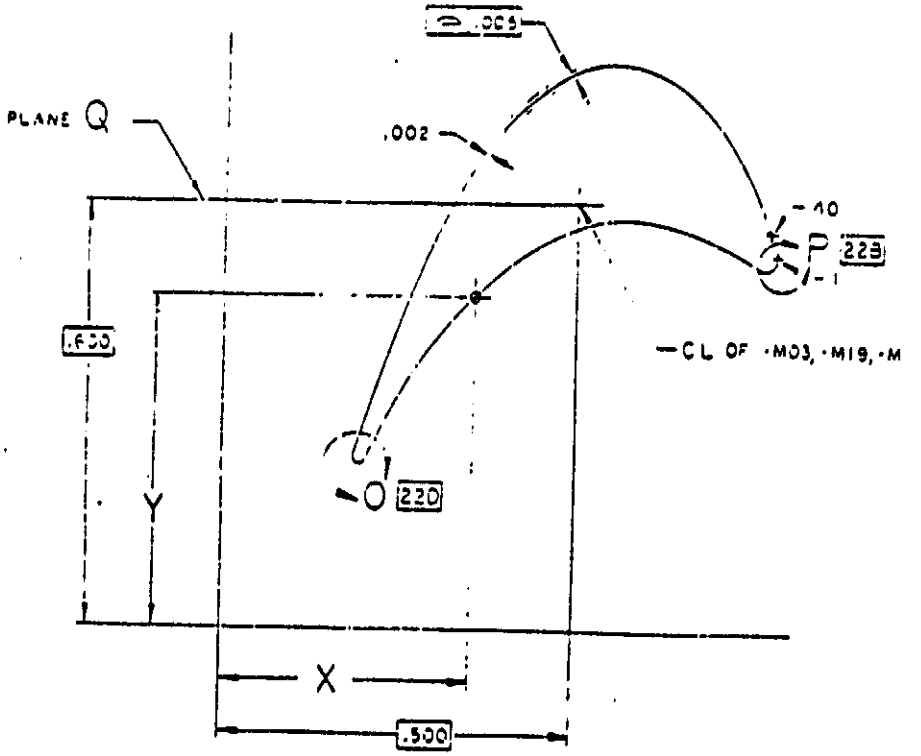

Fig. 3.2.1(b) Typical HPOT 1st Stage Blade Profile

The geometry for the relevant velocity triangles is shown for reference in Fig. 3.2.2, where solid lines represent absolute

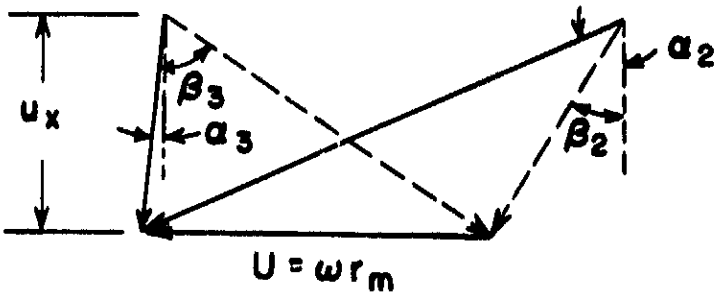

Fig. 3.2.2 Turbine Velocity Triangle.

velocities and dotted lines are velocities relative to the rotor. Subscript (2) refers to rotor inlet, subscript (3) to rotor exit, and α and β are absolute and relative flow angles, respectively. Important non-dimensional factors are the stage loading parameter:

$$\psi = \frac{\text{Specific enthalpy extraction}}{U^2} = \frac{u_x}{U}(\tan\beta_2 + \tan\beta_3) \qquad (3.2.1)$$

$$= \frac{n\, c_p\, T_1[1 - (p_2/p_1)^{\gamma-1/\gamma}]}{U^2} \qquad (3.2.2)$$

and the degree of reaction:

$$R = \frac{\text{Static enthalpy drop in rotor}}{\text{Total static enthalpy drop}} = \frac{\tan^2\beta_3 - \tan^2\beta_2}{\tan^2\beta_3 - \tan^2\beta_2 + \tan^2\alpha_2} \qquad (3.2.3)$$

From the leaving angles α_2, β_3 and the geometry,

$$\tan\beta_2 = \tan\alpha_2 - \frac{U}{u_x} \qquad (3.2.4)$$

$$\tan \alpha_3 = \frac{U}{u_x} - \tan \beta_3 \qquad (3.2.5)$$

In these expressions, the axial velocity u_x is assumed constant through the stage, and it can be calculated as

$$u_x = \frac{\dot{m}}{\rho_1 \, 2\pi r_m H} \qquad (3.2.6)$$

These expressions, with the values in Table 3.2.1, give the following derived quantities (Table 3.2.2):

Table 3.2.2 Calculated Parameters for Same Blades as in Table 3.2.1.

	Fuel Turbine	LOX Turbine
Inlet density, ρ_1	14.6 Kg/m^3	16.8 Kg/m^3
Axial speed, u_x	262 m/sec	164 m/sec
Relative rotor inlet angle, β_2	43.9°	66.5°
Absolute exit angle, α_3	-3.1°	3.6°
Loading parameter, ψ (from Eq.3.2.1)	1.508	2.07
Loading parameter, ψ (from Eq.3.2.2)	1.509	2.02
Degree of reaction, R	0.216	-0.033
Leaving velocity (relative, $u_x/\cos \beta_3$)	524 m/sec	388 m/sec

Both turbines are seen to be highly loaded. Also, since the speed of sound in the working gas is about 1850 m/sec, all Mach numbers involved are rather low. This means that the specific heat ratio, γ, should play only a secondary role in similitude considerations.

The Reynolds number based on chord and relative exit velocity is 5.6×10^6 for the fuel turbine and 3.4×10^6 for the LOX turbine. These are very difficult values to reproduce in experiments at moderate pressures, as commented in Sec. 3.1 but, as stated, we plan to be well above the transition Reynolds number of $1\text{-}2 \times 10^5$.

We choose to base our first test turbine design on the 1st stage of the SSME fuel turbopump. Besides the obvious interest on this particular design, there are some practical advantages to us in the fact that the aerodynamic design of these blades is available in the form of detailed drawings and tables of coordinates. In this sense, the simplest choice of size would be 1:1 scaling, which would allow the use of spare SSME blades as blanks for casting the test blades. We will therefore investigate the practicality of this choice in conjunction with that of working fluid in Sections 3.3, 3.4.

Since the nominal flow rate for the LOX turbine is smaller than that for the fuel turbine and its pressure ratio is only slightly larger, the facility can be easily modified for this other blading.

3.3 Air Flow Open Loop Design

With the above test turbine parameters in mind, we now explore the possibility of using existing Gas Turbine Lab air supply equipment. These systems, together with their design operating conditions, are listed in Table 3.3.1.

It is clear that both the oil free system and steam injector are not suitable. The measured characteristics of the steam ejector are shown in Fig. 3.3.1; at a pressure ratio of 1.2 the available flow rate is only of the order of 0.40 Kg/sec (1 lb/sec), which would lead to a very small operating Reynolds number. The same is true of the oil free system. Even though it has a storage facility, the pipes connected to the storage are only 10.2 cm (4") in diameter and the distance from the storage facility to the test section is relatively long, which makes it impossible to get a large mass flow rate.

The blower can deliver sufficient pressure, although at a relatively low mass flow rate. A performance diagram of the blower obtained in a different experiment is shown in Fig. 3.3.2. For purposes of comparison with our chosen configuration, we will here design the test facility such that this blower operates at a pressure ratio of 1.2 and a flow rate of 100 m^3/min. Also, we will design a test turbine which has the same pressure ratio, load coefficient, degree of reaction, and blade leaving angles as the 1st stage of the SSME fuel turbine.

Table 3.3.1 Characteristics of Available Air Supplies

	De Laval Compressor	Oil Free System	Air blower	Steam ejector
Max. pressure ratio	3:1	100/14.6	1.30	1.2
Flow rate	8.7 Kg/sec	0.32 Kg/sec	2.2 Kg/sec	0.22 Kg/sec

We can write the load coefficient ψ as in Eq. (3.2.2), and solve for the mean blade speed

$$U = \sqrt{\frac{\eta_t c_p T_1 (1 - \pi_t^{-(\gamma-1)/\gamma})}{\psi}} \qquad (\pi_t = p_2/p_1) \qquad (3.3.1)$$

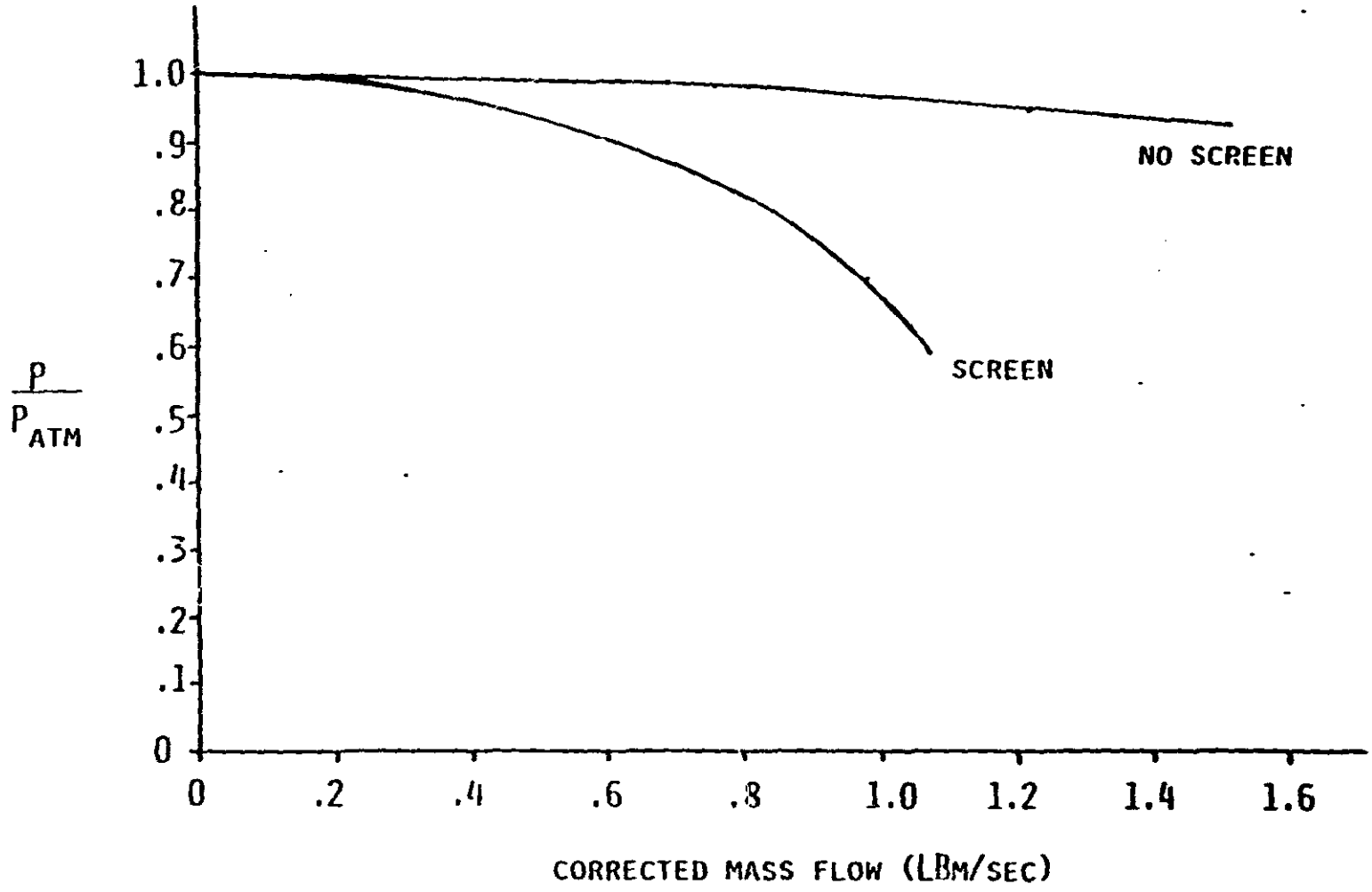

Fig. 3.3.1 Results of Steam Ejector Tests (mass flow rate corrected to 14.696 psi and 545°R)

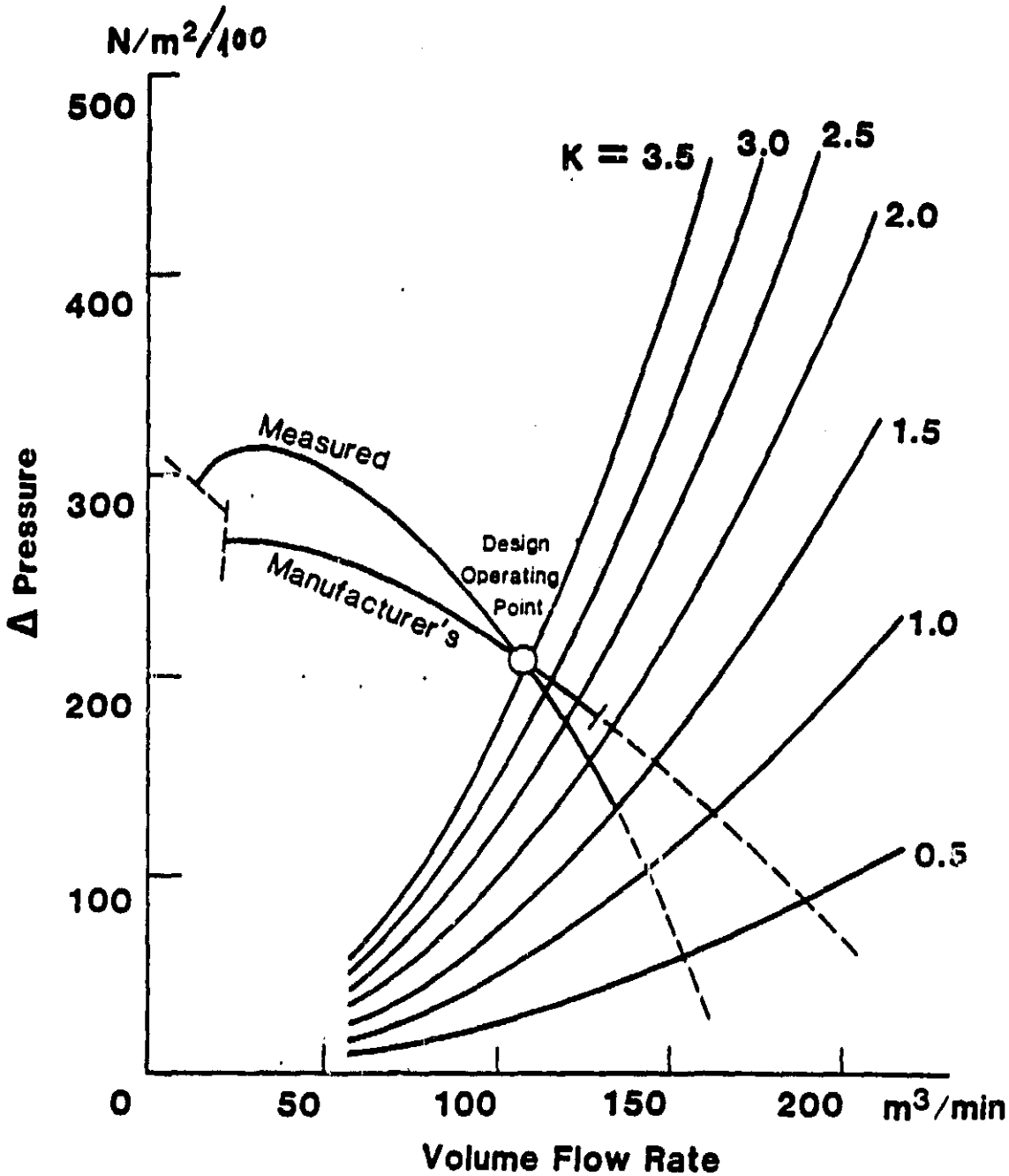

Fig. 3.3.2 Calibrated Characteristic Curve of Auxiliary Blower. Here K = ΔP (Dynamic Head), and ΔP is the pressure drop across the control damper.

Using the values

$\psi = 1.51$, $T_0 = 293°K$, $n = 0.7$ (assumed)

$\gamma = 1.4$, $c_p = 1004$ J/Kg K (for air)

we calculate a turbine running speed U = 83.2 m/s

We can also define the load coefficient in terms of the absolute flow angles at mean radius

$$\psi = \frac{u_x}{U} (\tan \alpha_2 + \tan \alpha_3) \qquad (3.3.2)$$

With $\alpha_3 \sim 0°$, $\alpha_2 = 70°$

$$u_x = \frac{\psi U}{\tan \alpha_2 + \tan \alpha_3} = \frac{1.51 \times 83.2}{\tan 70°} = 45.7 \text{ m/s}$$

If we keep the hub/tip ratio the same as in the HPTP, then

$$\frac{\text{blade height}}{\text{mean radius}} = 0.167 = H/R$$

which leads to a mass flow rate

$$\dot{m} = 2\pi R^2 \times 0.167 \times \rho u_x \qquad (3.3.3)$$

Using $\dot{m}/\rho = 100/60$ m^3/sec, the mean radius H is found to be R = 0.186 m. The corresponding blade height is H = 0.0311. This blade size is about 1.5 times larger than the blades used in the space shuttle engine.

The resulting rotation speed is $\Omega = U/R = 83.2/0.185 = 447$ rad/s = 4272 rpm and the Reynolds number based on chord and relative leaving velocity is

$$\text{Rey} = \frac{\rho u_x/\cos \beta_3 \, c}{\mu} = \frac{1.2 \times 46/\cos 60° \times 0.031}{2 \times 10^{-5}} = 1.7 \times 10^5$$

In view of these results, there are several objections to the use of the blower. First of all, the pressure it delivers is not high enough to provide for the test turbine to operate at the design condition (π_t = 1.19) and at the same time overcome the frictional loss in the duct and

provide a margin for testing at π_t above design. The more serious fault is the low Reynolds number of less than 2×10^5. As discussed in Sec. 3.1, this is in the middle of the transition range, particularly given the high load on the blades.

Several options exist for increasing the Reynolds number. Among these, we list the following:

1. Pressurizing the test section and making the test facility part of a closed loop.

2. Using the large De Laval air supply system.

3. A closed loop test facility using a gas other than air.

Option (1) entails most of the same sealing problems as option (3), while adding the operational and construction difficulties of a high pressure system. It therefore was discarded early.

The De Laval compressor is capable of delivering sufficient pressure ratio and mass flow, as shown in Fig. 3.3.3. However, in order to achieve a sufficiently high Reynolds number, the test turbine size has to be increased considerably. This also increases the brake power and the size of all other components by large amounts. As a rough calculation let us assume the design Reynolds number based on the blade height is 3×10^5. Then, from Eq. (3.3.1), using

$$\eta = 0.7 \qquad \psi = 1.5 \qquad \pi_t = 1.20$$

we obtain

$$U = 83.4 \text{ m/s}$$

$$u_x = U\psi/(\tan \alpha_2 + \tan \alpha_3) = 45.6 \text{ m/sec}$$

$$H = \frac{R_e \mu}{u_x \rho} = \frac{3\times10^5 \times 1.5\times10^{-5}}{45.6 \times 1.3} = 0.075 \text{ m}$$

$$H/Rm = 0.168$$

$$\dot{m} = u_x \rho \cdot 2\pi RH = 12.46 \text{ kg/s}$$

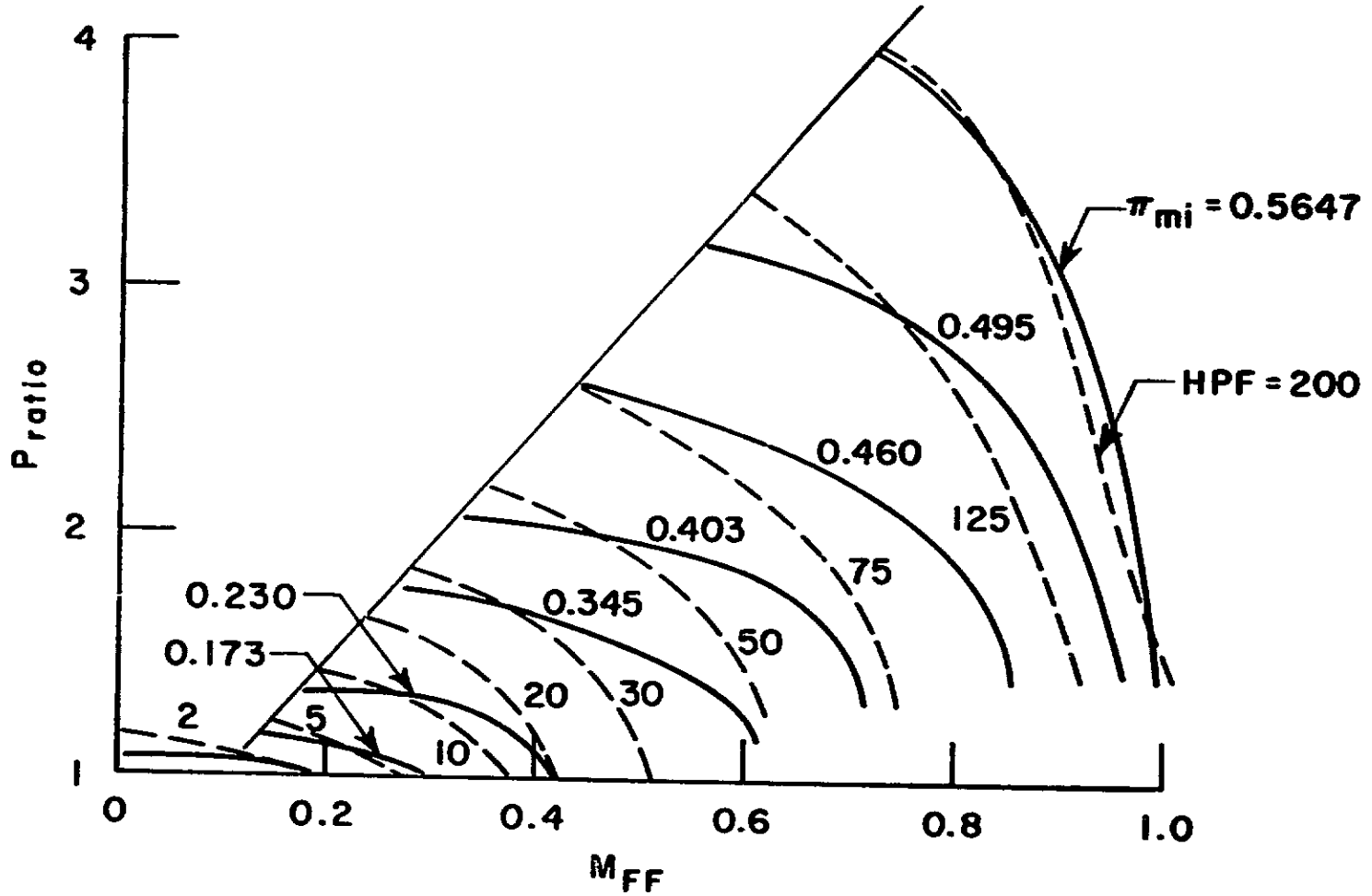

Fig. 3.3.3 Characteristics of De Laval Compressor

At T_{01} = 80°F , p_{01} = 14.7 psia,

$\dot{m}$(Kg/sec) = 107 x MFF

Power (KW) = 8.9 x HPF

Max. Power (KW) = 1560 x π_{m_i}

This is within the capabilities of the compressor (Fig. 3.3.3), although it may require a fairly large amount of bypass to avoid stall. The power to be taken out by the brake is then

$$P = \psi \dot{m} U^2 = 130 \text{ KW}$$

At the above power level the brake can be relatively expensive and large in size.

The present system of which the De Laval compressor is a part, is an old closed loop supersonic tunnel designed to operate at low pressure ($\sim$ 7 psi). In order to operate near atmospheric conditions (to keep the Reynolds number up with reasonable turbine size), we would have to open the 18" circuit piping, install a flange and valve, and build approximately 80 ft. of new 18" line to the test section. All these are fairly expensive operations. One additional important concern is the fact that the system is some 10 years old and has been inoperative for a number of years, and although it is in working condition now, any breakdown during the test program would be very expensive and time-consuming.

The conclusion of the above discussion is that an airflow facility will not provide a convenient test bed for our purposes. In the next section we examine the option of using a different fluid.

3.4 Freon Closed Loop Design

The gas to be used in the closed loop design must be of high molecular weight and low viscosity. After some consideration it was decided that Freon 12 would be the best choice. Freon 12 is a relatively inert gas at room temperature and it is readily available at low cost. Some of its most important constants are listed below.

molecular weight = 120.91

normal boiling point = - 29.79°C

density at STP = 5.35 kg/m^3

viscosity = 1.25×10^{-5} Kg/m/sec

Notice that while its density is about four times that of air, its viscosity is lower by about 30% than that of air.

With these properties we proceed to evaluate the corresponding test turbine design. Again we choose the load coefficient and degree of reaction the same as in the SSME HPFTP turbine. From Eq. 3.3.1, and using the values

c_p = 642 J/Kg K

T_{t1} = 293° K

ψ = 1.51

π_t = 1.192

r = 0.7 (assumed)

γ = 1.12

We obtain

U = 40.3 m/s

and then, using Eq. 3.3.2, with $\alpha_3 = 0$, $\alpha_2 = 70°$,

$u_x = \psi U/(\tan \alpha_2 + \tan \alpha_3) = 22.2$ m/s

If the size of the test turbine is the same as in the SSME, i.e.,

H = 2.169 cm

r_m = 12.9 cm

then the Reynolds number at the design condition is

$$Rey = \frac{\rho u_x H/\cos 60°}{\mu} = 3.9 \times 10^5$$

and also

$$\Omega = 312 \text{ rad/s} = 2980 \text{ rpm}$$

$$\dot{m} = 2\pi r_m H \rho u_x = 1.95 \text{ kg/s}$$

$$\text{power} = \dot{m}\, \eta_t\, c_p\, T_1 (1 - \pi_t^{-(\gamma-1)/\gamma})$$

$$= 4.79 \text{ KW}$$

A newly designed airtight gas booster will be used to supply power. Assuming it delivers a pressure ratio of 1.35 at the mass flow of 1.95 kg/s and has an efficiency of 0.6, the required power at the design point is

$$\text{Power} = \frac{\dot{m}\, c_p T_0}{\eta_c} (\pi_c^{\gamma-1/\gamma} - 1) = 20 \text{ KW}$$

Although the Reynolds number of the test turbine is well below SSME turbines operating Reynold numbers (around 5×10^6), it is well above the loss transition zone, and it does therefore allow some opportunity to explore Reynolds number effects in the turbulent regime. If we wanted to increase the Reynolds number to $\sim 10^6$, the test section size would have to be more than doubled. This would increase the power input by a factor of 5 and would make the whole facility more difficult to build and operate. As far as instrumentation is concerned, the difficulty of using a two centimeter blade is not very different from that with a four centimeter blade. Therefore, we decide to retain the SSME turbine size. This will also facilitate fabrication of test blades, by using sample SSME blades as casting blanks.

In summary, there are significant advantages in going from open-loop air to a closed loop Freon facility. The Reynolds number is increased and at the same time we reduce the power taken by the turbine, hence reducing the size of the brake, the compressor, and all other components. One further interesting point is that we can vary the Reynolds number for the same test turbine by mixing Freon and air, or perhaps other gases.

3.5 Loop Components Design

3.5.1 Loop Description

A schematic diagram of the proposed closed loop design is shown in Fig. 3.5.1. A heat exchanger is placed before the bypass to remove the net heat added to the gas due to the inefficiency of the turbine and compressor. Two dampers, one in the bypass loop and one in the main loop are used to control the pressure and main flow through the turbine. A flow straightener is placed about one or two diameters before the test section to reduce the flow irregularity due to the turns, damper and heat exchanger. This introduces some pressure loss, which can be easily compensated for by slightly increasing the pump capacity.

An electrical brake is connected to the turbine shaft through a belt system. Two universal joints are used to eliminate the lateral force transmitted to the force measuring devices.

An estimation of the pressure losses in the main loop is given in Sec. 3.5.2. The main pressure drop appears to be in the heat exchanger. The total pressure drop with full open damper is only about 0.03 atm, due to the assumed use of 0.305m (12") ducting (0.355m (14") in the heat exchanger and test section approach). Thus, a gas booster designed for a ΔP of 0.33 atm at a mean P = 1 atm, should allow ample margin beyond the nominal turbine pressure ratio of 1.192.

The cooler will be made from standard finned tube of large surface area, and heat will be taken out by cooling water. The brake will basically be an electrical DC generator (from a surplus aircraft motor-generator set). It has some control over the stator current and can run over a wide range of speed. Two generators driven in parallel may be needed, because of some uncertainty about the precise characteristics of the intended generator.

3.5.2 Pressure Drop Estimation

Heat Exchanger. The following values pertain to the Freon 12 flow:

Mass Flow Rate ($\dot{m}$)	=	2.3 kg/s
Density (ρ)	=	5.5 kg/m^3
Viscosity (μ)	=	1.25×10^{-5} kg/ms
Specific Heat (c_p)	=	640 J/kg deg
Thermal conductivity (k)	=	1.12×10^{-2} w/m deg
Prandtl number (Pr)	=	0.714

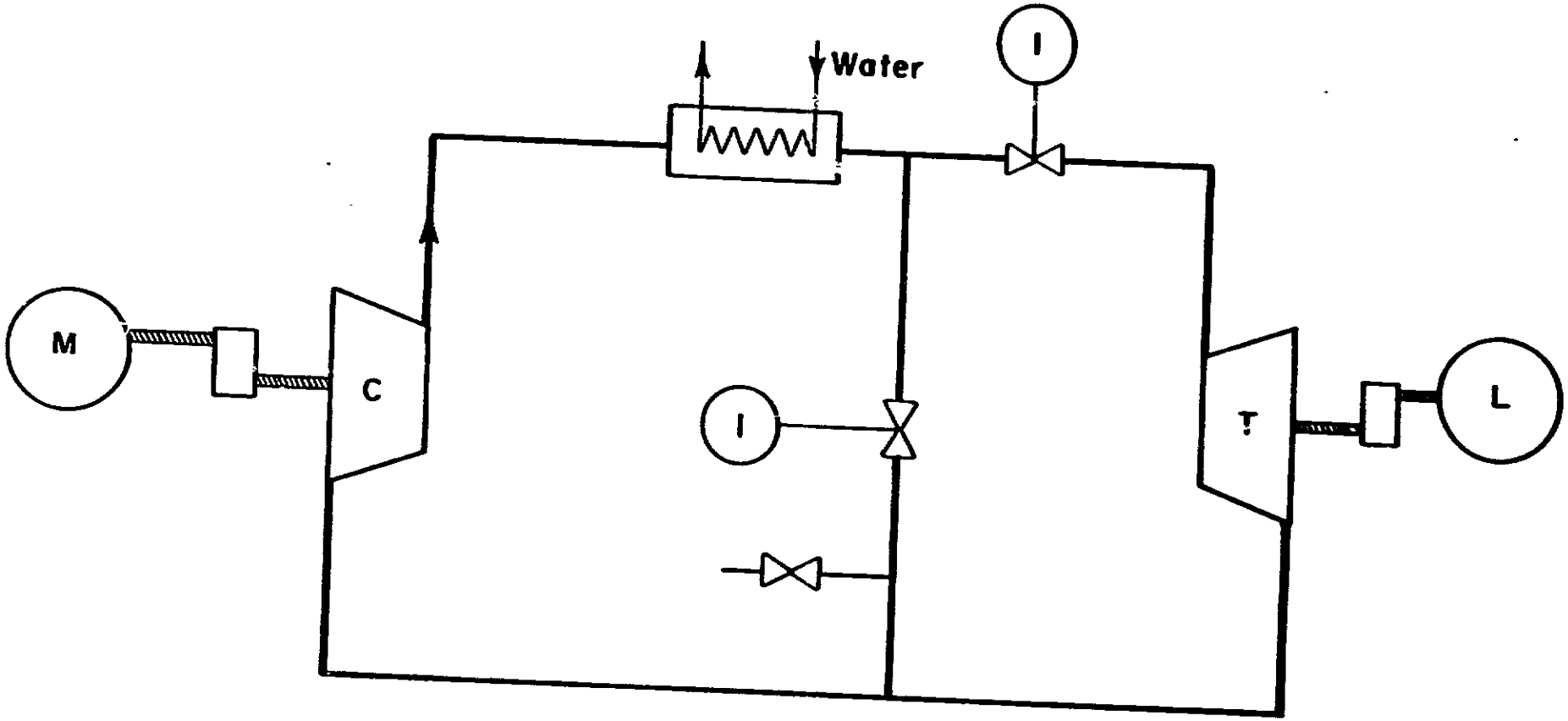

Fig. 3.5.1 General arrangement of the Freon closed loop:

(I) Valve

(M) Motor

(C) Gas Booster (compressor)

(L) Brake (load)

(T) Test Turbine

Assume the duct diameter is 0.356 m (14") at the heat exchanger, and that the flow area A_f is one half the total frontal area (Ref. 29). Then

$$u_x = \frac{\dot{m}}{\rho A_f} = 8 \text{ m/sec}$$

and the Reynolds number based on hydraulic diameter is 1.38×10^4.

From Ref. 29, adopting a design similar to that designated CF - 8.72 (finned circular tubes), we obtain a pressure loss factor f = 0.03, plus a specific area $\alpha = 535 \text{ m}^2/\text{m}^3$ and a heat transfer parameter

$$\frac{h}{Gc_p} (Pr)^{2/3} = 0.004$$

from which

$$h = 141.00 \frac{W}{m^2 K}$$

Assume a thermal power of 15 KW is to be removed (a conservative estimate). This corresponds to a temperature drop for the gas of $\Delta T_G = 15000/2.3/640 = 10.2$ K. If we now impose an equal temperature rise for the cooling water, and a (constant) temperature difference of 8K between both, the required effective area is

$$A = \frac{15000}{h\Delta T} = 13.3 \text{ m}^2$$

Total heat exchanger volume: $= A/\alpha = 0.025 \text{ m}^3$

$$\text{Axial length} = \frac{V}{\pi D^2/4} = 0.25 \text{ m}$$

The pressure drop can be estimated by

$$\Delta p = \frac{f}{2\rho} \left(\frac{\dot{m}}{A_f}\right)^2 \frac{A}{A_f} = 1560 \text{ N/m}^2$$

The water flow rate would be $\dot{m}_w = 15000/(4180 \times 10.2) =$ 0.35 Kg/sec, or about 5.5 GPM.

Ducting Loss

For 0.305m (12") ducting, the flow velocity is u_x = 5.5 m/s and using f = 0.03 and K = 0.9 for duct bends (fraction of dynamic head lost per bend), with 20 m of ducting and 8 bends (to account for the need to mount the compressor at a level different than that for the test section), we obtain

$$\Delta p = 2f \frac{L}{D} \rho u_x^2 + K \times (\text{No. of bends}) \times \frac{1}{2} \rho u_x^2$$

$$= 561 + 599 = 1160 \text{ N/m}^2$$

Dampers

In the fully open position, the damper will have a negligible pressure drop. For partially closed positions, the Δp is a control variable.

Flow Straightener

It is estimated that the flow straightener will take a pressure drop of 500 N/m^2. This is for an L/D of 50, and is low due to the low dynamic head involved.

Sudden Enlargement at the Test Section Exit

For a 22 m/sec flow speed in the test section, almost one full dynamic head will be lost at the discharge into the downstream duct. This amounts to 570 N/m^2.

Total

Hence the total pressure drop in the loop is approximately

Δp = 3800 N/m^2

This small value of the loop pressure drop is due to the large diameter ducting assumed (we have a number of 0.35m (14") sections available, and 0.305m (12") is a standard size). In connection with the estimated pressure drops it should be noted that closed loop recuperated Brayton cycles have been built with similar relative pressure losses (~3%).

3.6 Off Design Operation Control

Ideally, one tends to operate turbines very near their design point, but it is unavoidable that sometimes they will run at some point other than optimum. It is also known that for the Space Shuttle HPOTP the most serious subsynchronous vibration occurs at a power level of 9% above design point. Therefore subsynchronous vibration excitation at off-design conditions is a problem of interest.

There are several ways to operate the turbine at off-design conditions. Either the damper in the main loop can be adjusted to provide a different pressure ratio across the turbine, or the shaft load can be varied by changing the external power dissipation. For the latter case, brake load power output is in the form of electrical power dissipation in some heating resistance. It is estimated (see Section 3.4) that the maximum power the turbine can produce is about 6 KW, and this can be absorbed in a relatively simple water-cooled resistance.

To avoid compressor stall and increase the test range, a bypass is included in the loop. This also gives some additional flexibility in controlling parameters for the test program. For example, since it is a closed loop, we can mix air (or some other gas) with Freon 12 to get different operating Reynolds' numbers. By adjusting the bypass damper, we can still keep turbine operation at the design point.

The following is a description of the simplified model used to assess the off-design operation of the loop.

The turbine efficiency, and stator and rotor leaving angles (α_2, β_3) are assumed constant in the relatively small range of operating parameters about the design point. The following two equivalent expressions can then be written for the power per unit flow rate:

$$W = \eta_t \, c_p \, T_{01} \left[1 - \left(\frac{p_{02}}{p_{01}}\right)^{\frac{\gamma-1}{\gamma}}\right] = u_x \, U\left(\tan \alpha_2 + \tan \beta_3 - \frac{U}{u_x}\right) \qquad (3.6.1)$$

The turbine power will be absorbed by a resistively loaded, separately excited DC generator. Its output voltage will be

$$V = K_G \, \Omega \, i_{ex} - I R_i = I \, R_L \qquad (3.6.2)$$

where K_G is a machine constant (reflecting also any interposed speed changes), i_{ex} is the excitation current, I is the load current and R_i, R_L are the internal and load resistances, respectively. Also

$$\Omega = \frac{U}{r_m} \tag{3.6.3}$$

where r_m is the turbine mean radius and U its blade speed.

The generator absorbs a shaft power

$$P_g = V\, I/\eta_g \tag{3.6.4}$$

where η_g is its mechanical efficiency. From (3.6.2) then,

$$P_g = \frac{K_G^2\, i_{ex}^2}{r_g} \; \frac{R_L}{(R_L + R_i)^2} \; \left(\frac{U}{r_m}\right)^2 \tag{3.6.5}$$

and this must be the same as $W\,\dot{m} = W(\rho_1 u_x A)$, where ρ_1 is the inlet gas density and A the annulus area.

The generator parameters can be grouped together into a single "load control" parameter

$$\lambda_g = \frac{K_G^2}{r_g} \; \frac{R_L\, i_{ex}^2}{(R_L + R_i)^2} \tag{3.6.6}$$

in terms of which,

$$W = \frac{\lambda_g}{\rho_1 A r_m^2} \; \frac{U^2}{u_x} \tag{3.6.7}$$

In addition to this power balance, a pressure balance around the loop is needed. We assume a constant-speed compressor with a pressure rise characteristic given by

$$\Delta P_c = \Delta P_{co} - K_c u_x^2 \tag{3.6.8}$$

which reflects the approximately quadratic droop of ΔP_c with mass flow rate. Similarly, the passive elements (bends, cooler, flow straightener, tubing) contribute pressure losses

$$-\Delta P_{loss} = K_L u_x^2 \qquad (3.6.9)$$

and the control valve contributes

$$-\Delta P_{valve} = K_v u_x^2 \qquad (3.6.10a)$$

This leaves for the turbine a pressure drop

$$\Delta P_t = \Delta P_{co} - (K_c + K_L + K_v) u_x^2 \equiv \Delta P_{co} - K_{tot} u_x^2 \qquad (3.6.10b)$$

If the mean loop presure is $\bar{p}$, then the turbine pressure ratio is

$$\frac{P_{02}}{P_{01}} = \frac{\bar{P} - \Delta P_t/2}{\bar{P} + \Delta P_t/2} = \frac{2\bar{P} - \Delta P_{co} + K_{tot} u_x^2}{2\bar{P} + \Delta P_{co} - K_{tot} u_x^2} \qquad (3.6.11)$$

Upon substitution into Eq. (3.6.1) we obtain two different expressions for W in terms of u_x, U. Together with Eq. 3.6.7, we have therefore a system of equations to be solved for W, u_x, U once the valve setting (K_v) and the load parameters (λ_c) are specified.

Many of the parameters of this model can only be numerically specified after the particular components of the loop are precisely characterized. However, for the purpose of illuminating the operating characteristics of the loop, we can use some reasonable component parameters, plus an assumed operating point, and deduce the necessary values.

For the compressor, assuming its nominal operating pressure ratio is 1.35 at a flow rate of 2.2 Kg/sec (giving u_x = 25.3 m/sec), and that the flow rate for zero pressure rise is twice the nominal value, we obtain ΔP_{co} = 0.467 atm = 47300 Pa. and K_c = 18.5 Kg/m^3.

We also assume here a nominal turbine pressure ratio of 1.24 and a mean loop pressure $\bar{p}$ = 1 atm. Therefore, the total pressure drop coefficient K_{tot}, as implied by Eq. (3.6.11), must be 40 Kg/m^3. This is an implicit determination of the nominal value setting, the precise value of which could be determined from $K_v = K_{tot} - K_c - K_L$ if the parasitic loss factor K_L were prescribed. Also, at a turbine pressure ratio of 1.24 and at T_{01} = 298 K, $(c_p)_{freon}$ = 647J/Kg K, γ = 1.12, η_t = 0.7, we calculate from the first part of Eq. 3.6.1 a work per unit mass of

$$W_{nominal} = 3074 \text{ J/Kg}$$

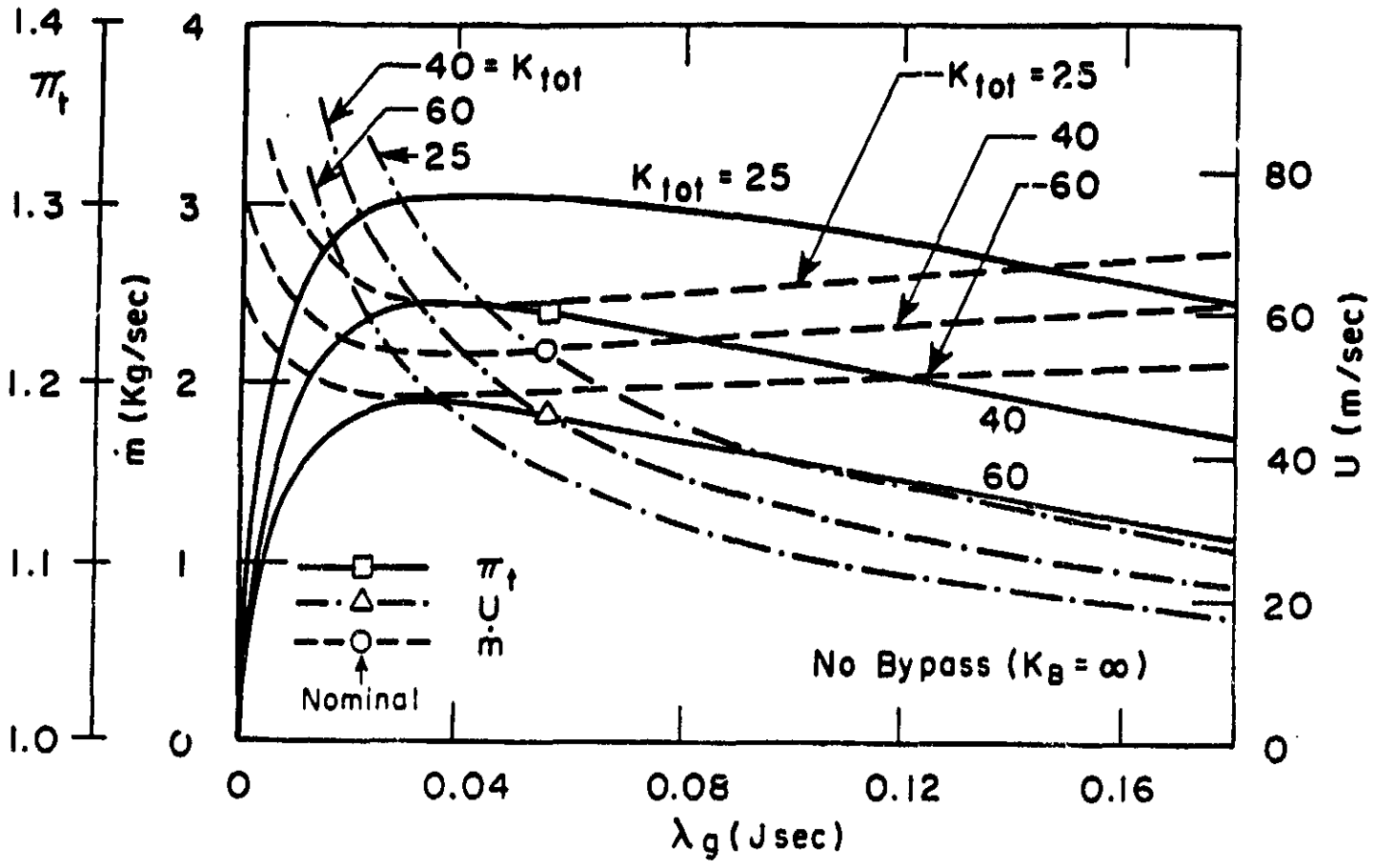

Fig. 3.6.1 Effect of generator control parameter (λ_g) and main damper setting (K_{tot}) on turbine pressure ratio (π_t), wheel speed (U) and flow rate ($\dot{m}$).

and then, from the second part of 3.6.1 (using $\alpha_2 = 70°$, $\beta_3 = 60°$, $u_x = 25.3$ m/sec), the nominal wheel speed is

$$U_{nom.} = 45.0 \text{ m/sec}$$

There is also a second root for this variable, giving U = 68.2 m/sec. As we will see later, this corresponds to a second possible operating branch, but we assume the nominal point to be in the low speed branch.

With these values, plus $\rho_i = 4.94$ Kg/m^3, $A = 2\pi r_m h = 0.0176$ m^2 and $r_m = 0.129$ m, the nominal generator parameter is then found from Eq. 3.6.7, giving

$$(\lambda_g)_{nom.} = 0.0556 \text{ J x sec}$$

For off-nominal conditions at the same T01, the system of equations to be solved is

$$W = 4.48\, U u_x - U^2 = 135000 \left[1 - \left(\frac{155300 + K_{tot} u_x^2}{249900 - K_{tot} u_x^2}\right)^{0.107}\right] = 691\, \lambda_g \frac{U^2}{u_x} \qquad (3.6.12)$$

The results are shown in Fig. 3.6.1 for a range of generator and valve settings. As the load factor λ_g is increased (either by increasing excitation current i_{ex} or by moving the load resistance R_L towards R_i from either side), the turbine speed U is seen to decrease continuously. A wide range of turbine speeds appears to be achievable using a combination of generator and damper control. For example, if the excitation current is varied by a factor of 1.414 above and below nominal, this changes λ_g by a factor of 2, and allows U to change between about 30 and 62 m/sec. Similarly, by adjusting the valve opening such that K_{tot} varies between 25 and 60 Kg/m^3 (at fixed load) U can be varied between 37 and 55 m/sec.

On the other hand, as Fig. 3.6.1 shows, load variations tend to have only a minor effect on mass flow rate and pressure ratio. In fact, an interesting aspect of this calculation is that $\dot{m}$ and $\pi_t = p_{01}/p_{02}$ both have an extremum (minimum for $\dot{m}$, maximum for π_t) in the probable control range. Thus, for example, for a valve setting of $K_{tot} = 40$ Kg/m^3, the two generator settings $\lambda_g = 0.012$ J sec and $\lambda_g = 0.127$ both give the same external turbine parameters; i.e., $\dot{m} = 2.41$ Kg/sec, $\pi_t = 1.2$. Of course, the <u>internal</u> parameters, such as velocities and flow angles are quite different, since U = 91 m/sec at the first of these settings, while U = 28 m/sec at the second. Therefore we can explore a large range of turbine aerodynamic conditions by load variations, with only minor changes in compressor power, flow rate or other factors. These other parameters are then most easily controlled by valve adjustments (for in-

stance, at the nominal generator setting, $\dot{m}$ varies from 1.95 to 2.47 Kg/sec and π_t from 1.18 to 1.31 by K_{tot} changes between 25 and 60 Kg/m^3).

Further variations of $\dot{m}$ can be obtained by opening the bypass valve. For a fixed $\dot{m}$ there are various combinations of main and bypass valves giving the same π_t; the value of the bypass is that it allows lower turbine flow rates with no danger of compressor stall. The calculation can be modified easily to account for bypass. Assuming the bypass line is immediately across the compressor, its pressure drop is ΔP_c, and its flow rate is $\dot{m}_B = \dot{m}_c - \dot{m}_t$ where $\dot{m}_c$ and $\dot{m}_t$ refer to compressor and turbine, respectively. Then, if K_B is a pressure loss factor for the bypass valve,

$$\Delta P_c = K_B' \dot{m}_B^2 = K_B u_B^2 \tag{3.6.13}$$

where u_B is a fictitious bypass velocity defined as $u_B = \dot{m}_B(u_x/\dot{m}_t)$. Eq. (3.6.13), together with the compressor characteristic (Eq. 3.6.8) and the (line + main valve) loss equation

$$\Delta P_c - \Delta P_t = (K_v + K_L) u_x^2 \tag{3.6.14}$$

can be solved for u_B, giving

$$u_B = -\frac{K_c u_x}{K_B + K_c} + \sqrt{\left(\frac{K_c u_x}{K_B + K_c}\right)^2 - \frac{\Delta P_{co} - K_c u_x^2}{K_B + K_c}} \tag{3.6.15}$$

and then

$$\Delta P_t = K_B u_B^2 - (K_{tot} - K_c) u_x^2 \tag{3.6.16}$$

where we have reintroduced $K_{tot} = K_c + K_v + K_L$ as a measure of the main valve position. The turbine pressure ratio is then

$$\pi_t = \frac{2P + \Delta P_t}{2P - \Delta P_t} \tag{3.6.17}$$

and this factor replaces that in parentheses in Eq. 3.6.12. Fig. 3.6.2 shows the calculated results for the nominal generator setting (λ_g = 0.0556).

Finally, it is of interest to examine the stability of the loop operation. For this purpose we select the nominal settings only (K_{tot} = 40, λ_g = 0.0556), but qualitatively similar results can be obtained for all other settings. The procedure will consist of plotting the torque-speed curves of turbine and generator and examining the nature of the equilibrium point (point of intersection).

For the generator, we have, from Eqs. 3.6.5 and 3.6.6, $P_g = \lambda_g \Omega^2$, i.e., for the torque Q_g.

$$Q_g = \lambda_g \Omega = 0.639\ U \qquad (3.6.18)$$

For the turbine, we read on Fig. 3.6.1 the value of $\dot{m}$ corresponding to a particular U (for the nominal K_{tot}). We then calculate $u_x = \dot{m}/\rho A = \dot{m}/0.087$ and $W = U(4.48u_x - U)$ and, finally,

$$Q_t = \frac{W\,\dot{m}}{\Omega} \qquad (\Omega = U/0.129) \qquad (3.6.19)$$

The results are plotted in Fig. 3.6.3. It is clear that the equilibrium point, at U = 45 m/sec, Q = 19.5 Nm is a <u>stable</u> operating point, since an increase in spin rate would entail a drop in turbine torque and an increase in absorbed (generator) torque, leading to a slowdown back to equilibrium.

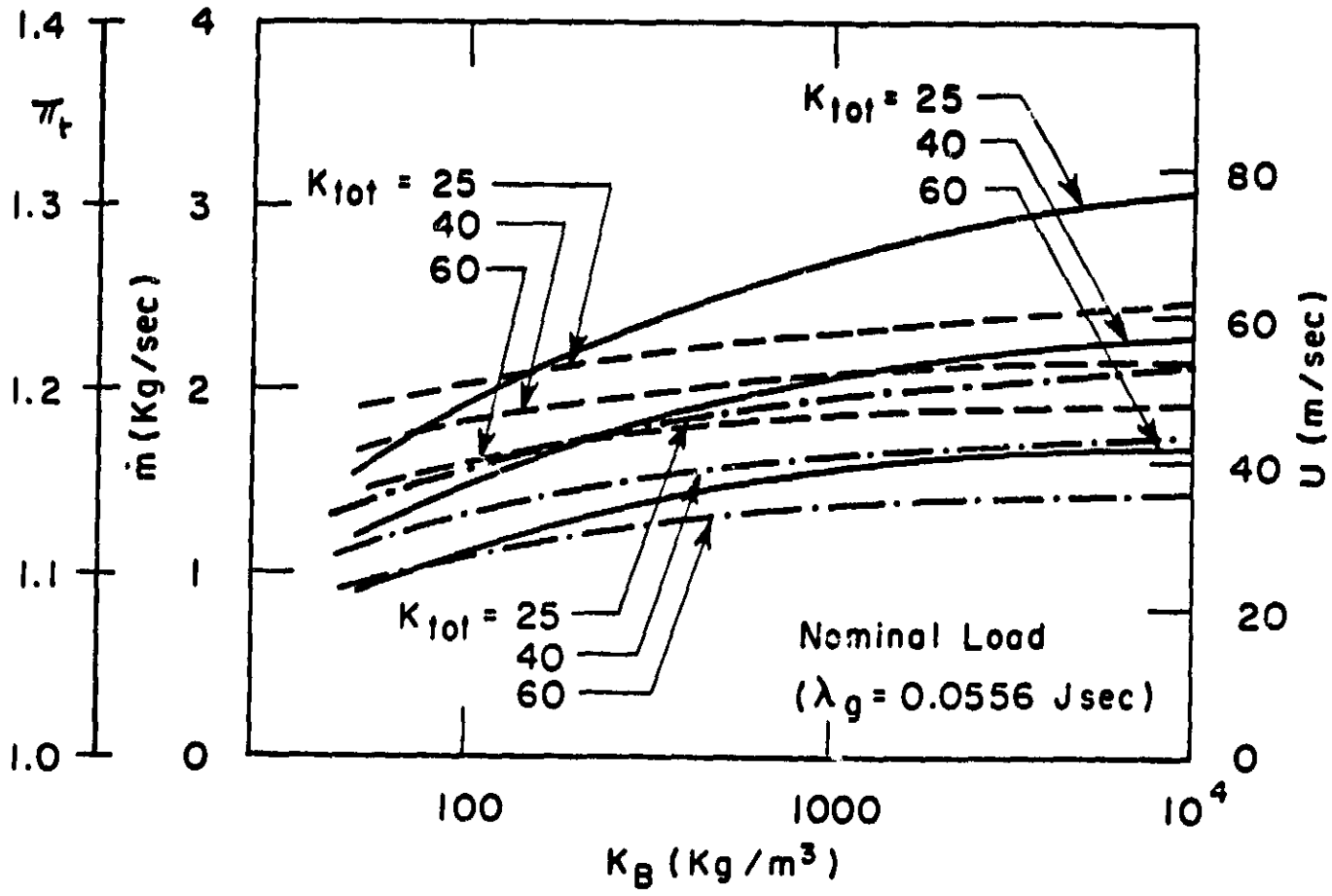

Fig. 3.6.2 Effects of bypass at nominal load.

Line identification as in Fig. 3.6.1.

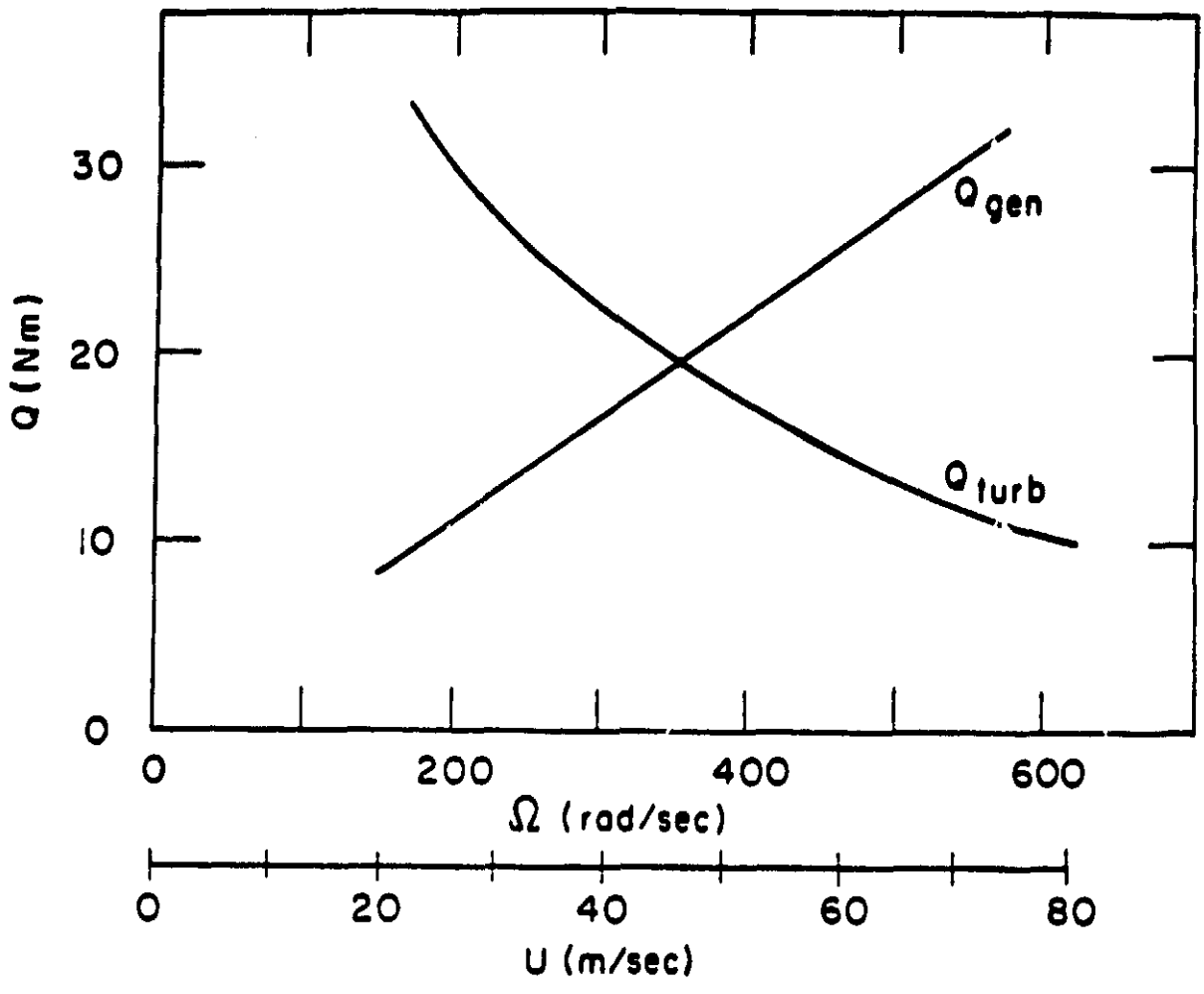

Fig. 3.6.3 Torque-speed curves for turbine and brake (at nominal conditions).

3.7 Test Section Design

3.7.1 Test Section Concept

Since the test section is clearly at the heart of the experimental facility, we recapitulate briefly here the objectives of the tests as a way to obtain guidelines for the design. We wish to obtain measurements of the transverse forces arising due to small transverse displacements of the rotor with respect to its case, and we wish to do so for a reasonable variety of blade-tip configurations, including shrouded vs. non-shrouded, various levels of mean clearance, various tip sealing arrangements, and various axial stator-rotor gaps. In addition, we want to allow access for a number of probes for detailed study of the flow patterns in some cases. These objectives prompt the following guidelines:

(a) The rotor should be mounted on bearings which are laterally restrained only by stiff force sensors.

(b) Axial displacement of the rotor and rotation about transverse axes should be restrained by separate means which do not contribute force components in the transverse direction.

(c) The turbine casing should have the capability for precise lateral displacements, without interfering with the fixed bearing supports.

(d) Since such a displacement is bound to induce fluid forces on other parts of the rotor, especially the stator seals, a provision must exist to either eliminate or separately measure such forces.

(e) The design of the test section should allow modular replacement of segments with as little complication as possible, in order to facilitate extensive parametric testing.

(f) Access for pressure, velocity, temperature and other sensors should be as direct as possible.

These considerations have led to a conceptual test section arrangement, which is shown in Fig. 3.7.1 and which, in general, is similar to that employed by Urlichs (Ref. 7) in his open-loop tests with air. The turbine shaft is simply supported on two roller element bearings which are themselves supported by four transverse bars each. These bars are part of a support frame which is connected to the load cells and which will be discussed more fully in Sec. 3.8. The casing is split in two, one part for the stator and the other for the rotor; each of these is mounted on a carriage for transverse displacement, and both can collectively move axially by means of an additional carriage. In this manner the horizontal off-centering of each, the

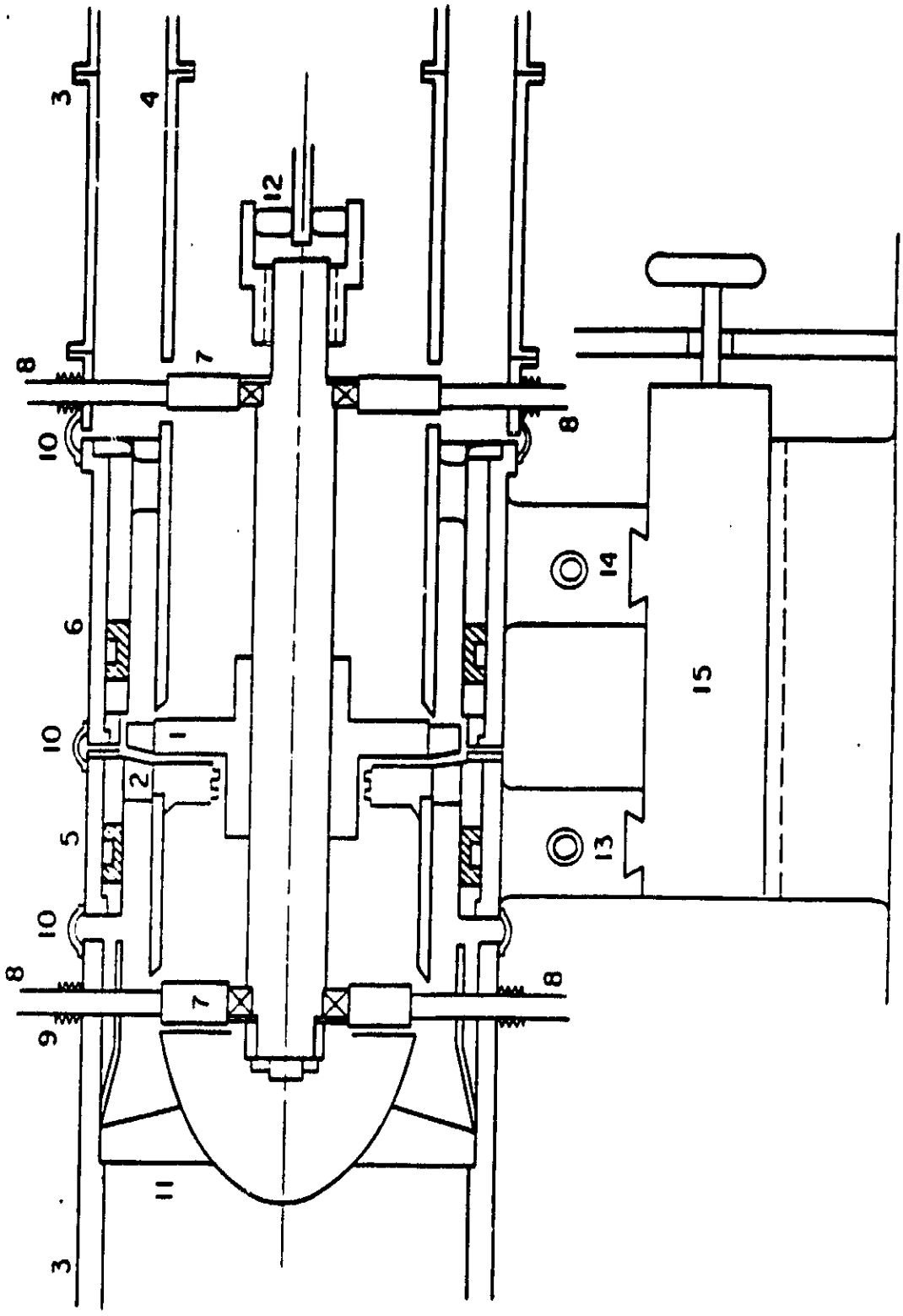

Fig. 3.7.1 Schematic of test section. (1) Turbine wheel. (2) Stator nozzles. (3) Outer ducting. (4) Inner ducting (brake housing). (5) Movable stator casing. (6) Movable rotor casing. (7) Bearings. (8) Bearing support frame. (9) Bellows seal. (10) Flexible sealing joint. (11) Inlet guide vanes. (12) Flexible connector to brake shaft. (13) Carriage for stator casing transverse motion. (14) Carriage for turbine casing transverse motion. (15) Carriage for casing axial motion.

stator and the rotor, plus the axial gap between them, can be separately controlled. Since the test section is part of a closed loop, tight sealing of the working gas is required. This requires the use of flexible rubber or metal bellows seals at the joints between movable casing sections and at the points where the support bars go through the fixed casing. These last seals may introduce small unbalanced forces on the support system, but with some care these should be only minor and can in any case be calibrated against. Although the transverse bearing support rods will introduce some disturbance to the inlet flow. We will ensure that these are small by reducing the rod cross-sections and by fairing them.

Additional construction details on the test section are discussed in the remainder of Section 3.7.

3.7.2 Choice of Stator Sealing Geometry

Since our primary concern is with rotor tip effects rather than with stator effects, we will in our design attempt to isolate any side forces arising from the required stator seal when the casing is offset. Figs. 3.7.2(a) and (b) represent two possible approaches to this end.

In the design of Fig. 3.7.2(a) the seal-off centering forces are minimized by leaving a wide gap at the rim, with no sealing strips, and placing the sealing strips on the upstream and downstream surfaces. The drawback of this arrangement is that it makes it difficult to effect variations of the stator-rotor axial gap, a parameter shown to be important by the work in Ref. 7.

In the design of Fig. 3.7.2(b) the sealing is done on the stator rim, thus allowing unimpeded axial displacements of the casing. If the radial sealing is done with a labyrinth, seal side forces will then arise when the casing is displaced laterally. An alternative possibility is to use a floating ring or floating brushing radial seal, in which case a certain amount of radial displacement can be accommodated by the floating stator element with no change in clearance, and hence with no generation of side forces (or at least with reduced forces). Most interest in our testing attaches to the rotor-generated side forces, with a secondary interest on the forces due to the stator tips on seals. Thus, two approaches appear most indicated for our purposes: (a) Use floating-element radial seals to mimimize stator forces, and (b) Use a radial labyrinth with independent side displacement (as shown in Fig 3.7.2 (b)). In the second case, measurement of the side forces with various combinations of (small) stator and rotor eccentricities will separate their respective contributions. In the first case (floating element seals), a more direct rotor force measurement is is obtained, but no information is gained on stator seal effects.

We propose to employ both types of radial seals: if a satisfactory design of a floating element seal is evolved, with sufficient lateral compliance ($\sim$0.3mm) and low side force, this will be used for the majority of the tests. The force contribution of the stator seals will be measured in special tests with

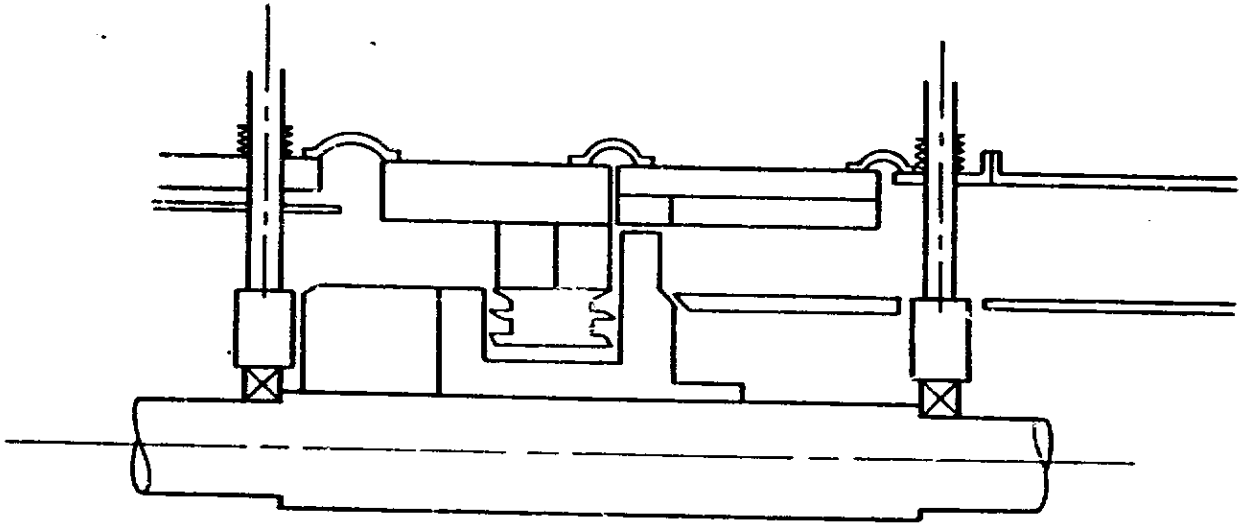

(a) Face Seal

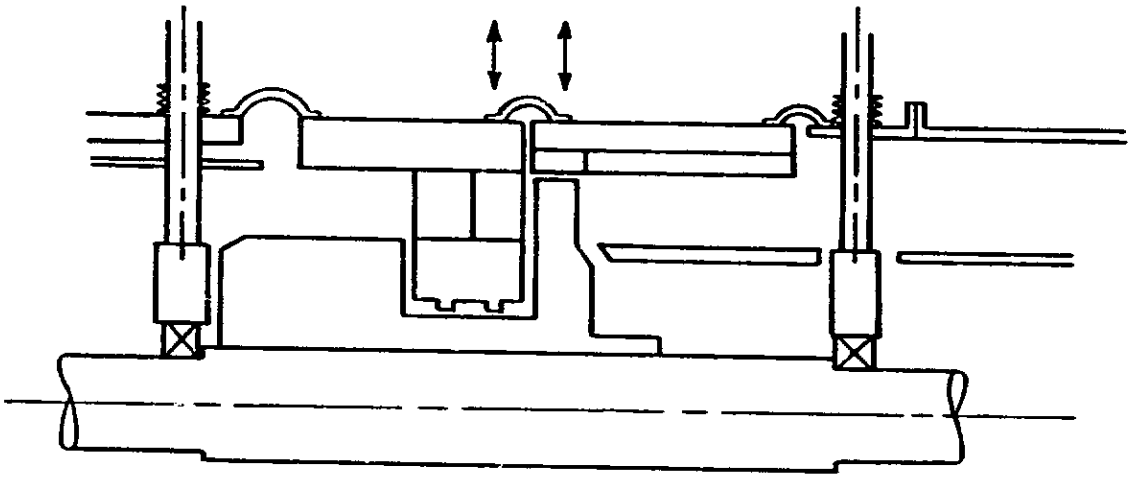

(b) Radial Seal (Labyrinth, Floating Ring, or Floating Bushing)

Fig. 3.7.2 Two approaches to stator sealing.

a radial labyrinth seal, which will also serve as a back-up for the other design. Both types allow free axial clearance adjustment.

3.7.3 General Assembly and Replacement of Modular Parts

The test facility will be called upon to support a variety of configurations, as will be discussed in the section on the test program. Particularly important will be the ability to change the configuration of the turbine tip area. This will be required at a minimum for the preliminary testing of efficiency vs. nominal clearance. In addition, it is necessary for testing of various tip sealing arrangements in shrouded turbines and, possibly, of surface treatments in unshrouded cases. It is then desirable to minimize the amount of work needed to replace that particular section, as well as, more generally, to allow a relatively simple assembly and disassembly of the whole test section, such as will be required when changing rotor blading.

Although full detail on this matter must await final design, it will be useful to discuss here a preliminary conceptual design showing at least the feasibility of such partial or total disassembly. With reference to Fig. 3.7.3 we will assume the test section initially assembled in the configuration shown. We wish to replace the ring labelled (9), which constitutes the rotor tip casing. As a first step, the first section of downstream ducting (1), which is assumed to be built in the form of an axially split cylinder, will be opened and removed (its actual length may be greater than shown in the sketch). The first section (2) of the inner duct is also similarly removed. The flexible coupling (3) between the turbine shaft and the dynamometer can now be slid to the right and the connecting shaft removed. This will leave a section of turbine shaft bare; this can now be supported on an external jack or other suitable base (4) prior to removal of the right-hand bearing supports.

To allow access to the inner rings of the casing, the vertical bars supporting the right-hand bearing must now be removed. Prior to this, the bellows seals such as (5) must be loosened and the bars disconnected at their upper linkage points to the support frame. They can then be slid out of the way. A number of possibilities exist now, including sliding out the rings, such as the bearing outer race (7), as far as the external support would allow, then inserting a second support on the other side and completing the removal. A simpler and more precise technique is to use a number of holes (13) (to be capped in operation) in the turbine disk to insert hardwood pegs between the stator and its rotor land, thus providing support for the shaft and allowing removal of the external support on the downstream side. Detailed stress calculations should be made on the disk, but since the required rotation speed is not high (less than 50 m/sec at the blades) the holes should pose no problem.

Having cleared the right-hand side of the machine, the bearing race (7), the internal downstream lining (8) and, finally, the ring (9), can be simply removed. They can be replaced and re-assembled following the inverse sequence of steps.

If the rotor were to be removed as well, the process would continue by

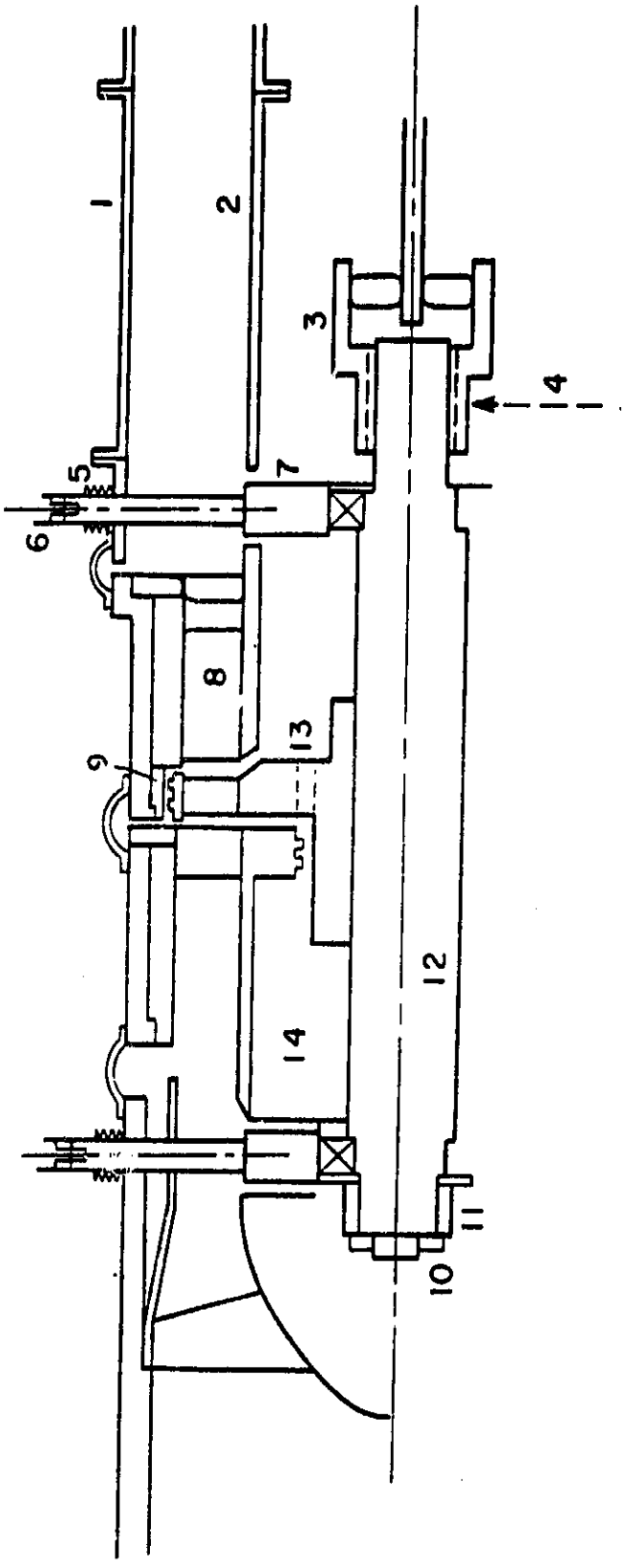

Fig. ? 7.3 Schematic to illustrate disassembly.

unlocking the left bearing retainer at (10), removing the support pegs and sliding the complete shaft assembly to the right.

3.7.4 Rotor Mass and Natural Frequency Estimates

According to Secs. 3.2 - 3.4, our first test turbine will have an outer diameter of 28.2 cm, with blades of 2.2 cm height. The shaft dimensions are less well defined at this point; a distance of 50 cm between bearings, and a shaft diameter of 5 cm (solid) appear adequate for a preliminary layout. The rotor is then as sketched in Fig. 3.7.4.

Assuming steel for the material of construction, those dimensions give an estimated mass of 7.7 Kg for the shaft, 10.4 Kg for the rotor disc, 4 Kg for the stator land, and an estimated 0.7 Kg for the 40 brass blades.

If we lump the disk, stator land and blades together as a central mass, the first natural pinned-pinned frequency of the shaft can now be estimated from the expression

$$\omega(\text{Hz}) = \frac{2}{\pi}\sqrt{\frac{3\,E\,I}{L^3(M_c + 0.49\,M_{sh})}}$$

where $I = \pi/4\ R^4$ is the bending moment of inertia of the shaft and M_c, M_{sh} are the "center mass" and shaft mass, respectively. E is the Young's modulus, taken as 2.1×10^{11} N/m^2 for steel. We obtain $I = 3.07\times10^{-7}$ m^4, M_c = 15.1 Kg, M_{sh} = 7.7 Kg, giving

$$\omega = 182 \text{ Hz} = 10{,}920 \text{rpm}$$

This frequency is more than three times higher than our nominal rotation rate, indicating that shaft flexibility will not be a significant factor in the dynamics of the test rig. However, other elements in the support assembly must be considered as well. In particular, the load cells themselves have significant flexibility (Sec. 3.9.2). A strain-gauge load cell with a 445 N (100 lb) full load rating will be unlikely to have less than about 0.175mm (7 mils) full load deflection, giving a stiffness

$$K_{cell} = 2.50 \times 10^6 \text{ N/m}$$

Assuming the mass of the rotor system plus the support frame is about 50 kg, the frequency of oscillation corresponding to the cell flexibility alone would be $\sqrt{2.5 \times 10^6/50} = 224$ rad/sec = 2140 cpm. This is <u>below</u> the design operating point of 3000 rpm, and would be further lowered by bearing and frame flexibility. Although it might be possible to lighten the rotor or use a heavier load cell (at a sacrifice in resolution, see Sec. 3.9.2), it appears to be difficult to design the rig for sub-critcal operation.

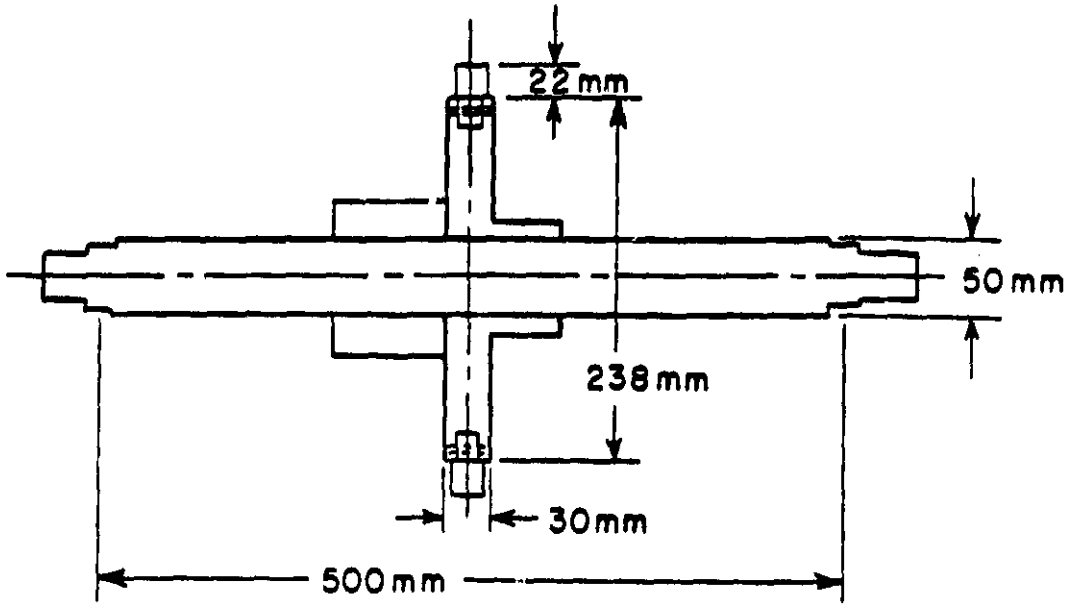

Fig. 3.7.4 Approximate rotor dimensions.

On the other hand, super-critical operation is commonplace in jet engines and many other turbomachines, including both SSME turbopumps. The resonant effects are minimal for rotation rates above $1.3\omega_{cr}$, (ω_{cr} being the shaft resonance or critical frequency), and instabilities are unlikely to develop at rotation rates lower than $2\omega_{cr}$ (Ref. 3), and then, for mechanisms other than dry friction or oil whip, they will only be likely at high power levels; this is in particular true for Alford forces. With careful mass balancing, the shaft c.g. will be within a few microns of the shaft geometrical center, and so, although the shaft will tend to rotate about its c.g. rather than about its axis, the difference will be insignificant for the purposes of our experiments.

With this in mind, it is reasonable to select a target resonance frequency of

ω_{cr} = 1600 to 1800 cpm

= 178 to 188.5 rad/sec

For instance, if ω_{cr} = 1750 cm, and if the test program covers from 2500 to 3500 rpm, we would be in the range of ω/ω_{cr} from 1.43 to 2, which appears to be safe and quiet.

The bearing and frame flexibilities are in series with that of the load cells. Thus, if ω_{cr} = 1750 cpm, their combined stiffness must be 1.68×10^{6} N/m. If we assume bearings with stiffness well above 10^{7} N/m, the remaining major flexibility is that of the frame bar supporting the load cell (see Sec. 3.8). For a pinned-pinned bar of length l and bending moment of inertia I, its stiffness is $K_{bar} = 48EI/l^{3}$, where E is the Young's modulus of the bar material. A steel tube of 3.0 cm outer diameter and 0.6 cm thickness, with a length of 50 cm (the distance between bearings), will have $K^{bar} = 6.7 \times 10^{6}$ N/m, and will thus be adequate for our purposes, since a value of 5.12×10^{6} N/m would combine with the cell stiffness to yield the required K_{TOT}.

As indicated, no rotordynamic instabilities are expected to develop in the planned speed and power ranges. On the other hand, if one were encountered that could not be suppressed at its root, there is the possibility of introducing viscous damping between the bearing support frame and the ground.

3.8 The Bearing Support Frame

As discussed in 3.7, the bearing support frame should transmit the rotor transverse forces to the load cells while absorbing axial loads and all moments. The principle of operation is schematized in Fig. 3.8.1. The load cells (3) and (4) restrict any displacement of the frame in the plane perpendicular to the shaft. They are attached to the shaft by means of articulated joints capable of transmitting only uniaxial force, thus decoupling each cell from slight motions in other directions. The system of roller element guides (5), (6) and (8) would of itself allow any translation of the frame, including axial translation. This

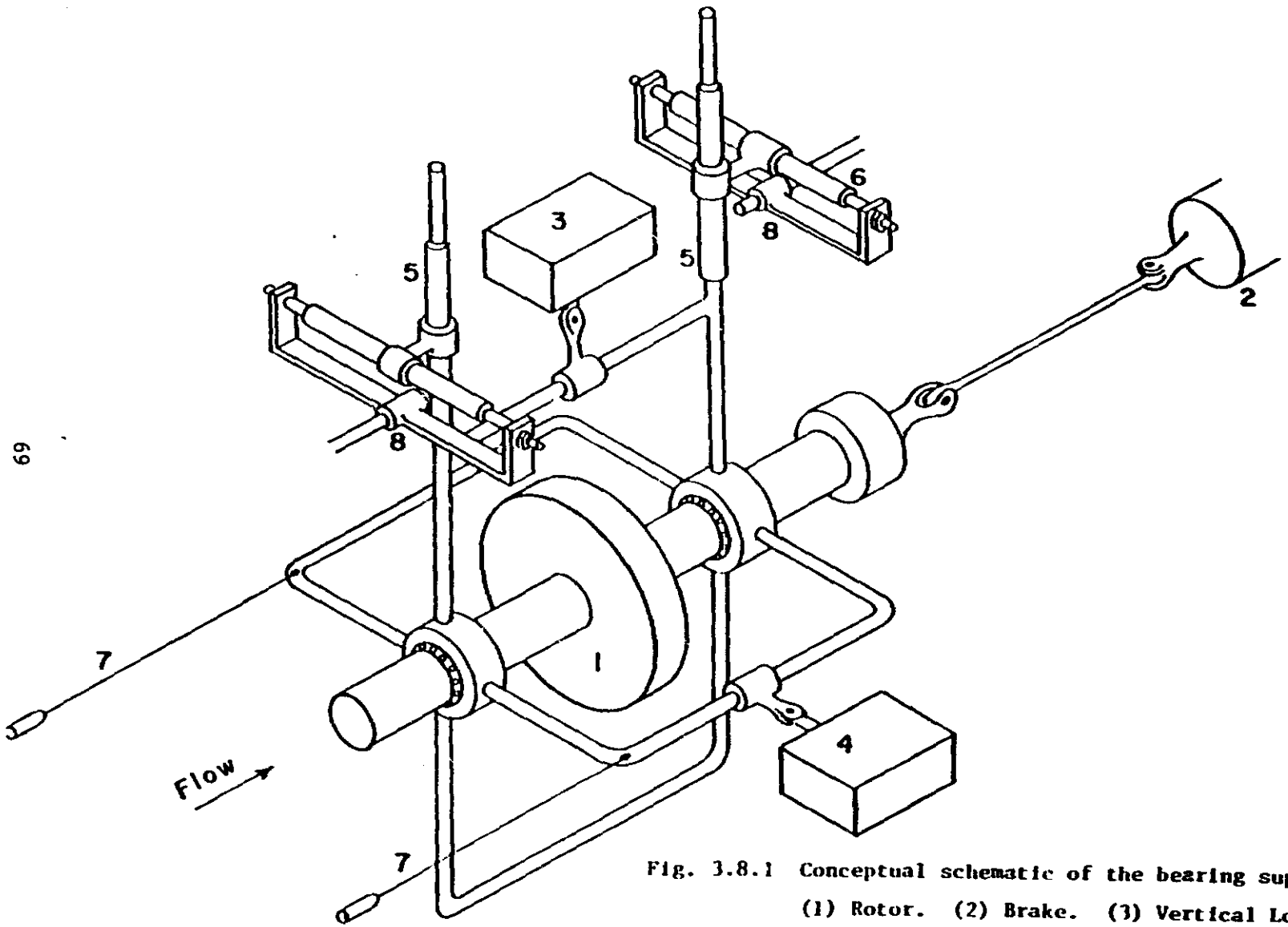

Fig. 3.8.1 Conceptual schematic of the bearing support frame. (1) Rotor. (2) Brake. (3) Vertical Load Cell. (4) Horizontal Load Cell. (5) Vertical Guides. (6) Transverse Guides. (7) Thrust Relief Wires. (8) Axial Guides.

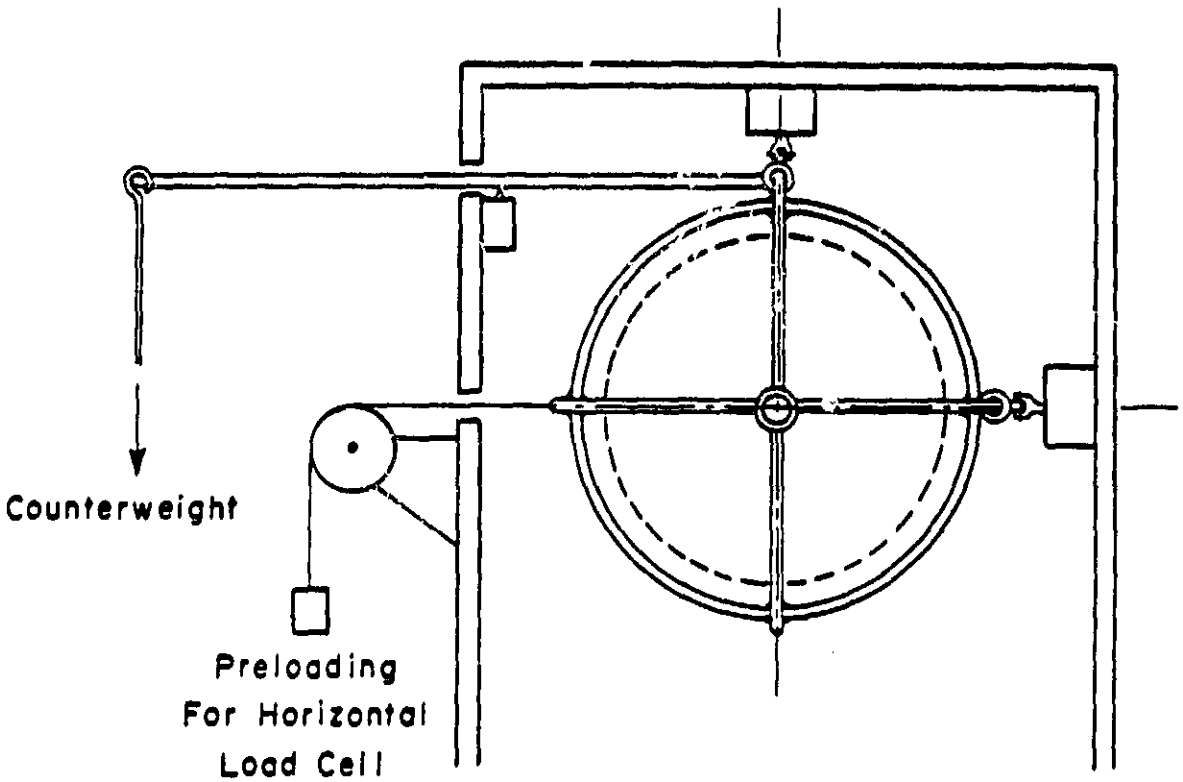

Fig. 3.8.2 Support of the frame and preloading of the load cells.

is restricted by cables (7) with adjustable tension; in this manner, the support frame is free of any bending moment due to the turbine thrust force. This also eliminates thrust loads at the bearings, thus reducing friction. Torques on the frame in the horizontal plane are resisted by both the cables and the transverse guide bars, while pitching torques are resisted by the vertical guide bars. Any torque about the shaft axis transmitted by the bearings is similarly absorbed by the vertical and transverse guides.

The load cells should be under a positive (but small) tension to avoid linkage backlash errors. The arrangement of Fig. 3.8.2 ensures this. A levered counterweight will absorb the larger part of the rotor weight, leaving a small fraction as preloading for the vertical load cell. Preloading for the horizontal cell is provided by a separate small counterweight.

The general arrangement of the frame in its relationship to the turbine casing is shown in Fig. 3.8.3.

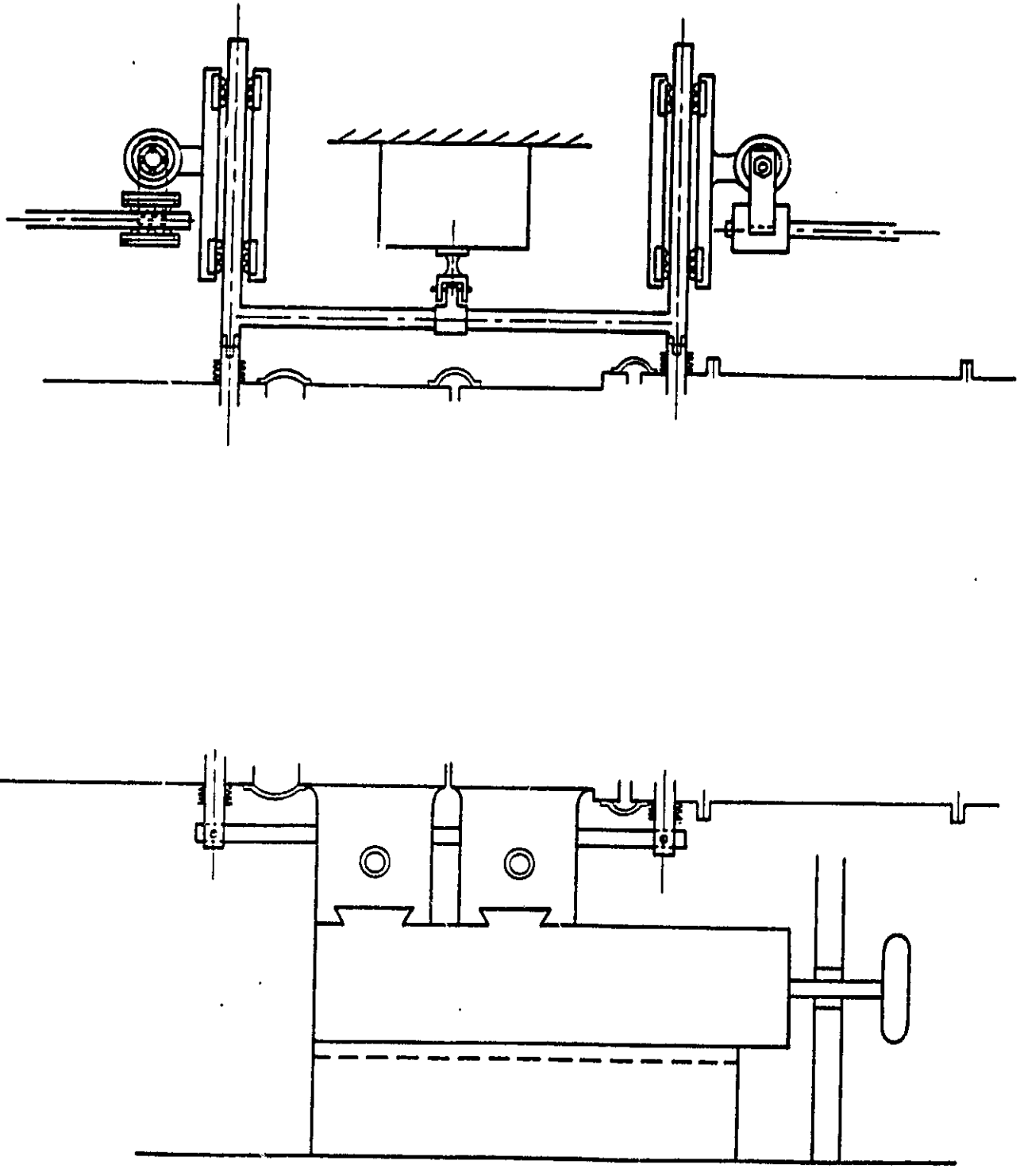

Fig. 3.8.3 The support frame in relation to the test section.
(Side View)

3.9 Instrumentation and Data Acquisition

3.9.1 Instrumentation Layout

The quantities to be measured and the instrumentation required belong to one of three categories:

(a) Facility status and operating parameters. These include mass flow rate, measured by means of a low pressure drop contraction, such as a Venturi or a faired orifice, upstream and downstream total temperatures and pressures, gas composition, rotor rotation rate, braking torque and casing vibrations.

(b) Variables used for Alford force determination. To this category belong the rotor position measurements and the bearing support forces, plus the pressure distributions on rows of taps over the stator and rotor blading.

(c) Variables of value for detailed flow mapping. These include the hot wire or wedge probes to be mounted on movable instrument rings placed upstream and downstream of the stage.

The pressure and temperature measurement points are shown in Fig. 3.9.1, with an "unwrapped" layout, as in Fig. 3.9.2. "Reservoir" conditions are established at location (0), ahead of the test section, by means of two total pressure and two total temperature sensors. These will serve for monitoring purposes, while a detailed traverse will serve to establish the relevant profiles.

After contraction, but far enough from the stator to be unaffected by its eccentricity, a series of static and total pressure probes and of total temperature probes at mid-span will establish the approach boundary conditions (Station (1)).

The corresponding downstream conditions will be provided by azimuthally distributed P and T probes ((8), (9)), as well as by the velocity and total pressure scannings made possible by the downstream instrument ring (7). These measurements, together with those of mass flow rate, rotation speed and torque (see Table 3.9.1), will allow a complete performance characterization of the turbine.

The upstream (2) and downstream (7) instrument rings can rotate through a 90° arc each allowing continuous scanning in the azimuthal direction by means of three clusters of instruments distributed as shown in Figs. 9.3.1 and 9.3.2. Each cluster contains one primary

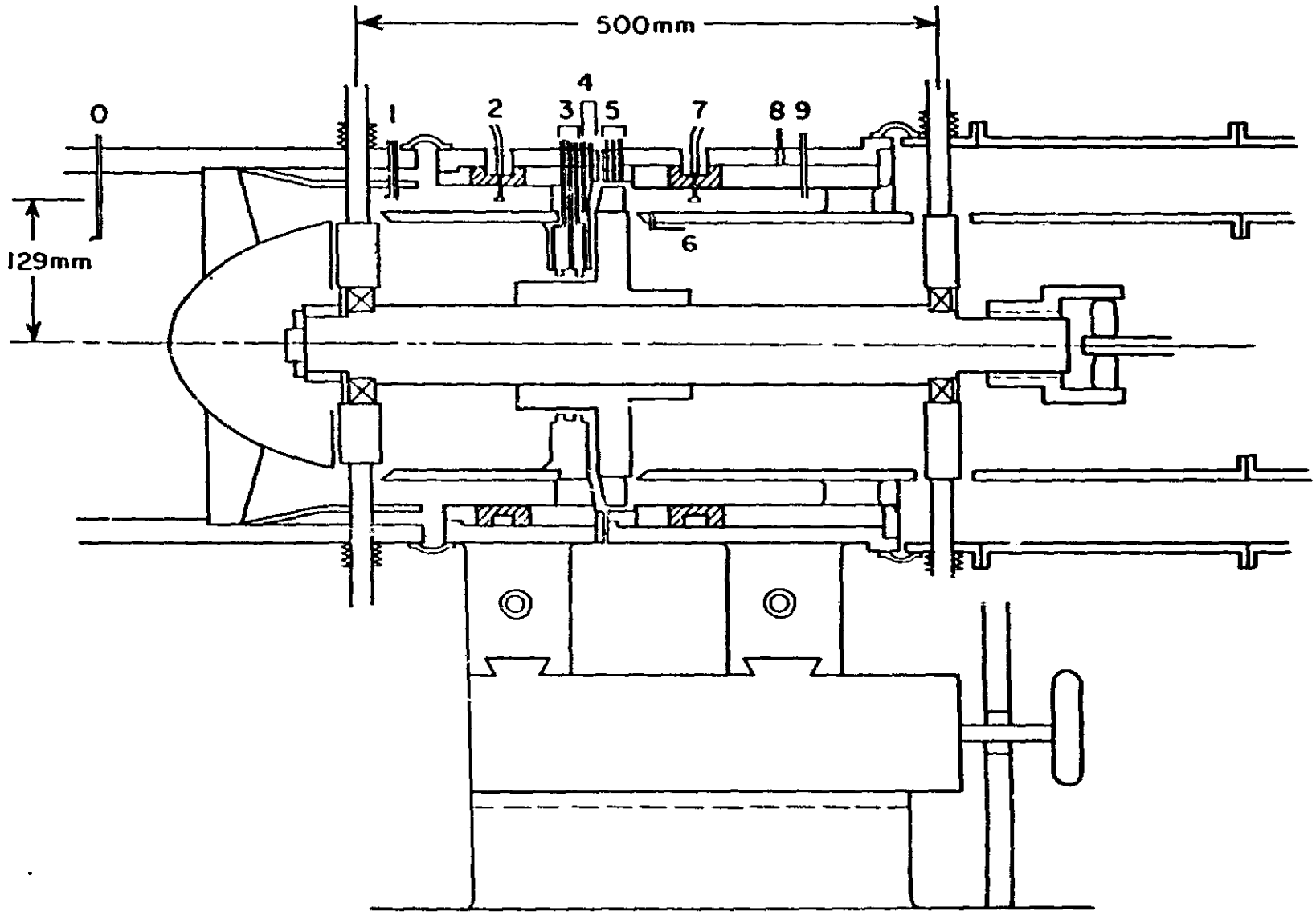

Fig. 3.9.1 Instrumentation ports. Description in the text.

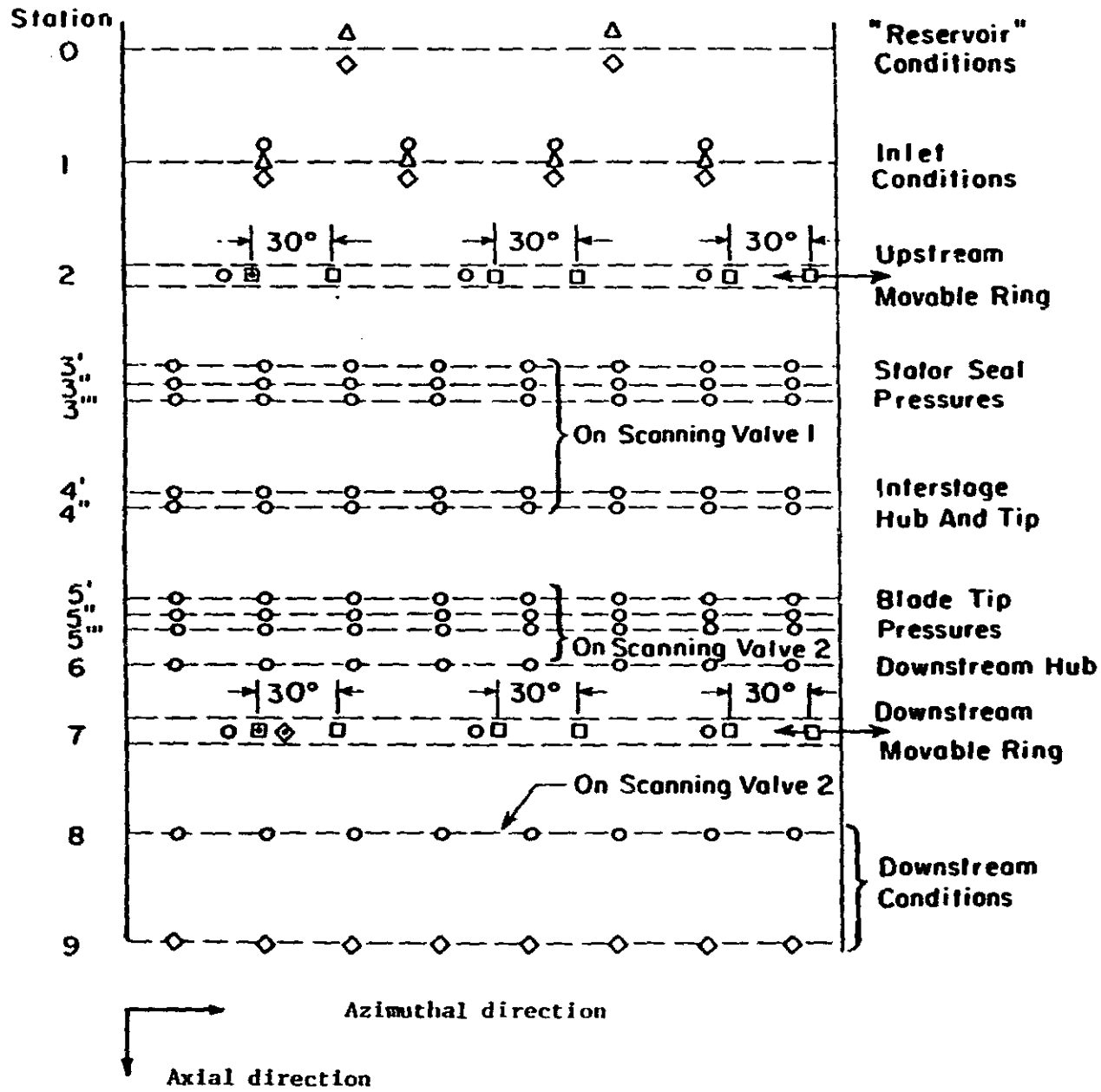

Fig. 3.9.2

Instrumentation Layout

Key to Symbols

- △ p_{total}
- ○ p_{static}
- ▯ Three-hole Wedge Probe
- ◇ T_{total}
- ■ Hot Wire Probe
- ⊟ Traversing Three-hole Probe
- ◆ Traversing T_{tot} Probe

three-hole wedge probe (or hot wire probe) for velocity magnitude and direction, and one additional identical probe with its point of penetration shifted 30° to allow spanning of the blind arcs and to provide data redundancy. One of the probes will be made to traverse in the radial direction. The rings themselves are part of the inner shell of the test section, and communicate with the outside through three partial grooves (90° each) cut in the outer shell.

The stator seal region and the blade tip casing are each instrumented with three rows of eight pressure taps each. In addition, two rows of taps will be provided near the tip and hub, respectively, of the stator-rotor gap in order to facilitate interpretation of performance (stator-rotor split) and offset effects. One more row of taps will be provided near the downstream rotor hub (station (6)). This large number of pressure measurements will be made possible by the use of at least two scanning valves, as indicated in Fig. 3.9.2. A third scanning valve may be required to consolidate most of the remaining pressure measurements.

3.9.2 Instrumentation Requirements

In order to establish instrumentation requirements, it is useful to estimate upper and lower limits on the effects to be measured. The nominal output power of the unshrouded test turbine is about 7 KW (see Sec. 3.4) at a rim speed of roughly 40 m/sec, giving a mean azimuthal force of 175 N. If the "nominal" lateral offset is taken to be 0.3 mm and the Alford G is taken as 3, then, for a blade height of 22 mm we obtain a side force of the order of

$$F = 1.5 \times 175 \times \frac{0.3}{22} = 3.6 \text{ N} \approx 350 \text{ gm}.$$

Thus, for operation at reduced power and with offsets as low as can be reliably measured ($\sim$ 0.1 mm), we are likely to see minimum forces to be measured of the order of 60 gm; conversely, the maximum force may be of the order of 1-2 Kg.

If a substantial fraction of these forces can be attributed to a pressure nonuniformity of the type $p = p_o + p_i \sin\theta$ (which is likely for shrouded blades, at least), then the amplitude of the pressure variation, p_i, will be of the order of $F/\pi \ell R$, where ℓ is the axial length acted upon by p_1. Using ℓ = 2 cm, R = 13 cm, we obtain

$$p_{i_{min}} \sim 74 \text{ N/m}^2 \sim 0.010 \text{ psi} \sim 0.5 \text{ mm Hg} \sim 8 \text{ mm } H_2O$$

Table 3.9.1 Other Instrumentation

Variable	Symbol	Sensor	Transducer	Number
Side Forces	F_x , F_y	Strain Gauge Load Cells		2
Flow Rate	$\dot{m}$	Venturi	Pressure Transducers	1
Rotation Rate	Ω	Magnetic Pickup		1
Torque	Q	Flex. Mount on DC Brake	Strain Gauges	1
Axial Gap	δ_{ax}	Micrometer + Proximeter		1 each
Radial Gap	$\delta_r(\theta)$	Micrometer + Proximeter		3 each
Air Concentration	x_a	Speed of Sound Meter	Spark + Microphone	1
Frame + Case Vibrations	a_v	Accelerometers		

This is at the lower end, but well within the measurable range with standard instruments (the typical resolution of a 2 psi transducer is of the order of 0.002 psi). On the other hand, little difficulty is to be anticipated for measurements in the "nominal" range.

Regarding the measurement of the forces themselves, the most severe constraint is that the load cells should be stiff enough to allow an adequately high first natural frequency (see Sec. 3.7.4) and to avoid interference with the turbine centering. A small yielding of the cell, say, less than 20% of the mean gap, can be tolerated, provided it can be accurately monitored, but it is likely to complicate operations and data reduction. If we impose, for example, a 0.05 mm (2/1000 inch) yield under a 10 kg load (as may be used for cell pre-loading), the required stiffness is 2×10^6 N/m, which, according to Sec. 3.7.4 is also adequate for dynamic purposes. This high stiffness can always be achieved with cells of high enough load capacity, but a limitation may be encountered then in terms of resolution. As an example, one particular line of high quality strain-gauge cells which are available commercially has full scale deflection of 0.175 mm (7/1000 inch) for full scale loads of 100, 200, or 500 lbs (445, 890, or 2220 N), and have minimum total errors of the order of 0.02% of full scale. Selecting the 445 N type gives a stiffness of 2.5×10^5, with a resolution of 0.09 N (9 gram); the stiffness is doubled for the 890 N type, but so is the minimum accurately measureable force.

One aspect of the test apparatus that will facilitate precise measurements is that, for static tests, which are the most important part of the test series, time-resolved data per se are not required, and so the sampling rates can be long and there are no stringent requirements on length of pressure lines or mass of thermal sensors. This is in contrast with the requirements of the whirling seal test facility, where time resolution is essential. The requirements for the dynamic tests on both rigs are discussed in Sec. 3.11.

3.9.3 Data Acquisition

A count based on Fig. 9.3.2 and Table 9.3.1 indicates 107 pressure measurement points, 15 temperatures and 10 other miscellaneous data channels (proximeters, load cells, torque meter, tachometer). Thus, without including other potential data (from compressor or brake, for instance), we obtain 132 data channels. However, most of the pressure measurements will be made by the transducers connected to three 48-channel scanning valves. As shown in Fig. 3.9.2, two of these will be dedicated to the wall taps in the stator and rotor blade regions, respectively. A third scanning valve will be used to consolidate the probe pressures of either the upstream or the downstream instrument rings, plus perhaps an assortment of other pressure lines. In addition to the obvious savings in transducers, amplifiers and digitizers, this approach has the advantage of largely avoiding calibration differences among many transducers. Depending on the precise configura-

tion of absolute and differential pressure measurements, and including some channels not in the test section area (such as for the flow rate meter), the approximate number of required transducers, and hence pressure data channels, is 12.

The temperature data can also be consolidated prior to A/D conversion by means of thermocouple switches. Thus, only two or three A/D channels will be needed here. Adding the other instrument channels, we arrive at a number of approximately 26 required digitizers. This should not pose severe data-handling difficulties, but will require some software development for correct interfacing to the computer used for data acquisition.

3.10 Test Program

In an ideal sense, the test measurements should be performed for a reasonably large number of values of each of the following parameters:

Nominal radial gap,	δ_o
Turbine speed,	Ω
Turbine flow rate,	$\dot{m}$
Axial gap,	δ_{ax}
Eccentric displacement,	δ

and this should be repeated for each type of turbine, both non-shrouded and shrouded.

Since this would yield a very large number of test points, making the program prohibitively lengthy, some judgment must be used to select a smaller, but still comprehensive, subset of conditions.

First of all, as already explained in Sec. 3.2, we will focus attention on only two turbine blade types, one without and one with a shroud band. These are representative of the type of turbines used by the current SSME turbopumps. For a shrouded case, only one seal arrangement (to be specified later) will be chosen. For each of these configurations, three turbine casing rings of slightly different diameters will be tested, to study the effects of variable mean radial gap. Thus, there will be altogether 3x2 = 6 configurations to be tested, implying a minimum of 6 assembly-disassembly cycles of the test section, and also 6 Freon filling loads. This discussion is summarized in Table 3.10.1.

Table 3.10.1 The Test Matrix

Config. No.	Shroud	Nominal Gap Designation	Ω	$\dot{m}$	δ_{ax}	δ_{tr}	No. of Traverses	No. of Dynamic Tests
1	No	1	Nom.	Nom.	3 pts.	Vary	3	1
1	No	1	25 off-design combinations		3 pts.	Vary	75	25
2	No	2	Nom.	Nom.	3 pts.	Vary	3	1
3	No	3	Nom.	Nom.	3 pts.	Vary	3	1
4	Yes	1	Nom.	Nom.	3 pts.	Vary	3	1
*	Yes	1	25 off-design combinations		3 pts.	Vary	75	9
5	Yes	2	Nom.	Nom.	3 pts.	Vary	3	1
6	Yes	3	Nom.	Nom.	3 pts.	Vary	3	1

As indicated in the table, three values of the axial gap are tested in every case. The turbine operating parameters Ω, $\dot{m}$, however, are to be fully scanned for only one selected value of the nominal radial gap for each turbine. For this selected configuration, a 5x5 matrix of turbine parameters about the design point will be tested (see also Sec. 3.2); for other mean radial gaps, only the turbine design condition will be used. In every case, the zero-offset point will be tested first, to obtain nominal turbine performance values, particularly turbine efficiency. Subsequently, a detailed scan of lateral offset will be performed, noting the variables of interest for Alford force determination. For one axial gap value in each case, a dynamic test will be conducted at the rig natural frequency. A more detailed set of dynamic tests, at various whirl frequencies, will be scheduled later, if these preliminary tests indicate significant effects.

As Table 3.10.1 shows, this procedure leads to a minimum of 84x2 = 168 traverses, each of which should be repeated a number of times (at least three times) to reduce random errors. The lengthiest testing will occur for the selected radial gap, when the turbine map is to be scanned. As a reasonable guess we may assume 30 minutes per set point in this case, which indicates 75x30/60 = 38 hrs. of test time under ideal conditions. Counting interruptions, spot check repeats, etc., this points to a test time of about two weeks for the nominal gap case of each turbine-seal configuration. To this we must add the time for three cycles of evacuation, disassembly, turbine casing ring replacement, assembly realignment, and refilling. Each such cycle is likely to require two to three weeks of work. Thus, for each turbine-seal configuration a <u>minimum</u> test time of about three months is anticipated, or six months for the four turbine-seal cases to be studied. A more realistic estimate considering such factors as facility down time, etc., is of the order of one year.

In addition to this main test sequence, a number of other tests are planned. These include Alford force measurements for an assortment of other conditions, in an effort to reach out for parameters not covered in a systematic way, plus detailed flow explorations for one or two particular configurations. Examples of tests of the first type above are:

- Tests with freon-air mixtures to study the effect of varying the Reynolds number over a relatively wide range ($\sim$ 1/4 to 1).

- Tests with a different <u>stator</u> seal to verify the separation of effects achieved with the nominal design (see Sec. 3.7.2).

- Dynamic tests for a range of whirling (critical) frequencies for selected configurations.

- Tests with other configurations suggested by the results themselves.

As to the second type of tests; i.e., detailed flow mapping, the aim will be to obtain the necessary data to correlate with the theoretical treatment

explained in Sec. 2 of this report. This must include static and stagnation pressure mappings in the vicinity of the stage, as well as hotwire velocity vector maps in the same areas, using the instrumentation described in Sec. 3.9.1. This detailed exploration will be made for only some selected configurations. As a preliminary plan, these should include the nominal configuration of each of the test turbines at their nominal mean gap, plus perhaps four off-design conditions of each of these. It is clear that the nature o the results themselves should serve as a more detailed guide for a final choice of configurations to be studied.

3.11 Dynamic Tests

As discussed in Sec. 2 of this proposal, existing theory predicts significant damping effects in the labyrinth seals of shrouded turbines, and smaller damping effects for the unshrouded case. There is no experimental information for either configuration, and we propose here to conduct tests aimed at obtaining such data, in a separate seals test facility for the shrouded case, and in the same facility used for the static tests in the unshrouded case (confirmatory dynamic testing of the shrouded turbine will also be made in the turbine test rig).

In principle, one set of direct and cross-force measurements at zero whirl (static offset only), plus one or more at some nonzero whirl speed, will be sufficient to calculate both the K_{ij} stiffness coefficients (see Sec. 2) and the C_{ij} damping coefficients. Alternatively, a static measurement can be combined with a measurement of either the lag-decrement of free vibrations or the Q-factor of forced vibrations in order to obtain the damping coefficients. Both approaches are proposed below, since there are advantages to each for the separate cases of shrouded and unshrouded blades.

3.11.1 Seal Dynamic Test Facility

In a seals test facility in which whirl is driven externally, two approaches are possible for obtaining data on the velocity-dependent side forces:

(1) Driven whirl, reaction force measurement

(2) Driven whirl, measurement of seal pressures

The first method is in principle the most desirable, since the information on the forces is obtained directly. However, these forces are superimposed on others arising from mechanical and inertial coupling with the whirl driving mechanism, and a careful design and signal processing is required to extract the seal forces. The second method is an extension to the dynamic range of the method used successfully in Ref. 21 in a static offset situation. Here the forces are obtained by integration of pressure distributions measured around the periphery of each gland in the labyrinth seal; since these pressures vary

at the whirl frequency, and their variations are small, special precautions must be taken in the pressure-sensing arrangement.

In order to obtain fundamental information on these effects, we are beginning the construction of a labyrinth seal whirl facility based on the second of the concepts above, with funding based on an AFOSR grant (Ref. 30). A more applied goal is, naturally, to obtain force data by the integration of these presures around the periphery. Wright (Ref. 25) has obtained some data which indicate that the correspondence between net force and pressure force is less than perfect, although it appears that his tests were made with very low and uncontrolled flow preswirl, which would minimize the level of force and thus amplify measurement errors. Since we will be separately making direct force measurements, as well as pressure distributions, on a statically offset turbine shroud seal, we should be able to compare these two approaches for the static case at least. Additionally, our vibration tests in the turbine test rig will also give us a direct comparison between pressure integration and force data under dynamic conditions.

The design goals for the dynamic seals facility are (1) Ability to produce both spin and controlled whirl motion of the test rotor. (2) Realistic seal pressure drops, i.e., a pressure ratio of up to 1.3 on the last seal strip. (3) A constriction Reynolds No. of no less than 1.5-2x10^5 to avoid unwanted low Re effects. (4) Linear rotor speeds up to 100 m/sec. (5) Capacity to accommodate various seal types and number of chambers. Secondary specifications are a reasonably large nominal gap to facilitate precise eccentricity control, and solid construction to minimize vibrations.

The test section design is shown in Fig. 3.11.1. The rotor diameter is 30 cm, such that a linear speed of 100 m/sec can be reached by driving it at 6370 RPM through a flex-coupling. The whirl motion (up to about 3000 RPM) is produced by supporting the rotor on bearings located eccentrically in a sleeve which is separately driven through a cogged belt by a separate motor. Table 3.11.1 lists several test parameter combinations achievable.

Table 3.11.1

N (No. of Strips)	P_o/P_e (Press. ratio)	P_o (atm)	δ Nominal gap (mm)	$\dot{m}$ (Kg/sec)	R_e Axial gap	R_e No.	Operating Mode
2	1.54	1.54	0.6	0.127		15,000	Steady
2	1.54	1.54	0.8	0.169		20,000	Steady
2	1.54	1.54	1.2	0.254		30,000	Blow-Down
20	3.85	3.85	0.6	0.127		15,000	Steady
20	3.85	3.85	0.8	0.169		20,000	Steady
20	3.85	3.85	1.2	0.254		30,000	Blow-Down

The primary data collected will be in the form of instantaneous pressure distributions around the periphery of each gland. This means a minimum of 6-8 flush-mounted sensitive transducers per gland. These will be differential-pressure sensors, with the reference connected to an annular cavity filled with a damping material and connected through small orifices to several points on the cavity; the cavity will thus provide a mean pressure reference.

The steady operation will be with a direct connection to our Gas Turbine Laboratory oil-free compressed air supply. For higher flow tests we can operate in a blow-down mode using the approximately 60 m^3 of pressurized air storage available.

The test rotor supporting the labyrinth seal is of solid construction, allowing no throughflow, except for the small amount required to pressurize the thrust balancing cavity. There is thus some question as to the possible interaction between the blading flow in a shrouded turbine and the seal leakage flow. The flow rate limitations on the seal facility preclude the testing of an actual shrouded turbine; however, we can, once again, investigate this potential interaction for conditions of static offset in the Alford force facility, by simply blocking the turbine annulus and bypassing most of the Freon flow.

We emphasize here that the seals test facility will be under complete MIT control, and that we intend to dedicate it to the project here proposed with priority over any other research program.

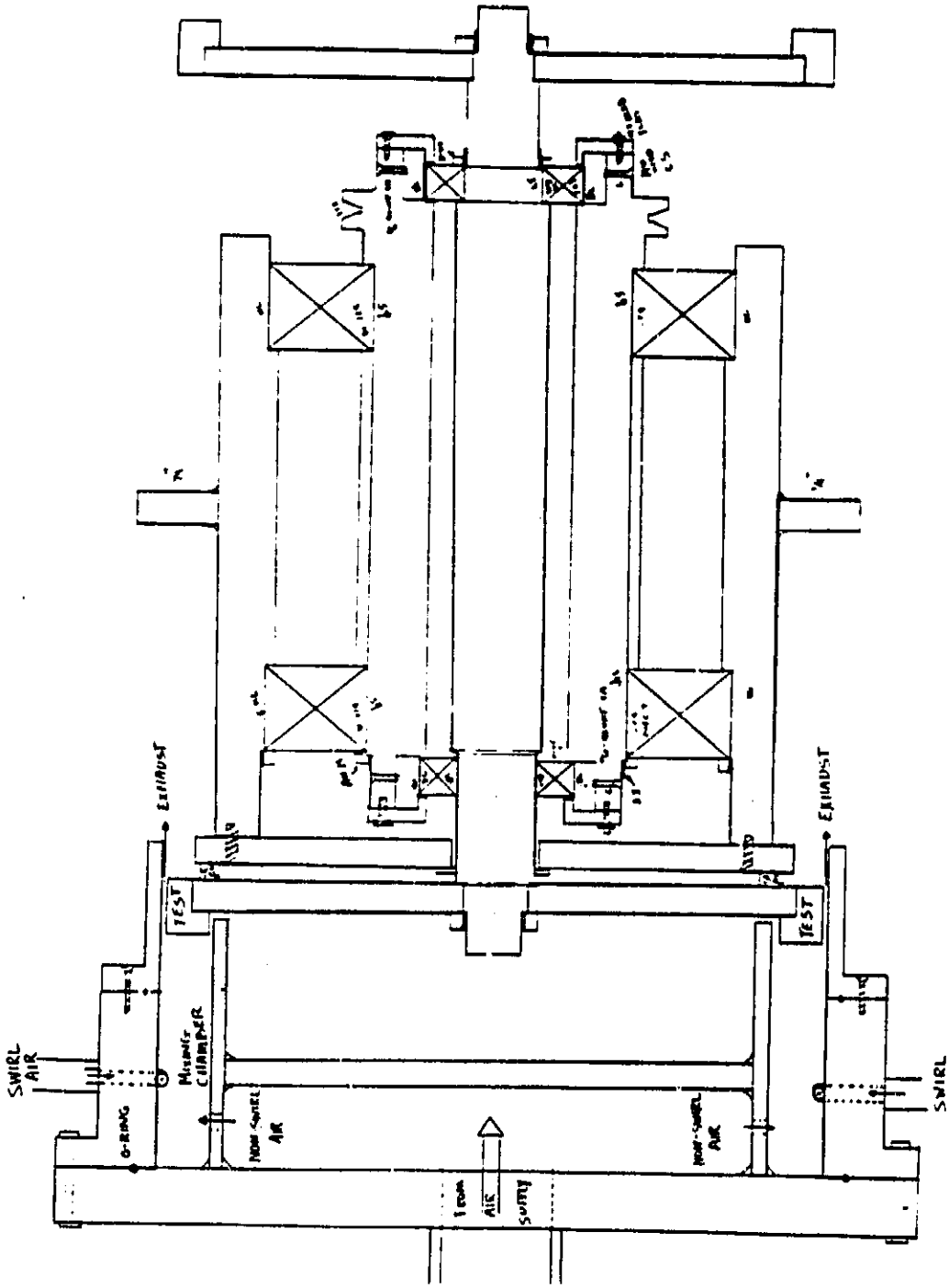

Fig. 3.11.4 Rotor and eccentric drive for dynamic seals facility.

3.11.2 Dynamic Tests in the Turbine Test Facility

The first priority in our experiments in the turbine test rig will go to the measurement of static forces from static deflections. However, dynamic (whirl) tests can, and will be also performed in this rig in order to supplement those planned for the seals test rig. The latter facility will be specifically dedicated to the measurement of the time-dependent pressure patterns in the glands of labyrinth seals, at leakage Reynolds numbers several times higher than can be achieved in the turbine test rig, but it will not be capable of addressing the problem of pure Alford forces (un-shrouded blading) because of (a) lack of direct force measuring capability, and (b) flow rate limitation to about 0.20 kg/sec of air.

To ensure a correct representation of the dynamic effects in the Alford forces on a rotor, the reduced whirling frequency $\Omega\ell/V$ (Ω = whirl frequency, ℓ = a representative length, such as the blade height, V = a characteristic flow speed, such as the axial velocity) must be matched. We have already designed the test rig such that $\omega R/u_x$ is the same as in the HPFTP 1st stage, where ω is the wheel rotation rate. Since the geometrical ratios, like ℓ/R, are also matched, all that is needed is a match of the frequency ratio Ω/ω. For the SSME turbopumps, the 1st critical frequencies, which are the expected whirling rates, are in the range of 0.4 to 0.6 of the rotation rate (Ref. 32). Therefore, if we excite oscillations of the bearing support frame at its design natural frequency (1750 rpm), while the turbine is turning at its design test speed (3000 rpm), we obtain dynamic conditions entirely representative of those in the HPFTP. This can readily be done with very little modification of the rig as it was designed previously.

The whirling frequencies involved (about 30 Hz) are low enough that detailed time-dependent force data will be directly obtainable from the load cells, although, of course, corrections will be necessary for the inertial and damping effects of the vibrating assembly. Additional information can be obtained from the time-dependent position sensors, in the form of either (a) The log-decrement of the damped response if a purely passive vibration is used, (b) The width of the resonance peak if one or two electromagnetic shakers are used to actively excite the vibrations. On the other hand, the frequency response of the pressure sensors, in the configuration used for the static tests, will probably be insufficient for a detailed time-dependent recording of pressures. If the combination of force and displacement data obtained in the vibration tests during the main test sequence indicate a need to refine the time-dependent flow data, we will consider a special test sequence with flush-mounted gauges analagous to the configuration for the seals facility.

Another direction in which these dynamic tests can be extended if warranted is to include additional controllable flexibility in the bearing support frame in order to allow vibration tests to be performed over a range of critical frequencies below the design value of 1750 cpm. Extensions to higher critical frequency could also be made by eliminating the load and

relying on vibration decay only. Tests at lower rotation speed for a given critical frequency may provide similar data.

The most difficult part of the dynamic tests contemplated here is the separation of the blade- or seal-induced whirl damping from other sources of damping in the system. This is a generic problem, unrelated to the methods used to measure total damping; it could be avoided only by some method that would measure separately the individual blade forces in sufficient detail to allow local separation of mean and Alford forces. Given the smallness of the latter in comparison to the mean force, and the other effects associated with the rotation (centrifugation, vibratory environment), this approach seems quite difficult to implement at present. At this point the best course appears to be to conduct a careful set of tare runs (with no blades, or with no flow) to determine separately the non-Alford damping, and then correct the overall damping data. According to our best estimates at this point, this appears also difficult to accomplish with good accuracy.

By way of example, let us consider the nominal conditions (ω = 3000 rpm, turbine power ≈ 7 kw) for the model HPFTP turbine stage (diameter ≈ 26 cm, blade height ≈ 2 cm). Assuming β - 3.0, we have estimated (Sec. 3.9.2) a cross stiffness $K_{xy} = 1.2 \times 10^{6}$ N/m. According to our analysis in Sec. 2, this is equivalent to a damping constant (either positive or negative) of $C_{xx} = K_{xy}/\Omega$, and for a natural frequency Ω = 1750 cpm = 183.3 rad/sec, C_{xx} = 65.5 (N)(sec)/m. The (negative) log-decrement associated with the C_{xx} is $\pi\, C_{xx}/\sqrt{MK_o}$, so that, using M = 50 K and $K_o = 1.68 \times 10^{6}$ N/m (which gives Ω = 1750 cpm), this log-decrement is -0.022. This is the reduction in the logarithmic decrement due to the cross-stiffness alone, and should be measurable without much difficulty. On the other hand, theoretical calculations to be reported in Ref. 33 indicate that for whirling frequency of the order of 1/2 of rotation rate, we can expect at most a 10-20% reduction of the cross-force with respect to its value under static offset. Thus, if we seek to measure specifically this reduction (which is what can be ascribed to blade-tip damping), we would need to measure log-decrement changes of the order of 0.002-0.004. This is indeed small, and its measurement in the presence of other sources of damping is challenging. On the other hand, if the theoretical predictions are correct and the effect is this small, it would be indeed proven inconsequential; we may regard our dynamic tests as a check and a search for unexpected effects not accounted for in the theory, which could conceivably lead to higher, and hence measurable damping forces (this possibility has been advanced as a possible explanation for the smaller-than-expected Alford forces experienced by the SSME turbines).

Conclusions and Recommendations

The principal conclusions reached by this study are:

(1) A very small data base exists for excitation blade tip forces in unshrouded turbines (Refs.7, 19).

(2) A more extensive data base exists for shrouded blading under static offset conditions (Refs. 7, 12).

(3) In both cases, a detailed fluid mechanical understanding of the effect is still lacking. Thus, extrapolations to untested conditions remain dubious.

(4) No reliable data exist on forces proportional to the gap rate of change.

(5) Our theoretical modeling indicates an important contribution of the flow redistribution around the turbine annulus to the Alford force.

(6) Similarly, there is an important contribution of the annulus pressure, even in unshrouded cases.

(7) There is a good probability of successfully extending the data base as well as the detailed mechanistic understanding of these effects by performing tests at a moderate scale.

(8) The test Reynolds number should exceed the critical level of about 2×10^5. This can most conveniently be achieved in a Freon 12 closed loop facility.

(9) The velocity-dependent forces can be separately explored in a dedicated whirl facility which concentrates on the effects occuring at the labyrinth seals.

We therefore recommend that a test program along these lines be instituted, to be supplemented by careful theoretical analysis both preceding and following the tests.

References

1. J.S. Alford, "Protecting Turbomachinery from Self-Excited Rotor Whirl." Journal of Engineering for Power, Oct. 1965, pp 338-344.

2. H.J. Thomas, "Instabile Eigenschwingungen von Turbinenlaufern, Angefacht durch die Spaltstromungen Stopfbuschenun Beschanfelungen. AEG-Sonderdruck, 1958. Also "Unstable Oscillations of Turbine Rotors due to Steam Loakage in the Clearance of the Sealing Glands and the Buckets," Bulletin Scientifique, A.J.M., Vol. 71, 1958, pp 1039-1063.

3. F. Ehrich and D. Childs, "Self-Excited Vibrations in High Performance Turbomachinery," Mechanical Engineering, May 1984, pp 66-79.

4. E. Pollmann, "Stabilitaet einer in Gleitlagern rotierenden Welle mit Spalterregung" (Stability of a shaft rotating in friction bearings under gap excitation) Fortschrittsberichte VDI, Zeitschriftsreihe 1*, No.15.

5. C.J. Winter, "Lastabhaengige Instabile Bewegungen von Turbinen Laeufern" (Load-dependent unstable movements of turbine runners), Diss., Darmstadt Inst. of Techn. (1968).

6. H.J. Thomas, K. Urlichs and R. Wohlrab, "Laeuferinstabilitaet infolge Spalterregung" (Rotor Instability due to gap excitation). Forschungsvereinigung Verbrennungskraftmaschinen (Research Association, Internal Combustion Engines), Frankfurt, Forschungsbericht (Research Report) No. 167 (1974).

7. K. Urlichs, "Durch Spaltstromungen Hervorgerufene Querkrafte an den Laeufern Thermischer Turbomaschinen." Diss., T U Munchen, 1975. Translated as NASA TM 77292, "Clearance Flow-Generated Transverse Forces at the Rotors of Thermal Turbomachines," Oct. 1983.

8. W. Traupel, Termische Turbomaschinen (Thermal Turbomachines). Vol. 1, 1st Ed., Springer, Berlin-Goettingen-Heidelberg, 1958.

9. K. Trutnowsky, Beruehrungsfreie Dichtungen (Non-contact Seals), VDI Publishers, Duesseldorf, 1973.

10. A.G. Kostyuk, "A Theoretical Analysis of the Aerodynamic Forces in the Labyrinth Glands of Turbomachines," Teploenergetika, 19, No. 11, 29-33 (1972).

11. W. Hochreuther, "Kraefte bei Axial Durchtroemten Spalten" (Forces in Gaps with Axial Flow), Diss., Stuttgart Univ. (1975).

12. R. Wohlrab, "Experimentelle Ermittlung Spaltstromungsbedingter Krafte am Turbinenstuffen und Deren Einfluss auf die Laufstablitat Einfacher Rotoren," Diss., T.U. Munchen (1975). Translated as NASA TM 77293, "Experimental Determination of Gap-Flow Conditioned Forces at Turbine Stages, and Their Effect on the Running Stability of Simple Rotors," Oct. 1983.

13. J.M. Vance and F.J. Laudadio, "Experimental Measurement of Alford's Force in Axial Flow Turbomachinery." ASME Paper 84-GT-140, June 1984.

14. T. Iwatsubo, "Evaluation of Instability Forces of Labyrinth Seals in Turbines or Compressors," NASA CP 2133, May 1980.

15. O.W.K. Lee, M. Martinez-Sancnez and E. Czajskowski, "The Prediction of Force Coefficients for Labyrinth Seals." NASA CP 2338, May 1984.

16. A. Egli, "The Leakage of Steam Through Labyrinth Seals," Trans. ASME, Vol. 57, 1935, pp 115-122.

17. K. Komotori, "A Consideration of the Labyrinth Packing of Straight-Through Type Seals," Nihon Kikai Gakkai, Trans. J.S.M.E., Vol. 23, No. 133, 1957, pp 617-623.

18. A.R. Wadia and T.C. Booth, "Rotor Tip Leakage: Part II - Design Optimization Through Viscous Analysis and Experiment." ASME paper 81-GT-72.

19. A. Patera (of MIT, ME Dept.). Private Communication.

20. H. Benckert, "Stromungsbedingte Fedeskennwerte in Labyrinthdichtungen." Diss., U. Stuttgart, Oct. 1980.

21. H. Benckert and J. Wachter, "Flow-Induced Spring Coefficients of Labyrinth Seals for Application in Rotor Dynamics." NASA CP 2133, May 1980.

22. Y.M.M.S. Leong and R.D. Brown, "Circumferential Pressure Distribution in a Model Labyrinth Seal." NASA CP 225C, May 1982.

23. Y.M.M.S. Leong and R.D. Brown, "Experimental Investigation of Lateral Forces Induced by Flow Through Model Labyrinth Glands." NASA CP 2338, May 1984.

24. D.V. Wright, "Air Model Tests of Labyrinth Seal Forces on a Whirling Rotor." Journal of Engineering for Power, Trans. ASME, Series A, Vol. 100, No. 14, Oct.1978, pp 533-543.

25. D.V. Wright, "Labyrinth Seal Forces on a Whirling Rotor," in Rotor Dynamic Instability, AMD - Vol. 55, pp 19-31, 1983.

26. S.H. Greathead and M.D. Slocombe, "Investigation into Output-Dependent Rotordynamic Instability of the High-Pressure Rotor of a Large Turbo-generator. IFTOMM Conference on Rotordynamic Problems in Power Plants, Italy, September 1982, pp 27-35.

27. J.P. Gostelow, Cascade Aerodynamics. Pergamon Press, 1984.

28. E. Duncombe, Aerodynamics of Turbines and Compressors. W.R. Hawthorne (Editor), Princeton University Press, 1964, p 481.

29. W.M. Kays and A.L. London, Compact Heat Exchangers, McGraw-Hill, 1964.

30. "Fluid Dynamic-Structural Interactions in Labyrinth Seals." AFOSR Grant 84-NA-388. M. Martinez-Sanchez and J. Dugundji (MIT), Principal Investigators.

31. J.H. Horlock and E.M. Greitzer, "Non-Uniform Flows in Axial Compressors Due to Tip Clearance Variation," Proc. Inst. Mech. Engrs., Vol.197C.

32. D.G. Ainley and G.C.R. Mathieson, "An Examination of the Flow and Pressure Losses in Blade Rows of Axial Flow Turbines," R&M No. 2892 (March 1951). Aeron. Research, Comm., U.K.

33. M.C. Ek, "Solution of the Subsynchronous Whirl Problem in the High Pressure Hydrogen Turbomachinery of the Space Shuttle Main Engine.' Paper AIAA 78-1002, presented at the 14th AIAA/SAE Joint Propulsion Conference, Las Vegas, Nevada, July 1978.

34. Dunham and Came, "Improvements to the Ainley-Mathieson Method of Turbine Performance Prediction." ASME Transactions. July 1970.

35. Horlock, J., Axial Flow Turbines, Krieger, 1982.